ROYAL SOCIETY OF CHEMISTRY

Check for updates

Low-dimensional materials for ammonia synthesis

Apabrita Mallick, [ID] [a] Carmen C. Mayorga-Martinez [ID] [b] and Martin Pumera [ID] *[ac]

Ammonia is an essential chemical due to its immense usage in agriculture, energy storage, and transportation. The synthesis of "green" ammonia *via* carbon-free routes and renewable energy sources is the need of the hour. In this context, photo- and/or electrocatalysis proves to be highly crucial. Low-dimensional materials (LDMs), owing to their unique properties, play a significant role in catalysis. This review presents a vast library of LDMs and broadly categorizes their catalytic performance according to their dimensionality, *i.e.*, zero-, one-, and two-dimensional catalysts. The rational design of LDMs can significantly improve their catalytic performance, particularly in reducing small molecules like dinitrogen, nitrates, nitrites, and nitric oxides to synthesize ammonia *via* photo- and/or electrocatalysis. Additionally, converting nitrates and nitrites to ammonia can be beneficial in wastewater treatment and be coupled with CO_2 co-reduction or oxidative reactions to produce urea and other valuable chemicals, which are also discussed in this review. This review collates the works published in recent years in this field and offers some fresh perspectives on ammonia synthesis. Through this review, we aim to provide a comprehensive insight into the catalytic properties of the LDMs, which are expected to enhance the efficiency of ammonia production and promote the synthesis of value-added products.

1. Introduction

Ammonia is a valuable chemical because of its diverse applications, such as in fertilizer industries, as a viable precursor to produce fine chemicals, and as a source of clean hydrogen energy storage, making it a potential alternative to fossil fuels.[1–3] The current large-scale synthetic industrial technique for ammonia production is the Haber–Bosch process, however, this process demands high energy input. This process consumes about 1–2% of global energy resources per year and contributes to carbon emissions corresponding to ~1% of global greenhouse gas emissions per year. This has prompted scientists to ponder over alternative, sustainable methods and, thus take a step toward attaining a carbon-neutral economy.[4,5] The inspiration for devising such reactions is acquired from the nitrogen cycle occurring in nature, where biological nitrogenase enzymes catalytically reduce dinitrogen to ammonia.[6] Consequently, different biohybrid catalysts were engineered to photoreduce nitrogen and produce ammonia. Various materials other than biohybrids evolved with time and participated in

ammonia synthesis.[7,8] Photo-, electro-, and photoelectrocatalytic processes have been mostly employed for synthesizing ammonia by reducing dinitrogen, nitrates, nitrites, and nitric oxides. The reaction conditions, mechanisms, benefits, and drawbacks of these catalytic processes are discussed in the review.

Over recent years, low-dimensional materials (LDMs) have emerged as effective catalysts in photo- and electrocatalysis. LDMs are typically defined as materials smaller than 100 nm in a minimum of one dimension.[9] Standard examples of LDMs include 0D spherical nanoparticles, 1D nanorods, nanowires, and 2D nanosheets. In lower dimensional (0D, 1D, and 2D) materials, their quantum-confined structures modify the electronic properties such that the LDMs become more efficient catalysts than their bulk counterparts, offering increased activity and stability.[10,11] LDMs have long been studied for their structural and optoelectronic properties, but their utilization in catalysis is quite recent.[12] This review explores the current state-of-the-art utilization of LDMs for ammonia synthesis by photo- and/or electroreduction of nitrogen-containing small molecules like dinitrogen, nitrates, nitrites, nitric oxides, *etc.* For a better understanding of the roles of dimensionalities, the catalytic synthesis of ammonia by LDMs has been categorized according to the dimensionality of the LDM (0D, 1D, and 2D) catalysts used for the photo- or/and electrocatalytic production of ammonia (Fig. 1). These low-dimensional materials present a wide range of physical and chemical characteristics that can boost the catalytic reactions.

[a] *Advanced Nanorobots and Multiscale Robotics Lab, Faculty of Electrical Engineering and Computer Science, VSB – Technical University of Ostrava, 17. listopadu 2172/15, 70800 Ostrava, Czech Republic.*
E-mail: martin.pumera@vsb.cz, pumera.research@gmail.com

[b] *School of Biomedical Engineering, Peruvian University of Applied Sciences (UPC), Prolongación Primavera 2390, 15023, Lima, Peru*

[c] *Department of Chemical and Biomolecular Engineering, Yonsei University, 50 Yonsei-ro, Seodaemun-gu, Seoul 03722, Korea*

This journal is © The Royal Society of Chemistry 2025

Chem. Soc. Rev., 2025, **54**, 5021–5080 | **5021**

In recent years, several reviews have been published, showcasing various techniques for ammonia synthesis. For instance, two reviews by Pang *et al.* and Ruan *et al.* focus on two-dimensional materials for nitrogen reduction by electrocatalytic pathways.[13,14] Qing and co-workers reviewed recent works on electrocatalytic N_2 reduction to produce ammonia,[15] and Shi and colleagues provided an account of photocatalytic procedures to generate ammonia.[16] Xiong *et al.* summarized the works on ammonia synthesis *via* electrochemical nitrate reduction.[17] All these reviews on ammonia synthesis primarily focus on either 2D materials for electrocatalytic or photocatalytic synthesis of ammonia. Further elucidation of the novelty of this review compared with some of the existing reviews published in the last few years in the context of ammonia

synthesis highlights the catalytic method, materials used, and N-sources used as reactants as presented in Table 1. Based on our current knowledge, a comprehensive review encompassing all low-dimensional materials, including 0D, 1D, and 2D, for ammonia synthesis is still pending. Some reviews also concentrate on LDMs for CO_2 reduction or HER.[9,18,19] Nevertheless, a review of LDMs for ammonia synthesis is lacking until now. This review presents all three classes of emergent low-dimensional catalysts for photochemical, electrochemical, and photoelectrochemical ammonia synthesis. Further, with the growing importance of ammonia synthesis in the global market and the increasing number of publications in this field, a thorough analysis and discussion on this subject is imperative and has been undertaken in this review.

The review is divided into eight sections. Section 2 focuses on the different approaches undertaken for synthesizing ammonia over the past years. The most common synthetic strategy of ammonia is the industrial Haber–Bosch process; however, this process is both energy-intensive as well as harmful to environment. Hence, other green strategies have been devised over time, which include enzyme catalysis and photo- and/or electrocatalysis. Here, we will also discuss the reaction pathways for ammonia synthesis.

In Section 3, we explore how the different dimensionalities of the LDMs play significant roles in catalysis. Zero-, one-, and two-dimensional (0D, 1D, and 2D) materials have different optoelectronic properties, impacting the catalytic process for ammonia synthesis. Through this review, we will present the latest advancements in developing LDMs, their characteristics, and the advantages they offer for catalytic ammonia production. The LDMs will be categorically summarized in the review, along with descriptions of the catalytic processes. These LDMs are often integrated to produce heterostructures that form promising catalysts for ammonia formation. Heterostructures

Apabrita Mallick

Dr Apabrita Mallick earned her PhD in Chemical Science from the Indian Institute of Science Education and Research (IISER), Kolkata, in 2022. Thereafter, she joined as a post-doctoral researcher at the Advanced Nanorobots and Multiscale Robotics Lab, led by Prof. Martin Pumera at VSB–Technical University of Ostrava, Czech Republic. Her current research interests encompass micro/nanorobotics, photocatalysis, low-dimensional materials, environmental remediation, nitrate-to-ammonia conversion, small molecule activation, and the generation of value-added products.

Carmen C. Mayorga-Martinez

Dr Carmen Mayorga is currently a professor at the School of Biomedical Engineering, UPC-Peruvian University of Applied Sciences. Previously, she was a senior scientist at VSB–Technical University of Ostrava and led the Kralupy unit of the Centre for Advanced Functional Nanorobots, UCT-Prague. She was a research fellow in the nanobioelectronics and biosensors group/ICN2, Barcelona-Spain, and at Nanyang Technological University, Singapore. Currently, her main research fields include the development of bio/sensors based on 2D-materials platforms functionalized with bioreceptors (enzyme, DNA, and antibodies) as well as micro/nano robotics at different scales and different propulsion modes for biomedical applications and environmental monitoring. Moreover, she is also interested in 2D-materials catalysis for energy applications.

Martin Pumera

Professor Martin Pumera is Head of the Advanced Nanorobots and Multiscale Robotics Laboratory at VSB–Technical University Ostrava, Czech Republic. He founded the Center for the Advanced Functional Nanorobots at UCT Prague, where he served as a director (2017–2023). He was a tenured group leader at the National Institute for Materials Science, Japan, in 2006. In 2010, Martin joined Nanyang Technological University, Singapore, where he worked as a tenured associate professor for almost a decade. Prof. Pumera has diverse research interests in nanomaterials and microsystems, in the specific areas of micro and nanomachines, electrochemical energy storage and conversion, machine intelligence, and 3D printing.
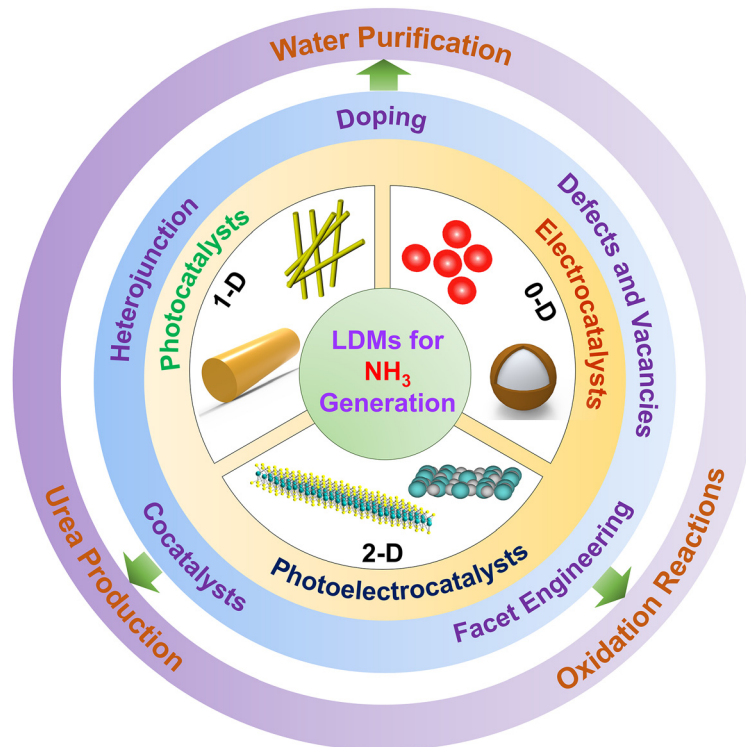
5022 | *Chem. Soc. Rev.*, 2025, **54**, 5021–5080

This journal is © The Royal Society of Chemistry 2025

Fig. 1 Schematic overview of low-dimensional materials used as catalysts for ammonia synthesis.

render the interfaces with unique properties, leading to improved charge transfer and slowing down the recombination of charge carriers, thereby promoting catalytic ammonia synthesis.[40] In the next three sections of the review, we describe up-to-date progress on LDMs in ammonia synthesis and categorize them according to the energy input, *i.e.*; photocatalysts, electrocatalysts, and photoelectrocatalysts.

Section 4 delves into a comprehensive array of 0D, 1D, and 2D low-dimensional photocatalytic materials used for ammonia synthesis. Structure engineering of the photocatalysts for enhancing catalytic performance *via* the introduction of defects, construction of heterojunctions,[21] and increasing surface area by hybridization with other materials will be explored further.[41–43] The role of co-catalysts in boosting the photocatalytic efficiency of ammonia synthesis will also be discussed here.[44]

Section 5 focuses on electrocatalysts that efficiently convert N-containing species to ammonia. Like photocatalysts, the low-dimensional electrocatalysts (0D, 1D, and 2D) have also been modified for better performance *via* defect engineering, formation of heterostructures and regulation of crystal planes, and the roles of such modifications will be illustrated with distinct examples.[45–47] LDMs have also been used to produce 3D-printed electrodes that can electrocatalytically reduce nitrates and nitrites to form ammonia.[48] 3D printing techniques can precisely tune the shape, structure, and geometry of LDMs; hence, we will explore these emerging 3D-printed LDM catalysts for enhancing catalytic performance.

Section 6 emphasizes low-dimensional photoelectrocatalysts that combine the advantages of photocatalysts and electrocatalysts. In photoelectrocatalysis the combination of light and electric bias helps improve the separation and migration of electron–hole pairs, reducing recombination losses.[49,50] Narrow band gap materials or heterostructures formed by LDMs are mostly used for designing photocathodes, and these LDMs will be explored in detail in this section.[51,52]

In Section 7 we discuss the advantages and applications of ammonia synthesis reactions. For instance, nitrates are well-known contaminants in groundwater, so reducing nitrates apart from yielding valuable-added ammonia also aids in wastewater treatment.[53] The reduction process can also be coupled with valuable oxidation reactions, such as water oxidation, methanol oxidation, glycerol oxidation, and plastic degradation *via* PET oxidation.[54–56] These reactions will also be explored in the review. The reduction of dinitrogen or nitrates, coupled with the co-reduction of CO_2 can produce urea *via* C–N coupling. Urea is the most common fertilizer used in agriculture.[57] This process is extremely beneficial as it can help realize carbon/nitrogen neutrality in the environment. The design of catalysts for two co-reduction processes is difficult, but not impossible. Dual-site, bimetallic, single-atom catalysts have been employed to achieve the formation of urea.[58–60] The catalysts explored in all these aspects will be discussed in this section.

The final section presents future perspectives and the outlook for ammonia synthesis. All sections in this review are supported and illustrated with representative literature from

This journal is © The Royal Society of Chemistry 2025

Chem. Soc. Rev., 2025, **54**, 5021–5080 | **5023**

Table 1 Selected examples of recently published reviews and perspectives on ammonia synthesis

| Journal	Catalytic approach	Highlights	N-Source	Ref.
Nat. Energy	Electrocatalysis	Metal-based catalysts, reactor design	N_2	20
Nat. Catal.	Electrocatalysis	Reaction mechanism, protocols	NO_x	21
Nat. Catal.	Electrocatalysis	Challenges, protocols, and future perspectives	N_2	22
Nat. Synth.	Photo- and electrocatalysis	Mechanisms and catalyst design	N_2	23
Chem. Rev.	Electrocatalysis	Theoretical and experimental N_2RR	N_2	15
Chem. Soc. Rev.	Electrocatalysis	2D catalysts	N_2	13
Chem. Soc. Rev.	Photocatalysis	Materials, structure, and reaction engineering of MO_x, $BiOX$, g-C_3N_4, and organic frameworks	N_2	16
Chem. Soc. Rev.	Photo-, photoelectro- and photothermocatalysis	Fundamentals and challenges of N_2RR, reaction mechanisms, quantification methods, techno-economic applications	N_2	24
Adv. Mater.	Photo-, electro-, and photoelectrocatalysis	Reaction mechanism, catalyst engineering	N_2	25
Adv. Mater.	Photo- and electrocatalysis	Reaction and catalyst engineering	N_2	26
Adv. Mater.	Electrocatalysis	Reaction mechanism, catalyst design	NO_3^-	17
Adv. Energy Mater.	Electrocatalysis	Fe-based single-atoms	N_2, NO_3^-	27
Adv. Funct. Mater.	Electrocatalysis	Active hydrogen in N_2RR and NO_xRR	N_2, NO_3^-, NO	28
ACS Energy Lett.	Electrocatalysis	Li and alkaline earth metal catalysts	N_2	29
ACS Nano	Electrocatalysis	Group VIII-based catalysts	NO_3^-	30
ACS Nano	Electrocatalysis	Graphene derivatives	N_2	31
ACS Catal.	Photocatalysis	Fe-based catalysts	N_2	32
ACS Catal.	Electrocatalysis, catalysis under temperature and pressure	Ru-based catalysts	N_2	33
Small	Electrocatalysis	Single-atom catalysts	N_2	34
Small Methods	Electrocatalysis	Reaction mechanism, catalyst engineering	N_2, NO_3^-	35
Small Methods	Photo- and photoelectrocatalysis	Reaction mechanism, catalyst engineering	N_2	36
Chem. Eng. J.	Electrocatalysis	Reaction mechanism, catalyst engineering	NO_3^-	37
Chem. Eng. J.	Photo-, electro-, and thermocatalysis	Ru-based single-atoms	N_2	38
J. Mater. Chem. A	Electrocatalysis	2D catalysts	N_2	14
J. Mater. Chem. A	Photo- and photoelectrocatalysis	Three-phase interface heterojunction catalysts	N_2	39
This Review	**Photo-, electro-, and photoelectrocatalysis**	**0D, 1D, 2D, and heterostructured catalysts, reaction pathways, applications**	**N_2, NO_3^-, NO_2^-, and NO**	

the last decade (2015–2025). This review aims to present a vast library of emergent low-dimensional materials for ammonia generation. It also provides a comprehensive insight into the choice of materials for catalysts, the strategic designs employed to reach maximum efficiency, and implementations toward next-generation applications.

2. Approaches to make ammonia: methods and reactions of ammonia synthesis

The synthesis of ammonia is important as ammonia has versatile uses, such as zero-carbon fertilizers, energy storage, and the synthesis of value-added products.[2,3,61] Global production of ammonia amounts to $\sim$170 million metric tons per year.[62] The industrial synthesis of ammonia mainly involves gaseous nitrogen, abundantly available in the atmosphere. But the process is not very simple. The dissociation of $N\equiv N$ requires a very high energy of $\sim$941.8 kJ mol^{-1}, and the standard enthalpy of formation of ammonia at 25 °C is -46 kJ mol^{-1}.[63,64] Hence, the synthesis of ammonia becomes challenging as the reaction involves high temperature, high pressure, or reactive reagents, and also the process is not energy efficient. This section focuses on the most widely used strategies explored till now to synthesize ammonia (Fig. 2).

2.1. Haber–Bosch process

To meet the need for ammonia-based fertilizers, in the early twentieth century, two Nobel Prize-winning chemists, Fritz Haber and Carl Bosch, invented a high-pressure reaction to directly combine N_2 and H_2 to form ammonia (eqn (1)).[66] To date, most industries rely on this process for the commercial production of ammonia. The modified Haber–Bosch reaction is typically conducted over Fe- or Ru-based catalysts in the temperature zone of 623–773 K and the pressure region of 15–35 MPa.[66] This process is energy-intensive, accounting for about 1–2% of global energy consumption. The H_2 required for this process is mostly derived from the combustion of fossil fuels. It releases CO_2, contributing to $\sim$1% of the total greenhouse gas emissions of the world.[4] The reaction for ammonia production following the Haber–Bosch process is as follows:

$$N_2 + 3H_2 \xrightarrow[\substack{623-773 \text{ K} \\ 15-35 \text{ MPa}}]{\text{Fe/Ru based catalyst}} 2NH_3 \qquad (1)$$
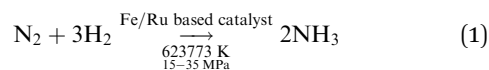
2.2. Enzyme-catalyzed reactions

In an attempt to reduce the carbon footprint generated by Haber–Bosch reactions, researchers have taken inspiration from biological nitrogen fixation reactions. In this reaction, nitrogenase, a bacterial enzyme, directly converts atmospheric N_2 to NH_3 (eqn (2)).[67] Instead of H_2, this reaction uses protons

5024 | *Chem. Soc. Rev.*, 2025, **54**, 5021–5080
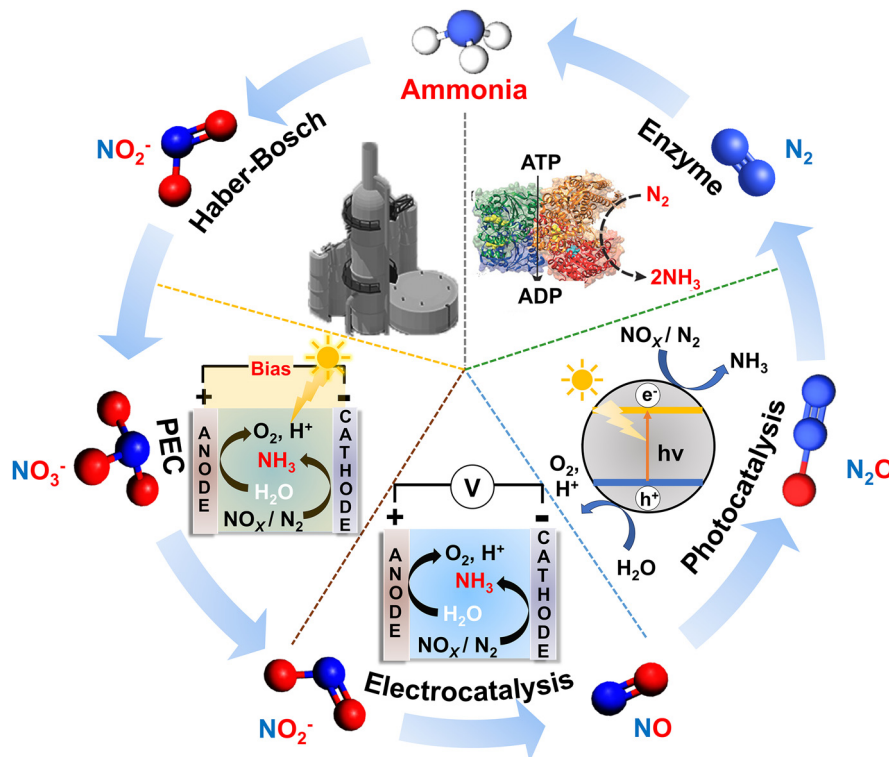
This journal is © The Royal Society of Chemistry 2025

Fig. 2 Schematic representation of different routes to synthesize ammonia. Industrial Haber–Bosch process, nitrogenase enzyme-catalyzed reaction, reproduced with permission from ref. 65, copyright 2017, Wiley-VCH, photocatalysis, electrocatalysis, and photoelectrocatalysis from the conversion of N_2, NO_x^-, and NO_x.

and electrons to form the N–H bonds in ammonia. Nitrogenase comprises two proteins: Fe-based protein (FeP) and MoFe-based protein (MoFeP).[65,67] FeP hydrolyzes ATP to ADP, and the electrons generated in this process are transferred to MoFeP. MoFeP reduces N_2 to NH_3. Stoichiometrically, six pairs of protons and electrons should be used for the synthesis of NH_3 from N_2. But the reaction takes up 8 pairs of H^+/e^-. This apparent wastage of $2e^-$ and 4 ATP molecules contributes to the energy required for thermodynamically driving the reaction. However, excess energy usage leads to a large chemical overpotential of this reaction.

$$N_2 + 8H^+ + 8e^- \xrightarrow[\text{16 ATP} \quad \text{16 ADP + 16 P}_i]{\text{Nitrogenase}} 2\,NH_3 + H_2 \qquad (2)$$
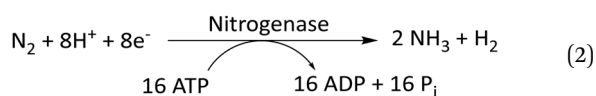
The high demand for ammonia has led researchers to find a sustainable method for its synthesis that will be energy-efficient, cost-effective, and environmentally benign. In recent years, numerous methods, such as plasma, thermochemical, photochemical, electrochemical, and photoelectrochemical techniques have been explored to decarbonize ammonia synthesis. This review will focus on ammonia generation from different nitrogen-containing species (like N_2, NO, NO_3^-, and NO_2^-) *via* photocatalysis, electrocatalysis, and photoelectrocatalysis.

2.3. Photocatalysis

Solar energy is a clean and inexhaustible energy source, which has triggered the wide utilization of photocatalysis in the sector of chemical fuels. Literature evidence suggests that over the initial years, it was thought that the photoreduction of N-containing species occurs only in nature. Soil and sand samples were explored to study the effect of minerals on the photoreduction of nitrogen in nature.[68,69] Fascinated by the working mechanism of the Fe and FeMo proteins in nitrogenase enzyme reactions, chemists have designed photocatalysts that absorb light to generate electrons and protons. These electrons activate the N-containing species (N_2, NO_x, and NO_x^-), which react with protons from water to form ammonia. Brown *et al.* developed such an analog CdS: FeMo protein biohybrid, which can reduce nitrogen to ammonia upon light activation.[7] CdS nanocrystals act as photosensitizers, providing electrons to the FeMo protein for nitrogen reduction. In this work, light is used as the energy source, whereas in the biological nitrogenase system energy is acquired by hydrolysis of ATP. Researchers have extended this know-how to design other photocatalytic systems like metal oxides,[70,71] metal sulfides,[72] bismuth oxyhalides,[73,74] layered double hydroxides,[75,76] and carbon-based materials[77,78] for the photocatalytic synthesis of ammonia. According to the literature, the photocatalytic N_2, NO_x, and NO_x^- reductions by semiconductors occur on photoactivation, when the excited electrons move to the conduction band, leaving holes in the valence band.[79] The electrons reduce N-species to ammonia

This journal is © The Royal Society of Chemistry 2025

Chem. Soc. Rev., 2025, **54**, 5021–5080 | **5025**

while the holes participate in the water oxidation reaction. The recombination of electrons and holes is one of the significant problems in photocatalytic reactions.[80] Thus, hole scavengers are sometimes used as sacrificial agents to prevent recombination. The band gap of the materials and the position of conduction and valence bands play a significant role in photocatalysis. The reduction potentials of N_2RR, NO_xRR, and water oxidation must lie in between the conduction and valence band positions. NO_x^- (nitrates and nitrites) are common sources of pollutants in wastewater and the photoreduction of NO_x^- can help in wastewater treatment, which will be discussed in detail later in Section 7.1. The direct reduction of nitrate and nitrite wastes into ammonia is thus both economically and environmentally important. In some cases, however, the competitive hydrogen evolution reaction (HER) and reduction of NO_3^- to N_2 limits the selectivity of the ammonia produced. A detailed discussion on different classes of photocatalytic materials like metal oxides, metal nanoparticles, single-atoms, quantum dots, and their composites, which can photoreduce N-containing species to ammonia with high selectivity, will be presented in Section 4 of this review.

2.4. Electrocatalysis

Electrochemical reduction of N_2 or NO_x^- to ammonia occurs under ambient conditions, *i.e.*, at room temperature and atmospheric pressure at a specific applied voltage. Sometimes, electrochemical reactions are considered to be more energy-efficient than photochemical reactions. This is because, in photocatalysis, some of the absorbed photons remain unutilized due to the variable wavelengths of incident light sources and the recombination of electrons and protons.[81] The design of electrocatalysts is quite challenging because the activity, selectivity, efficiency, and stability depend on the choice of materials. The material structure (surface area, porosity, crystal facets) and morphology affect the turnover and yield, while the electronic properties (heteroatom doping, defect engineering) influence the active site of the catalyst.[82] The surface properties of the catalyst can affect the adsorption–desorption of N_2 or NO_x^- species, which in turn affects the bond dissociation and the consecutive hydrogenation reactions for ammonia formation. The availability of electrons and protons can also be controlled by the design of the catalyst, which might be able to suppress the competing HER reactions and also help in attaining selectivity of the ammonia, reducing the chance of obtaining lesser reduced products like NO_2^- or NO from the electroreduction of NO_3^-.

In the electrochemical experiments, initially N_2 or NO_x^- is adsorbed on the surface of the electrode in a simple electrochemical cell. Electrons supplied by the external circuit reduce the N-containing molecule, which undergoes subsequent hydrogenation by the protons to produce ammonia. In most cases, water present in the reaction medium acts as the source of hydrogen for ammonia production. A judicious choice of electrolyte is crucial for electrocatalytic reactions because the electrode reactions of the electrochemical cell are dependent on the electrolyte. In past years, aqueous and non-aqueous electrolytes have been used where protons (H^+), hydroxides (OH^-), oxides (O^{2-}), and nitrides (N^{3-}) act as mobile charge carriers. The main bottlenecks in electrocatalytic ammonia synthesis are the yield and the Faradaic efficiency (FE). Competing reactions on the surface of electrocatalysts, like water reduction to hydrogen evolution reaction (HER), dominate over N_2 or NO_x^- reduction reactions (N_2RR and NO_xRR) at higher overpotentials, thus decreasing the selectivity of the product.[83] To eliminate the drawbacks, over the past few years, researchers have been working to upgrade electrocatalysis cells, electrocatalysts, electrolytes, and working potentials, which will be discussed in detail in Section 5 of this review.

2.5. Photoelectrocatalysis (PEC)

The general redox reactions for photocatalysis and electrocatalysis are similar. In PEC, these reactions become more favourable because of the combined effects, *i.e.*, electric and light energy.[84] In an electrochemical cell, N_2RR or NO_xRR occur at the cathode while water splitting occurs at the anode. The experimental setup of PEC is very similar to the electrocatalytic set-up; only in PEC, the cathode is replaced with a photocathode. The photocathode utilizes energy from a light source to provide the photovoltage. In this way, the electrical energy required for N_2RR and NO_xRR either decreases to a certain extent or is completely diminished depending on the Fermi level of the photocathode.[49] Generally, in PEC a three-electrode set-up is employed where the catalyst is loaded on the working electrode (photocathode).[36] The reduction reactions (N_2RR or NO_xRR) occur at the photocathode and water splitting at the anode (counter electrode). A proton exchange membrane is placed between the cathode and anode, which ensures only protons are supplied to the cathodic side for ammonia formation, and no other oxidative species can migrate to the cathodic part so that the ammonia produced does not undergo any oxidation. In photocatalysis and electrocatalysis, the competing HER reduces the Faradaic efficiency (FE) of NH_3. In PEC, the competing HER can be suppressed using photoelectrodes. For instance, an Au-decorated ordered silicon nanowire array photocathode can perform NO_2RR to NH_3 with FE as high as 95.6% at 0.2 V *vs.* RHE.[85] This is because the Au and Si surfaces of the electrode are not active for water reduction. The absence of the competing HER makes the FE for NH_3 production comparatively higher. The PEC reaction mechanisms of N_2RR and NO_xRR are similar to photocatalysis and electrocatalysis. The design of materials for PEC follows the same principles as electrocatalysts and photocatalysts. Improvement in the photoelectrocatalytic NH_3 yield and selectivity can be achieved by modification of the catalysts such as, doping with heteroatoms, making heterojunctions, defect engineering, and modification of morphology.[86–88] Thus, we can infer that the structures and properties of the materials used for designing the catalysts have profound roles in the catalytic reactions and products formed. Section 6 of this review will extensively discuss the emergent low-dimensional materials for photoelectrocatalytic ammonia synthesis.

5026 | *Chem. Soc. Rev.*, 2025, **54**, 5021–5080

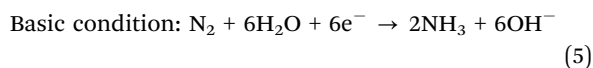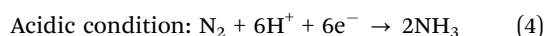This journal is © The Royal Society of Chemistry 2025

Among the above-mentioned ammonia synthesizing techniques, the most widely used methods in recent literature include photocatalysis, electrocatalysis, and photoelectrocatalysis. These processes are more sustainable and easily achievable and only require catalyst materials and energy sources to produce ammonia. Though all these processes follow the general principles of catalysis, however, the reaction conditions, mechanisms, and catalyst design differ. To get a brief idea about the working principles, catalysts, reaction mechanisms, benefits and drawbacks, and environmental impact, a comparative study of these processes is presented in Table 2 and Fig. 3.

2.6. Reaction mechanisms of N_2 reduction to NH_3

The reaction of catalytic reduction of dinitrogen (N_2) to ammonia (NH_3) using natural ingredients like air and water is proposed to be as follows (eqn (3)–(5)):[79,89]
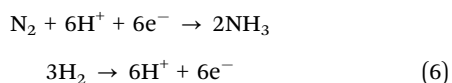
$$N_2 + 3H_2O \xrightarrow{\text{Catalyst}} 2NH_3 + 1.5O_2 \qquad (3)$$

The half-cell N_2 reduction in the acidic and basic media can be depicted as follows:[36,90]

$$\text{Acidic condition: } N_2 + 6H^+ + 6e^- \rightarrow 2NH_3 \qquad (4)$$

$$\text{Basic condition: } N_2 + 6H_2O + 6e^- \rightarrow 2NH_3 + 6OH^- \qquad (5)$$
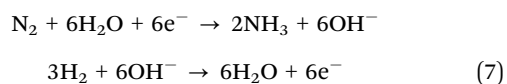
The reactions (eqn (6)–(9)) for the reduction of N_2 to NH_3 can change with the reaction medium and charge carriers as follows:[15]

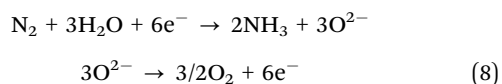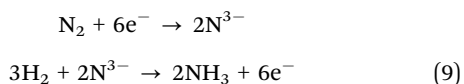a. In the presence of H^+

$$N_2 + 6H^+ + 6e^- \rightarrow 2NH_3$$

$$3H_2 \rightarrow 6H^+ + 6e^- \qquad (6)$$

b. In the presence of OH^-

$$N_2 + 6H_2O + 6e^- \rightarrow 2NH_3 + 6OH^-$$

$$3H_2 + 6OH^- \rightarrow 6H_2O + 6e^- \qquad (7)$$

c. In the presence of O^{2-}

$$N_2 + 3H_2O + 6e^- \rightarrow 2NH_3 + 3O^{2-}$$

$$3O^{2-} \rightarrow 3/2O_2 + 6e^- \qquad (8)$$

d. In the presence of N^{3-}

$$N_2 + 6e^- \rightarrow 2N^{3-}$$

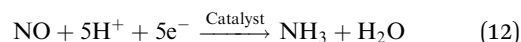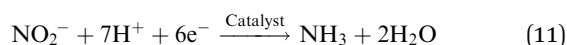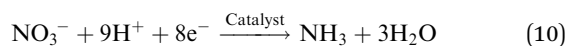$$3H_2 + 2N^{3-} \rightarrow 2NH_3 + 6e^- \qquad (9)$$

In all reaction conditions, dinitrogen reduction to ammonia is a six-electron reduction reaction, which is a kinetically "uphill" process. The design of photo- and/or electrocatalysts plays a vital role as they provide an alternative lower energy pathway to the production of ammonia. Nitrogen is a highly stable molecule owing to its triple bond and breaking the first bond is considered the rate-determining step. The mechanism of N_2 reduction to ammonia is currently being investigated by

different research groups and studies are still underway. It has been proposed that there are two possible pathways for N_2 reduction to NH_3: (i) associative and (ii) dissociative (Fig. 4A).[36,91] In the dissociative pathway, the N–N bond breaks before hydrogenation. However, this process is highly energy-demanding and the dissociative pathway is not considered favourable. In the associative mechanism, the first step involves the protonation of N_2. Protonation depends on the configuration of N_2 and can be either to the distal N atom, forming N_2H^* species, or to the two N atoms which can alternatively form $N_2H_2^*$ species. In the associative distal pathway, the reaction proceeds via three consecutive hydrogenation steps, forming one NH_3 molecule. Then, hydrogenation occurs at the second N atom, forming NH_3 after three more steps. In the associative alternating pathway, hydrogenation occurs alternately at both N atoms, and two molecules of ammonia are produced almost simultaneously. Photocatalytic and electrocatalytic reduction of N_2 to ammonia can follow any of these pathways, though simple calculations are not enough to predict the exact reduction pathway.

2.7. Reaction mechanisms of NO_x^- and NO_x reduction to NH_3

As discussed above, the bond dissociation energy of N_2 is very high (~ 941.8 kJ mol^{-1}). In comparison, the bond dissociation energies for NO_x and NO_x^- species are lower. They can be disintegrated into deoxygenated species with a lower bond dissociation energy (for $NO_3^- \sim 204$ kJ mol^{-1}); hence, nitrogen oxides can offer a sustainable route to the synthesis of ammonia at a lower energy cost. Also, the valence states of N in nitrogen oxides are higher (+5 in NO_3^-, +3 in NO_2^-) than in dinitrogen where the valence state of N is 0; hence, deep reduction reactions are more plausible in the case of nitrogen oxides. The catalytic reactions are similar to that of dinitrogen but require a different number of electrons and protons for each species (eqn (10)–(12)).[92]

$$NO_3^- + 9H^+ + 8e^- \xrightarrow{\text{Catalyst}} NH_3 + 3H_2O \qquad (10)$$

$$NO_2^- + 7H^+ + 6e^- \xrightarrow{\text{Catalyst}} NH_3 + 2H_2O \qquad (11)$$

$$NO + 5H^+ + 5e^- \xrightarrow{\text{Catalyst}} NH_3 + H_2O \qquad (12)$$

Nitrates and nitrites are present in the form of electrolytes for the electrocatalytic reduction, which involves 8e$^-$ and 6e$^-$ respectively for the conversion to ammonia. The reduction proceeds via the dissociation of NO_x^- species into deoxygenated species followed by hydrogenation, which is quite similar to the adsorption–desorption mechanism of nitrogen reduction. The reduction of nitrogen oxide species to ammonia is illustrated in Fig. 4B and it exhibits multi-step processes of electron and proton transfer.[93,94] Initially, NO_3^- is adsorbed on the catalyst surface as $*NO_3^-$, which is followed by the loss of an electron to form $*NO_3$. This $*NO_3$ intermediate is then converted into $*NO_2$ via the transfer of two electrons and two protons. In most cases, the reduction of nitrate to nitrite is the rate-determining step for NO_3^- reduction. The $*NO_2$

This journal is © The Royal Society of Chemistry 2025

Chem. Soc. Rev., 2025, **54**, 5021–5080 | **5027**

Table 2 Comparison among photocatalysis, electrocatalysis, and photoelectrocatalysis methods used for ammonia synthesis by LDM-based catalysts

Factors	Photocatalysis	Electrocatalysis	Photoelectrocatalysis
Energy source	Solar energy (light)	Electrical energy	Light and electrical energy
Catalyst materials	Semiconductors, metallic nanoparticles, plasmonic materials, quantum dots, metal oxides, single-atoms, carbon-based materials	Metals, alloys, metallic oxides, single-atoms, carbon-based materials, MXenes, transition metal dichalcogenides	Heterostructures composed of photo-catalysts and electrocatalysts
Design of catalytic systems	i. Band gap engineering.	i. Good conductivity and corrosion resistance.	i. Heterostructures of photocatalysts and electrocatalysts for simultaneous light and electrical energy utilization.
	ii. Efficient charge separation.	ii. Electrode surface modification to adsorb reactants and intermediates.	ii. Interface engineering for charge transfer. Catalyst engineering with photo- and electrocatalysts.
	iii. Surface area modification for better light absorption and adsorption of N_2/NO_x.	iii. Electrode porosity for better mass transfer.	iii. Reactor design for efficient light and electrical energy distribution.
	iv. Catalyst engineering *via* the introduction of defects, doping, cocatalysts, heterojunction and heterostructure formation, particle size, and morphology modification.	iv. Catalyst engineering *via* the introduction of defects, doping, cocatalysts, facets, heterojunction, and heterostructure formation.	
		v. Good electrolytes to enhance ionic conductivity.	
Reaction mechanism	i. Light absorption leads to the separation of electron–hole pairs and photoexcitation of electrons from the valence band to the conduction band.	i. Application of electric potential.	i. Light absorption and electric potential generate required charge carriers for photoelectrocatalysis.
	ii. Electrons in the conduction band reduce $N_2/NO/NO_2^-/NO_3^-$ to form NH_3.	ii. Electrons reduce $N_2/NO/NO_2^-/NO_3^-$ to NH_3 at the cathode.	ii. Synergistic effects enhance electron transfer.
	iii. Holes oxidize water or other organic reactants.	iii. Efficient electron transfer at electrode surface facilitated by catalysts.	iii. Optimization of photo- and electrical parameters for efficient reduction of $N_2/NO/NO_2^-/NO_3^-$ at the photocathode.
		iv. The oxidation half-reactions occur at the anode.	
Cost	Low	High	High
Efficiency	Low	High	Low
Advantages	i. Light energy can be harnessed from abundant solar energy.	i. Ammonia production with high efficiency and greater selectivity.	i. Combined advantages of photo- and electrocatalysts.
	ii. Low operational cost.	ii. Reaction parameters can be controlled and adjusted easily for electrocatalytic processes.	ii. Potential for synergistic reactions.
	iii. Sustainable synthesis of ammonia due to reduced greenhouse gas emissions.	iii. Lower dependency on weather conditions as electric energy can be produced on demand.	iii. Flexible reaction conditions.
Disadvantages	i. For solar-powered photocatalytic reactions, ammonia production is dependent on regions with high solar irradiance.	i. Requires electrical energy, which is sometimes harnessed from non-renewable sources.	i. Complexity of system design.
	ii. Efficient light absorption and conversion are required.	ii. Electrode degradation with time.	ii. Requires optimization of both light and electrical inputs.
	iii. Long-term stability and recyclability of photocatalysts have to be considered.	iii. Higher operational costs due to electricity, maintenance, and replacement of electrochemical setup.	iii. Higher costs of photoelectrochemical setup and maintenance.
Environmental impact	i. Low environmental footprint due to reduced use of fossil fuels for photocatalytic ammonia production.	i. Dependent on electricity, sometimes produced by non-renewable energy sources.	i. Can provide an optimized balance between light and electrical energy sources and reduce environmental impact.
	ii. Minimal waste generation and greenhouse gas emissions.	ii. Emissions associated with electricity production and potential waste generation from electrode degradation.	
Future applications	i. Solar-powered green ammonia generation.	i. Potential for industrial-scale ammonia productions.	i. Hybrid systems for enhanced sustainable ammonia production under variable reaction conditions.
	ii. Potential for integration with renewable energy sources.	ii. On-grid applications.	ii. Off-grid and on-grid applications.
	iii. Off-grid applications.		

5028 | *Chem. Soc. Rev.*, 2025, **54**, 5021–5080

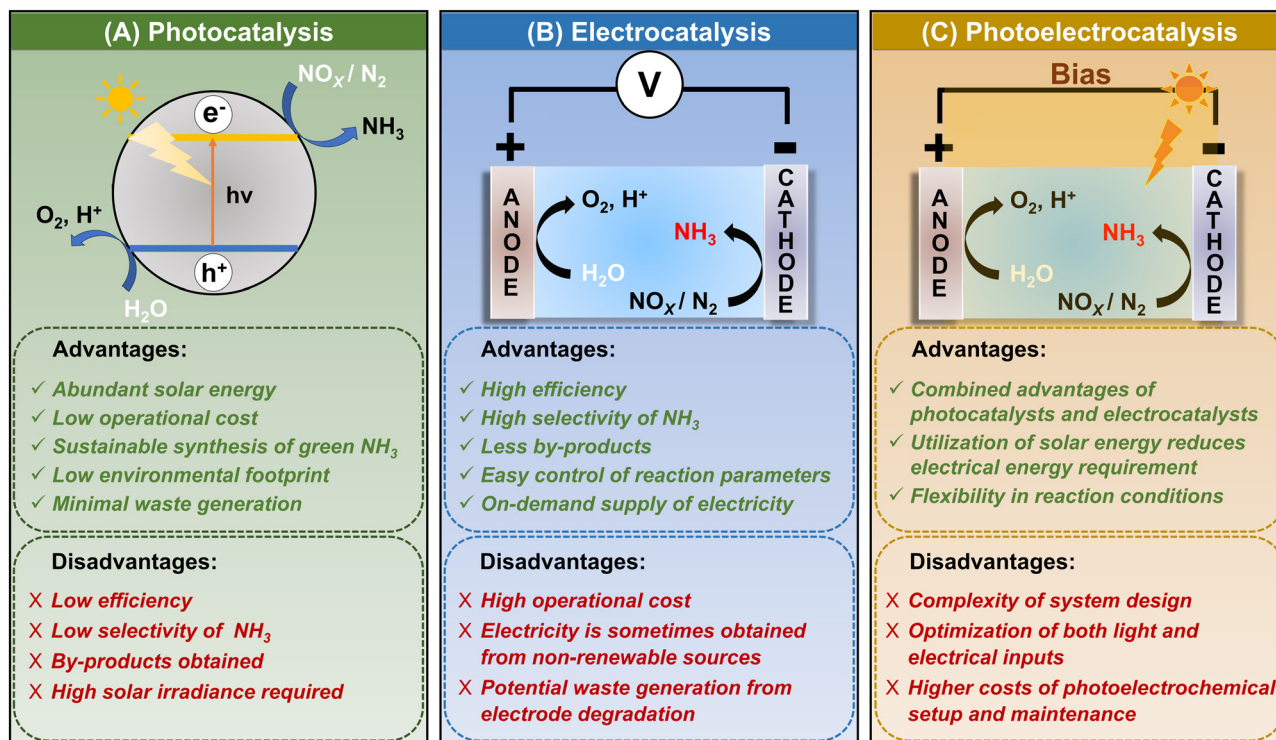This journal is © The Royal Society of Chemistry 2025

Fig. 3 Comparison of (A) photocatalysis, (B) electrocatalysis, and (C) photoelectrocatalysis methods for ammonia synthesis.

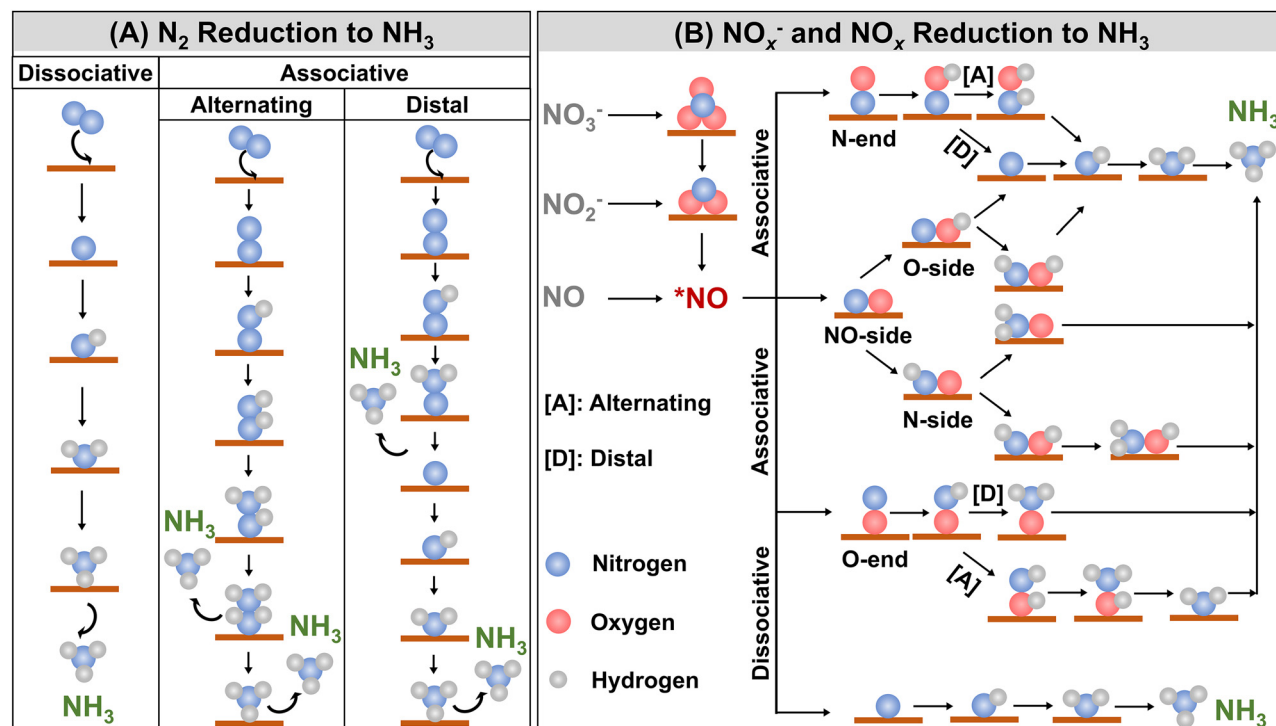**Fig. 4** General reaction pathways of ammonia synthesis. (A) N_2 reduction to ammonia *via* dissociative, associative alternating, and associative distal pathways, (B) NO_x^- and NO_x reductions to ammonia *via* associative, dissociative, alternating, and distal pathways through N- and O-ends.

intermediate is further reduced to *NO. The subsequent steps of reduction to ammonia passing through *NO intermediate is the same for NO_x^- and NO. The next possible steps can follow

either dissociative or associative pathways. In the dissociative pathway, the N–O bond undergoes dissociation, forming adsorbed nitrogen (*N) and oxygen (*O) species on the catalyst

This journal is © The Royal Society of Chemistry 2025

Chem. Soc. Rev., 2025, **54**, 5021–5080 | **5029**

surface. The *N is then sequentially hydrogenated to yield ammonia. The associative pathway can proceed through any one of the three possible routes depending on the adsorption type of *NO intermediate. The adsorption of *NO on the catalyst surface can be through (i) N-end, (ii) O-end, or (iii) NO-side. The hydrogenation of the N-end and O-end routes can again proceed through either alternating or distal hydrogenation processes. In the case of the distal-O or N hydrogenation pathway, at first one of the O or N atoms is at first fully hydrogenated to form H_2O or NH_3, followed by the hydrogenation of the other atom. For the case of the alternating-O or N hydrogenation pathway, the O and N atoms are alternately hydrogenated stepwise to form H_2O and NH_3, respectively.[94]

3. Low-dimensional materials (LDMs): dimensionality of nanostructures and heterostructures

Nanostructured materials (NSMs) can act as effective catalysts because of their morphologies, electronic properties, and surface characteristics.[95] Dimensionality is an important parameter because different dimensional materials of similar chemical composition exhibit separate physical and chemical properties. For instance, carbon has different allotropes: fullerene, carbon nanotube, graphene, and graphite. Fullerene is 0D, carbon nanotube is 1D, graphene is 2D, and graphite is 3D, and all four have different properties. NSMs have building units of size ranging from nanometer to sub-micron scale. The classification of NSMs has been proposed by Gleiter (1995) and Skorokhod (2000); later, Pokropivny and Skorokhod proposed a modified classification.[96,97] According to the classification by Pokropivny and Skorokhod, NSMs can be classified as 0D, 1D, or 2D. The structure and morphology of some common low-dimensional materials are illustrated in Fig. 5. In this review, we will explore the implementation of the NSMs and multicomponent heterostructures, which are built from the 0D, 1D, and 2D materials for photocatalytic, electrocatalytic, and photoelectrocatalytic N_2RR and NO_xRR to produce ammonia.

3.1. Zero-dimensional (0D) nanostructured materials

0D materials are mostly nano-dimensional structures with an average size of less than 10 nm along all three dimensions and are isotropic.[115] They comprise metal nanoparticles, metal alloy nanoparticles, nanospheres, core–shell structures, yoke–shell structures, quantum dots, single-atoms, nanocrystals, and metal oxides.[98–103,116] The fabrication of 0D catalysts has been well explored and various methods, such as thermal evaporation, sputtering, chemical vapour deposition, electrodeposition, solvothermal, sol–gel, annealing, galvanic replacement, gas phase deposition, and template-based methods are quite common fabrication techniques.[117,118] The optical and physicochemical properties of these 0D materials can be tuned depending on their size, making them potential catalysts for photo- and electrocatalysis reactions.

3.2. One-dimensional (1D) nanostructured materials

1D materials are nanostructured along any two dimensions while the third dimension can be in the microscale range.[115] 1D catalysts are advantageous over 0D catalysts as they offer a unique anisotropic structure, more density of active sites, and more surface area than 0D materials.[119] 0D materials are more susceptible to Ostwald ripening due to the high surface energy. In 1D nanostructures, the lower-energy facets are preferentially exposed on the surface, which reduces the surface energy of the whole material, making them more stable.[120] The structure of 1D materials enhances mass transport and diffusion, and provides them with superior catalytic properties.[121] 1D materials comprise nanowires, nanotubes, nanorods, nanoribbons, nanobelts, and nanofibers.[104–109] The most common synthetic techniques of 1D materials include hydrothermal, sol–gel, self-assembly, electrospinning, and template-assisted methods.[122–124] In this review, we will explore the recently developed 1D catalysts and how their structural and electronic properties aid in the catalytic synthesis of ammonia.

3.3. Two-dimensional (2D) nanostructured materials

In 2D materials, only one dimension is confined to the nanoscale regime while the other two dimensions can range from micrometer to centimeter scale.[115] Nanosheets, nanoplates, nanodisks, and nanoprisms are the most commonly designed 2D materials for catalysis.[76,110–114,125] These 2D nanostructures have exposed surface area, increasing their contact with reactants.[126,127] Most of the active sites are present on the surface and are easily accessible for catalysis. Defects and unsaturated sites can be introduced into the 2D structures, which enhances adsorption–desorption and facilitates mass transport.[126] In 2D materials, electrons can be trapped within the atomic layers, which brings good conductivity and electron mobility to the structures, thereby facilitating electron transport and charge carrier separation.[128]

According to Sabatier's Principle, an optimized catalytic reaction occurs when the interaction between the reactants and the catalyst surface is optimal, i.e., the adsorption energy is intermediate.[129] Thus, it can be said that the catalytic properties of a material are dependent on its surface and electronic properties.[130,131] Hence, engineering the band structure of a material proves to be an important tool in catalyst design.[132] The electronic structures of low-dimensional nanostructures differ from their bulk counterparts due to the quantum confinement of the electronic density states. As a result, the photon absorption properties of these materials are enhanced, leading to better catalytic activities in these systems.[133,134] The electronic properties are also dependent on the morphology of the materials, including kinks, edges, facets, and phases.[9] Additionally, the surface area to volume ratio is higher in the low-dimensional catalysts, which ensures the availability of more active sites on the surface of the catalyst.[9] The successful utilization of 0D, 1D, and 2D materials for catalysis has also prompted researchers to prepare hybrid structures using these

5030 | Chem. Soc. Rev., 2025, 54, 5021–5080

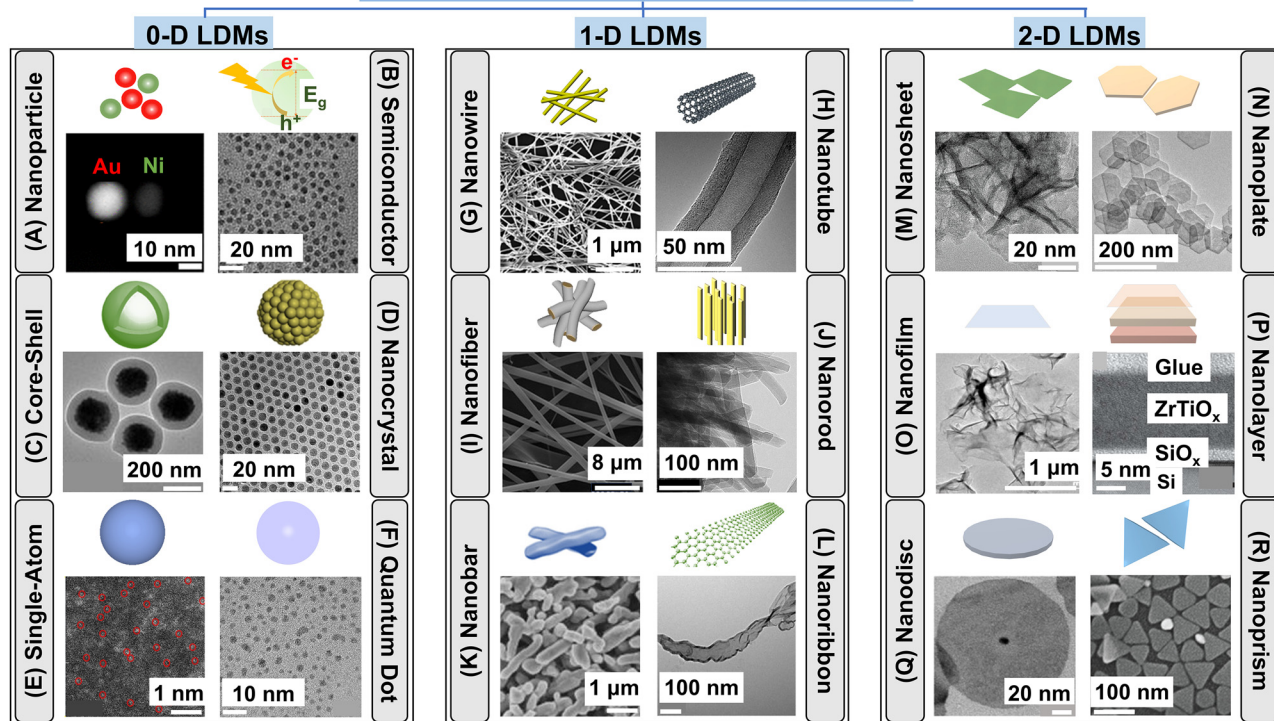This journal is © The Royal Society of Chemistry 2025

Fig. 5 Dimensional classification of low-dimensional materials (LDMs). 0D common structures. (A) Metallic nanoparticles, representative SEM image of bimetallic Au/Ni nanoparticle. Reproduced with permission from ref. 98. Copyright 2019, American Chemical Society. (B) Semiconductor nanoparticles, representative TEM image of CdS semiconductor nanoparticles. Reproduced with permission from ref. 99. Copyright 2020, American Chemical Society. (C) Core−shell structures, representative TEM image of Fe_3O_4@silica RF core−shell particles. Reproduced with permission from ref. 100. Copyright 2009, Royal Society of Chemistry. (D) Nanocrystals, representative TEM image of maghemite nanocrystals. Reproduced with permission from ref. 101. Copyright 2001, American Chemical Society. (E) Single atoms, representative HAADF-STEM image of Fe single atoms. Reproduced with permission from ref. 102. Copyright 2023, Wiley-VCH. (F) Quantum dots, representative TEM image of carbon quantum dots. Reproduced with permission from ref. 103. Copyright 2023, Royal Society of Chemistry. 1D common structures. (G) Nanowires, representative SEM image of Ag nanowires. Reproduced with permission from ref. 104. Copyright 2020, American Chemical Society. (H) Nanotubes, representative TEM image of carbon nanotube. Reproduced with permission from ref. 105. Copyright 2019, Elsevier. (I) Nanofibers, representative SEM image of Fe_2TiO_5 nanofibers. Reproduced with permission from ref. 106. Copyright 2022, Wiley-VCH. (J) Nanorods, representative TEM image of g-C_3N_4 nanorods. Reproduced, 2022, Elsevier. (K) Nanobars, representative SEM image of $LiNi_{0.4}Co_{0.2}Mn_{0.4}O_2$ nanobars. Reproduced with permission from ref. 108. Copyright 2012, Royal Society of Chemistry. (L) Nanoribbons, representative TEM image of graphene nanoribbons. Reproduced with permission from ref. 109. Copyright 2015, AIP Publishing. 2D common structures. (M) Nanosheets, representative TEM image of ZnCr-LDH nanosheets. Reproduced with permission from ref. 76. Copyright 2020, Wiley-VCH. (N) Nanoplates, representative TEM image of hexagonal $Co(OH)_2$ nanoplates. Reproduced with permission from ref. 110. Copyright 2013, Royal Society of Chemistry. (O) Nanofilms, representative TEM image of Cu-TCPP MOF ultra-thin nanofilm. Reproduced with permission from ref. 111. Copyright 2013, Royal Society of Chemistry. (P) Nanolayers, representative cross-TEM image of a-$ZrTiO_x$ nanolayers. Reproduced with permission from ref. 112. Copyright 2013, Royal Society of Chemistry. (Q) Nanodiscs, representative TEM image of Bi_2Se_3 nanodisc. Reproduced with permission from ref. 113. Copyright 2012, American Chemical Society. (R) Nanoprisms, representative SEM image of Ag nanoprisms. Reproduced with permission from ref. 114. Copyright 2024, American Chemical Society.

nanomaterials and exploit them in catalysis. Moreover, the integration of two components provides synergistic effects from each counterpart toward catalysis. These individual components of heterostructures are held together mainly *via* van der Waals forces.[9] Heterostructures have emerged as state-of-the-art catalysts as they offer superior-quality interfaces with unique properties compared to normal nanostructures. The newly formed interfaces between the components can lead to improved charge transfer, slowing down the recombination of charge carriers.[126] These heterostructures can be 0D–1D, 0D–2D, 1D–2D, 2D–2D, and so on. In the next sections, we will discuss the 0D, 1D, and 2D materials, their heterostructures,

and the interplay between the electronic properties and their catalytic activities.

4. Low-dimensional photocatalysts for ammonia synthesis

The design of photocatalysts for the reduction of N-containing species to ammonia requires a few criteria to be met: (i) adsorption of the N-containing species on the surface of the catalyst; (ii) absorption of light by the catalyst; (iii) tuning the band gap corresponding to the wavelength of light absorbed,

which can promote the excitation of electrons from the valence band to the conduction band; (iv) position of the valence and conduction bands such that the potentials of the redox reactions are aligned in the gap; and (v) recombination of charge carriers is minimum. These requirements can be fulfilled by choosing the proper catalyst from a wide range of photocatalytic materials, such as semiconductors, metal nanoparticles, metal oxides, metal sulfides, and carbon-based materials. Structural engineering of the photocatalysts *via* the introduction of defects, construction of heterojunctions, increasing surface area by hybridization with other materials, and the use of cocatalysts can enhance photocatalytic performance.

Photosynthesis of ammonia, in principle, requires only water, light, and N_2 or NO_x^- hence, it is quite attractive. However, the photocatalysts developed earlier exhibit low conversion efficiency for ammonia generation. This might be due to the availability of less active sites, limited light absorption properties, and quick recombination of photogenerated charges. Active sites adsorb and activate the N-containing substrate. The activation of N_2 is challenging due to the high dissociation energy of $N{\equiv}N$. Nitrogen has four bonding (2σ and 2π) and four anti-bonding ($2\sigma^*$ and $2\pi^*$) orbitals. Activation of N_2 requires a donation of electrons to the bonding orbitals and an acceptance of electrons from anti-bonding π^* orbitals. The thermodynamic reduction potential of N_2 to NH_3 is 0.148 V *vs.* RHE, which is quite close to the hydrogen evolution reaction (0 V *vs.* RHE), so the competing HER sometimes hinders the N_2RR, and this remains a major concern in

most cases.[135] The drawbacks of the low solubility of N_2 in an aqueous medium and the high dissociation energy required for the cleavage of $N{\equiv}N$ can be overcome by replacing the N-containing precursor from N_2 with nitrates or nitrites.[21] Moreover, high concentrations of nitrates and nitrites in wastewater can be a major health concern; thus, reducing them to ammonia can diminish health risks. However, nitrate reduction to ammonia requires $8e^-$; hence, the risk of obtaining lesser-reduced products like N_2 persists. For achieving higher NH_3 selectivity, side reactions of N_2 production and HER must be suppressed. This may be achieved by surface modification of catalysts or modification of materials based on the mechanistic pathway of ammonia synthesis.

The principle of photocatalysis relies on harvesting solar energy (Fig. 6). Hence, the band gap of the catalysts should also be tuned for direct utilization of solar light, preferably visible light. However, the band gap tuning sometimes reduces the energy of photogenerated electrons and, thereby, their reduction capability.[136] Hence, developing an optimized photocatalyst that effectively absorbs light while maintaining its reduction capability is essential. For activation of N-containing molecules, the active sites must be electron-rich and able to promptly transfer electrons to adsorbed N-containing moieties. Inducing defects and unsaturated sites with abundant localized electrons in the catalysts can address this issue as they effectively transport electrons, and consequently, activate and reduce the N-containing moieties. The synthetic and modification strategies of LDMs are mostly
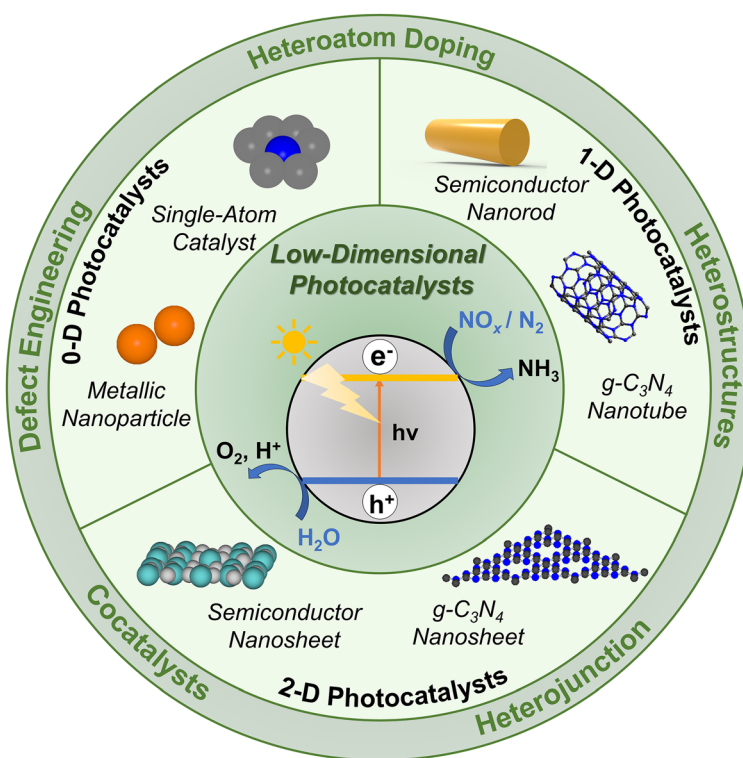

Fig. 6 Low-dimensional photocatalysts for ammonia synthesis. Classification of photocatalysts into 0D, 1D, and 2D, and schematic representations of few selected photocatalytic LDMs.

5032 | *Chem. Soc. Rev.*, 2025, **54**, 5021–5080

This journal is © The Royal Society of Chemistry 2025

simple and single-step, but structure engineering of the catalysts and the formation of heterostructures sometimes require multi-step fabrication strategies. 0D photocatalysts like metal and metal oxides mostly rely on different reduction methods of metallic salts, like photoreduction, H_2 reduction, or chemical reduction, whereas single-atom-based photocatalysts use different deposition techniques for integration with support materials.[137–141] Fabrication of 1D materials based on metal oxide, metal oxyhalides, and carbon-based materials mostly uses different thermal treatment procedures like hydrothermal, solvothermal, and annealing.[142–144] 2D materials based on semiconductor nanosheets, graphitic carbon nitrides, and graphdiynes rely on different thermal synthetic procedures.[145–148] The catalytic properties of these materials can be enhanced by defect engineering like the introduction of vacancies,[43] doping of heteroatoms,[71] formation of heterojunctions,[149] heterostructures,[150] and use of cocatalyst materials.[146] The fabrication strategies of the most widely used 0D, 1D, 2D, and heterostructured photocatalysts are presented in Table 3. This section will explore the emergent low-dimensional photocatalysts (Fig. 6) used recently to convert N_2, NO_x, or NO_x^- to NH_3.

4.1. 0D photocatalysts and heterostructures

0D photocatalysts for ammonia synthesis mainly consist of three classes of materials: semiconductor nanoparticles, quantum dots, single-atoms, and heterostructures formed with these 0D particles. Due to their plasmonic properties, 0D structures prove to be effective catalysts because the photons can be harvested at lower energy by nanoparticles, and their adsorption properties can be easily tuned by altering their shape and architecture.[9] The separation of charge carriers is also possible because of the strong electric fields created at local "hotspots" induced by surface plasmons.[173] These properties allow the 0D materials to be incorporated with 1D or 2D materials to create heterostructures that can function as efficient photocatalysts for ammonia synthesis.

Metallic nanoparticles have plasmonic properties and their size and shape can be easily tuned, making them important materials for catalysis. Quantum dots also prove to be promising photocatalytic materials owing to their unique characteristics like high absorption coefficient, efficient charge transfer properties, large surface-to-volume ratio, and stability. Single-atoms are another class of materials that have recently emerged as prospective photocatalysts due to their highly efficient atom economy, low coordination environment, unique electronic structural properties, and atomic-level understanding of reaction mechanisms. Metallic nanoparticles, quantum dots, and single-atoms, upon heterogenization with different 1D and 2D support materials, can produce excellent photocatalysts for ammonia synthesis. For instance, the well-explored TiO_2 nanosheets can be used as substrates for incorporating metallic nanoparticles, metal oxide nanoparticles, and single-atoms, which can simultaneously modify the interface as well as act as active sites for catalysis. The heterostructures formed are mostly of dimension 0D–2D. Heterostructures of semiconductors like TiO_2 and CdS decorated with metallic

nanoparticles act as efficient photocatalysts for ammonia generation from N-containing species like N_2 and NO_x.[174–176] Ideally for NO reduction reactions, a high concentration ($>10\,000$ ppm) of NO is required for photoproduction of ammonia. However, limited NO conversion and ultra-low solubility of NO in water (1.94 ± 0.03 mmol L^{-1} at 25 °C) are the major bottlenecks for NO conversion to NH_3.[177] To address these challenges and for direct photocatalytic conversion of NO, Fe(II)EDTA is employed as the NO chemical absorbent, forming Fe(II)EDTA–NO chelates, and formaldehyde (HCHO) acts as the antioxidant to prevent the formation of Fe(III) from Fe(II) oxidation.[137] TiO_2 decorated with Au nanoparticles are adorned with active sites to facilitate photogenerated charge separation, thereby promoting ammonia generation. The simultaneous chemical adsorption and photocatalytic reduction system enable continuous NO adsorption, NO reduction, and Fe(II)EDTA regeneration on-site. Notably, the efficiency of NO conversion and the selectivity of ammonia produced remain unaffected even in the presence of H_2O, SO_2, and metal ions (K^+, Ca^{2+}, Cd^{2+}, and Pb^{2+}). In flue gas, the simultaneous presence of NO and SO_2 presents certain challenges of removal and recovery. SO_2 is soluble and easily oxidized, hence, SO_2 acts as a potential reductant in the NO photoreduction reaction. The formation of the SO_2–NO redox pair promotes easy conversion of both NO and SO_2 in continuous flow.[178] Thus, high selectivity is achieved simultaneously for both NO-to-NH_3 upcycling (97%) and SO_2-to-SO_4^{2-} purification (92%). Metallic nanoparticles or bimetallic nanoalloys-loaded TiO_2, such as Cu/TiO_2 and Cu–Pd/TiO_2, in the presence of hole scavengers like oxalic acid and methanol, can perform photocatalytic $8e^-$ conversion of NO_3^- to NH_3 without forming N_2 while simultaneously producing H_2, which lowers the selectivity of NH_3.[138,139] To address this problem, subnanometric metal oxide nanoparticles like BaO, CaO, and MgO are synthesized *in operando* on the TiO_2 nanosheets.[154] *In operando* growth of 0D subnanometric metal oxide nanocrystals (MO_{NC}) at the oxygen defect sites of TiO_2 nanosheets promotes NO_3^- reduction to synthesize NH_3 selectively. The construction of MO_{NC} at defect sites is preferable because, due to the limited number of electron lone pairs, the nanocrystals cannot undergo further agglomeration. These MO_{NC}@OVs act as active sites for the $8e^-$ photoreduction of NO_3^- to NH_3. Water splitting, the primary side reaction, produces trace amounts of H_2. However, theoretical calculations indicate that the activation energy of NO_3^- reduction is 1.42 eV less than water splitting, favouring NO_3^- reduction over the side reaction of water splitting. Compared with the HER, the selectivity of NH_4^+ has been reported to be 97.67%. The formation of a unique interface between metal oxides and TiO_2 promotes charge separation as well as charge transfer properties of the hybrid catalyst. The light absorption property of the catalyst is improved and the conduction band is also elevated, enhancing the photocatalytic performance of NO_3^- reduction. A similar work along these lines features the *in situ* formation of dynamic Cu_2O sub-nanoclusters on TiO_2 nanosheets (TNS) as the ammonia-producing photocatalyst.[155] This work introduces a different

This journal is © The Royal Society of Chemistry 2025

Chem. Soc. Rev., 2025, **54**, 5021–5080 | **5033**

Table 3 Synthetic and modification techniques for selected ammonia generating low-dimensional photocatalysts

Classification	Materials	Photocatalysts	Synthesis/Modification	Ref.
0D LDMs and heterostructures	Metallic nanoparticles (NPs)	Au_{NPs}–TiO_2	In operando photodeposition	137
		Pd/Cu/Ag–TiO_2	H_2 reduction	138
		CuPd–TiO_2	Chemical reduction	139
		Ru–g-C_3N_4	Green tea reduction	151
		Ru–ZrO_{2-x}	Impregnation method	152
		Ru–$K_2Ta_2O_{6-x}$	Thermal decomposition	153
	Metal oxide nanocrystals (NCs)	MO_{NCs}–TiO_2 (M = Mg, Ca, Sr, Ba)	In operando photodeposition	154
		Cu_2O_{NCs}–TiO_2	In operando photodeposition via pseudo-Fehling's reaction	155
	Quantum dots (QDs)	TiO_2QDs–Fe_3S_4	Heterojunction formation	149
		$Bi_2Ti_2O_7$ QDs	Defect engineering via hydrothermal method	156
		InP QDs	Organometallic reactions, ligand exchange	157
	Single-atoms (SAs)	Ru SA–H_xMoO_{3-y}	Defect engineering, H-spillover method	43
		Ru SA–CeO_2	Impregnation-calcination	158
		Ru_1 SA–d-UiO-66	Defect engineering, photochemical deposition	140
		Pt_1 SA–BiOBr	Defect engineering, photochemical deposition	141
1D LDMs and heterostructures	Carbonaceous materials	g-C_3N_4	Defect engineering via molten-salt method	107
		Ti^{3+}–TiO_2/HAp-C	Thermal annealing and reduction	142
	Metal oxides	MoO_{3-x} NWs	Defect engineering via hydrothermal method	143
		Cu_2O NPs–$W_{18}O_{49}$ NWs	Defect engineering, in situ reduction, heterojunction formation	150
		CdS NPs–WO_3 NRs	Heterojunction formation	159
	Metal oxyhalide	Bi_5O_7Br NTs	Defect engineering, thermal treatment	144
	Pyrochlore	Bi NPs–$Bi_2Sn_2O_7$ NWs	Defect engineering, heterojunction formation, hydrothermal treatment	160
2D LDMs and heterostructures	Metal oxides	B-TiO_2 NS	Hydrothermal treatment, B-doping	145
		C-TiO_x NS	Bottom-up substitutional C-doping	71
		Ru NPs–$W_{18}O_{49}$	Defect engineering via hydrothermal method, chemical reduction	161
		Sb–MoO_{3-x} NS	Defect engineering, Sb-doping, heat treatment	162
	Metal oxyhalides	M–BiOBr NS (M = Fe, Mo, Ni)	Defect engineering, metal doping, hydrothermal treatment	73
		Bi NPs–BiOBr nanoplates	Schottky-junction formation, solvothermal reaction	146
		Co–BiOCl nanoplatelets	Co-doping, hydrothermal treatment	44
	Graphitic carbon nitrides	B-C_3N_4 NS	B-doping, thermal treatment	77
		Ni_3B NPs–V_N–C_3N_4 NS	Defect engineering, Schottky junction, chemical reduction, electrostatic self-assembly	163
		B-C_3N_5 NS	Defect engineering, B-doping, thermal polymerization	147
	Graphdiynes (GDYs)	GDY-Fe_3O_4	Modified Glaser–Hay coupling, microwave-hydrothermal approach	148
		GDY-CoO_x QD	In situ growth-deposition	164
Organic framework-based heterostructures	Porous-organic frameworks (POFs)	MPc-POF (M = Fe, Co, Zn)	Schiff base reaction, solvothermal reaction	165
	Covalent-organic frameworks (COFs)	Porphyrin COF-Au SA	Thermal reactions	166
		DPPCOOH-COF	Schiff base condensation reaction	167
		Bi/COF-TaTp	Solvothermal reactions	168
	Metal-organic frameworks (MOFs)	MIL-100 (Fe) MOF	Defect engineering of ligands, nonthermal plasma-assisted synthesis	169
		Ca^{2+}-d-UiO-66 MOF	Ca^{2+}-doping, ligand incorporation, solvothermal reaction	170
		MXene-MIL-125(Ti) MOF	In situ etching, delamination heterojunction formation, ligand pre-coupling	171
		NH_2-MIL-125 MOF-$Co(OH)_2$-ZIF-8	Heterojunction formation, nanoarchitectonics, solvothermal reactions	172

5034 | Chem. Soc. Rev., 2025, 54, 5021–5080

This journal is © The Royal Society of Chemistry 2025

approach to ammonia formation, utilizing dynamic Cu_2O nanoclusters following pseudo-Fehling's reaction. The structure of Cu_2O is unstable under photocatalytic working conditions. Hence, dynamic reconstruction of active Cu_2O sites is required to perform the photocatalytic reactions using actual Cu_2O. The novel active Cu_2O sub-nanoclusters are constructed on-site utilizing photoinduced pseudo-Fehling's reaction in a photocatalytic system containing redox pairs of Cu^{2+} and reducing sugars (formaldehyde and formic acid). The photogenerated electrons (e^-) and holes (h^+) participate in the Cu^{2+} to Cu_2O reduction and HCHO to HCOOH oxidation for the formation of Cu_2O NCs and construction of Cu_2O–TNS interface, respectively. The value-added oxidation of HCHO to HCOOH is accompanied by synchronous reduction of different N-sources (NO_3^-, NO_2^-, and NO) to value-added NH_3 by the active dynamic Cu_2O sites. This strategy ensures the formation of realistic dynamic active sites and provides a better understanding of the reaction mechanisms underlying the photocatalytic reactions. The photoactivity of TiO_2 semiconductor nanoparticles can also be enhanced by doping with heteroatoms. Co-doping of TiO_2 with synergistic transition metals $Ce^{3+/4+}$-cation and S^{2-}-anion adjusts the band gap of TiO_2 such that maximum photoactivity is obtained upon visible light irradiation.[179] The ratio of Ce^{3+}/Ce^{4+} is adjusted with hydrazine to form oxygen vacancies (V_O), which helps maintain the charge and lattice electroneutrality of the TiCeOS catalyst. The Ce^{3+} centers act as the active sites for the adsorption and activation of N_2 while the electron-hopping between heterovalent Ce^{3+}/Ce^{4+} promotes electron transfer for the photoreduction of N_2. Simultaneously, the V_Os act as the active sites for trapping water molecules and subsequent proton generation from water to protonate N_2 to NH_3. The introduction of metallic nanoparticles like Ru can tune the band gap of the photocatalytic materials, boost electron transfer, and facilitate charge separation. Ru-modified g-C_3N_4 in the presence of visible light can selectively photoreduce NO_3^- to NH_3.[151] The theoretically calculated activation energy for the rate-determining step of NH_3 synthesis is 0.75 eV, which is much less when compared to the activation energies of competing HER (0.98 eV) and N_2 synthesis (1.36 eV), making the generation of NH_3 more selective. The Ru sites have more Bader charge; hence, the density of electrons is higher on the Ru atoms, making them the active sites for photocatalysis. Ru nanoparticles can also act as cocatalysts for ammonia production when loaded on defective semiconductor-based ZrO_{2-x} nanoparticles with oxygen vacancies (V_O).[152] The defective ZrO_{2-x} nanoparticles have a narrow band gap, and excellent reducing and electron donation properties, which makes it an outstanding photocatalyst for ammonia generation. The V_Os stabilize the dispersed Ru nanoparticles, which act as cocatalysts and pose an upward band bending of ZrO_{2-x}, inducing an interfacial Schottky barrier that promotes the separation of photogenerated charge carriers. The Schottky barrier at the Ru and ZrO_{2-x} interface also provides a unidirectional pathway for photogenerated electron transport. The Ru nanoparticles trap these electrons, thereby ensuring the supply of requisite electrons for N_2 reduction to NH_3. Ru nanoparticles

loaded on defective perovskite and pyrochlore structures can also promote N_2 photoreduction to NH_3.[153] In this work, different perovskite- and pyrochlore-structured tantalates with low-valent Ta and abundant oxygen vacancies (V_O) were fabricated by high-temperature solid-state reduction. These visible light active dark tantalates have narrow band gaps and upon the introduction of Ru nanoparticles, band bending occurs to construct an interfacial Schottky barrier. The Schottky barrier promotes adsorption of N_2 molecules and electron transfer to reduce N_2 to NH_3. Among all the synthesized tantalates, Ru-loaded defective pyrochlore $K_2Ta_2O_{6-x}$ has the highest electron-donation properties and chemical stability, and therefore is most effective for ammonia photosynthesis in the gas–solid phase at low pressure.

0D quantum dots (QDs) also prove to be efficient photocatalysts for ammonia production. TiO_2 nanoparticles are one the most widely used semiconductors for photocatalytic applications. Controlling the size of the nanoparticles and reducing them to below 10 nm creates TiO_2 QDs with outstanding photocatalytic properties owing to enhanced charge separation, modified textural properties, and altered redox potentials.[149] Upon the formation of an S-scheme heterojunction of TiO_2 with photoactive Fe_3S_4 crystalline spinels, the photofixation of N_2 to produce NH_3 is boosted in the presence of simulated sunlight. This enhanced photocatalytic activity is attributed to the heterojunction formation, which leads to more visible light absorption, accelerated photoinduced charge separation, and enhanced catalyst surface area. Formation of an S-scheme heterojunction between 0D g-C_3N_4 QDs and 3D macro- and mesoporous TiO_{2-x} with oxygen vacancies (V_O) and enhanced charge transfer properties promotes the photo/electrocatalytic reduction of NO to NH_3.[180] The photogenerated charge carriers are migrated by the S-scheme heterojunction formed in the g-C_3N_4 QDs/3D-TiO_{2-x} and the accumulated electrons in the conduction band of g-C_3N_4 quantum dots reduce NO to NH_3. Pyrochlore $Bi_2Ti_2O_7$ QDs with oxygen vacancies (V_Os), produced hydrothermally from bismuth nitrate and titanium sulfate also produce NH_3 from N_2 upon photoirradiation.[156] When ammonia production is compared with $Bi_2Ti_2O_7$ nanosheets, the QDs are found to be more photoactive. Despite possessing the same amount of V_Os, the QDs are found to be more photoactive as the synergistic roles of shallow levels arising from V_O of $Bi_2Ti_2O_7$ QDs and the quantum confinement effect promote adsorption and activation of N_2 molecules to produce NH_3. Ammonia production is also possible from nitrate (NO_3^-) and nitrite (NO_2^-) anions using visible-light-active indium phosphide (InP) quantum dots.[157] InP QDs have tuneable absorption properties, high charge separation abilities, efficient mobility of charge carriers, and flexibility in modifying the surface chemistry. The photoexcited charge carriers generated by the III–V InP QDs directly induce NO_3^- reduction to produce NH_3. The kinetic experiments from this study confirm that the reduction of NO_3^- to NO_2^- is the most energy-demanding rate-determining step in the conversion of NO_3^- to NH_3. The conversion of NO_2^- to NH_3 is faster and almost 100% conversion is achieved in this step. Additionally, in this study, water is used as the source of protons for ammonia production.

This journal is © The Royal Society of Chemistry 2025

Chem. Soc. Rev., 2025, **54**, 5021–5080 | **5035**

Single-atom (SA)-based catalysts are one of the emergent classes of materials currently undergoing widespread investigation. Compared to nanoparticles, single-atoms provide access to a higher density of active sites and contribute to better atomic usage, which in turn escalates the catalytic process.[27,43] The high catalytic activity, selectivity, and stability of SA catalysts can also be attributed to homogeneity and the low coordination capability of the single-atoms.[181] The Ru SAs can tune the electronic structure of the oxygen vacancies present in TiO_2 and improve the adsorption of N_2 for photocatalytic N_2RR. The synergistic effect of the two active sites, Ru SA and oxygen vacancies (V_OS) powers the N_2RR, demonstrating that both components of the heterostructures participate in the catalytic reaction. For Ru SAs on CeO_2 support, CeO_2 generates electron–hole pairs upon photoirradiation and the Ru sites pull the electrons toward them, accumulating photogenerated electrons around the Ru sites (Fig. 7A–E).[158] This further modulates the local electron density of the adsorbed N_2 molecules on Ru sites, lowers the energy barrier of the rate-limiting step, and, thereby, promotes the hydrogenation of adsorbed N_2 via the associative distal pathway. Ru SAs have also been implanted on

other supports like molybdenum oxides and metal–organic frameworks to photocatalytically synthesize ammonia by N_2RR. Here, the active single Ru site anchored on the UiO-66 nodes participates in producing ammonia (Fig. 7F–I).[140] Ru SAs can be embedded in TiO_2 by electronic metal–support interactions, and this catalytic system eradicates the use of external sacrificial agents for producing ammonia (Fig. 7J–M).[182] Pt SAs with tuneable oxidation states photodeposited on a BiOBr support with oxygen vacancies (V_OS) can also efficiently produce ammonia upon photoirradiation.[141] The electron–metal support interactions (EMSI) between the Pt and BiOBr and the tuneable oxidation state of Pt SA promote charge transfer between the modifiers (V_O and Pt SA) and the BiOBr support. The accelerated electron transfer and variation of the local electronic structure of V_O by Pt SA leads to selective adsorption and activation of N_2 as well as the reduction of the energy barrier of the rate-limiting step, and promote hydrogenation of $*N_2$ intermediate to produce NH_3 via a multielectron alternating reduction pathway. It is to be noted that though most of the reported SA photocatalysts use noble metals, the metal utilization efficiency of single-atoms in catalysis lowers the cost of noble
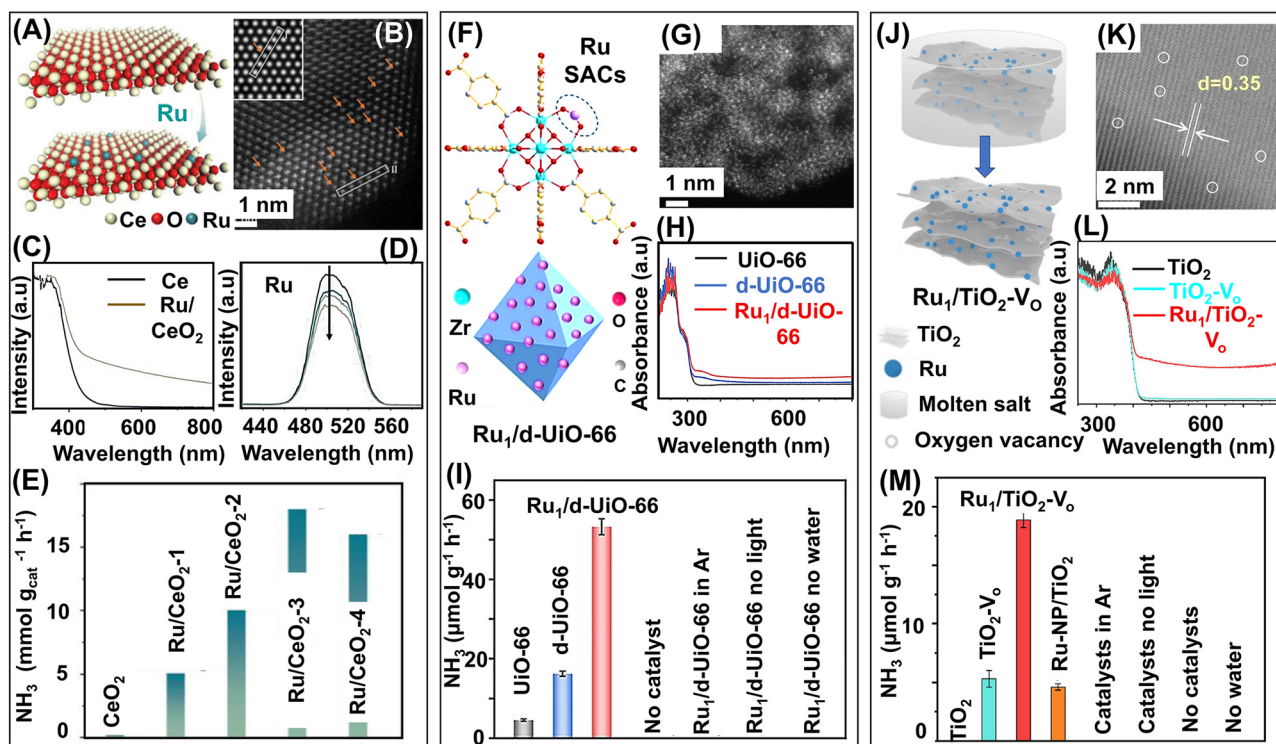

Fig. 7 Zero-dimensional (0D) photocatalysts for ammonia synthesis. (A) Schematic representation of the isolated 0D Ru sites anchored on CeO_2. (B) HAADF-STEM image of Ru–CeO_2. The inset features the corresponding simulated STEM image. (C) UV-Vis DRS of CeO_2 and Ru–CeO_2. (D) PL spectra of Ru–CeO_2 with different Ru loadings. With an increase in Ru loading the PL intensity decreases. (E) NH_3 yield comparison for CeO_2 and Ru–CeO_2 catalysts with different Ru loadings. The maximum yield obtained is 18 mmol g_{cat}^{-1} h^{-1} for Ru/CeO_2-3 where the Ru loading is 1.87%. Reproduced with permission from ref. 158. Copyright 2024, Wiley-VCH. (F) Schematic representation of the 0D Ru single-atom in the Ru_1/d-UiO-66 catalyst. (G) Aberration-corrected HAADF-STEM image of the catalyst. (H) UV-Vis DRS of UiO-66, d-UiO-66, and Ru_1/d-UiO-66. (I) NH_3 yield comparison for UiO-66, d-UiO-66, and Ru_1/d-UiO-66 catalysts, and control experiments conducted in the absence of light, N_2, and water. Reproduced with permission from ref. 140. Copyright 2023, Wiley-VCH. (J) Schematic representation of the Ru single-atom-bonded TiO_2, Ru_1/TiO_2-V_O, prepared by the molten salt method. (K) HADDF-STEM image of Ru_1/TiO_2-V_O, where the Ru single atoms are marked by white circles. (L) UV-Vis DRS of TiO_2, TiO_2-V_O, and Ru_1/TiO_2-V_O. (M) NH_3 yield comparison for TiO_2, TiO_2-V_O, and Ru_1/TiO_2-V_O, and control experiments conducted in the absence of light, N_2, catalysts, and water. Reproduced with permission from ref. 182. Copyright 2023, Elsevier.

5036 | *Chem. Soc. Rev.*, 2025, **54**, 5021–5080

This journal is © The Royal Society of Chemistry 2025

atoms. However, efforts to prepare a cost-effective, metal-free SA, like a boron-based SA photocatalyst are underway.[183] Theoretical studies on single-atom B on graphitic carbon nitride support demonstrate that it can efficiently reduce dinitrogen to selectively produce ammonia-suppressing competitive HER *via* the "σ donation–π* back-donation" properties of the designed catalyst. The activation barrier and overpotential of dinitrogen reduction are notably less for this metal-free SA catalyst when compared with most existing metallic catalysts.

4.2. 1D photocatalysts and heterostructures

1D materials, being microscale along one dimension, provide more surface area and easily accessible catalytic active sites than 0D materials, which enhances their catalytic performance. Various 1D carbonaceous materials have been investigated over the past few years because of their stability, good conductivity, and tuneable electronic structure, which exhibit remarkable catalytic activity.[184] The porous structure of the carbonaceous materials also facilitates the adsorption of N-containing species, which enhances the catalytic reaction rate. The onset potential for HER is comparatively more on carbon-based catalysts, which is beneficial for N_2RR and NO_xRR. The introduction of heteroatoms like B, N, and S, which have different electronegativity than C, results in charge distribution in the

structure and induces more active sites in the material for the adsorption of reactants. Graphitic carbon nitrides, g-C_3N_4, generally form layered two-dimensional structures that can transfer electrons in two dimensions. However, orderly 1D nanostructures of g-C_3N_4 can constrain charge transfer in one dimension, thus reducing the charge recombination. The introduction of defects, *i.e.*, metal dopant K and –C≡N, into the g-C_3N_4 nanorods further enhances their catalytic activities (Fig. 8A–D).[107] From theoretical studies, it has been observed that the active site is –C≡N, which donates electrons while K centres trap electrons. The synergistic effect of dual defects also promotes light absorption, charge separation, and proton adsorption, and enhances the photocatalytic N_2RR. Carbon-coated hydroxyapatite (Hap-C) nanorod, another carbon-based material derived from bones, exhibits considerable photoluminescence under ultraviolet light.[142] Hydrothermal deposition of Ti^{3+}–TiO_2 on the surface of Hap-C promotes the absorption of visible light, increases electron transfer, and reduces agglomeration. Due to these characteristics, the Ti^{3+}-TiO_2/HAp-C nanorods can accelerate photocatalytic N_2/H_2O ammonia synthesis compared to pristine Ti^{3+}-TiO_2 and HAp-C nanorods separately.

Oxygen vacancies, the most frequently formed defect, can act as active sites for the adsorption and activation of precursor
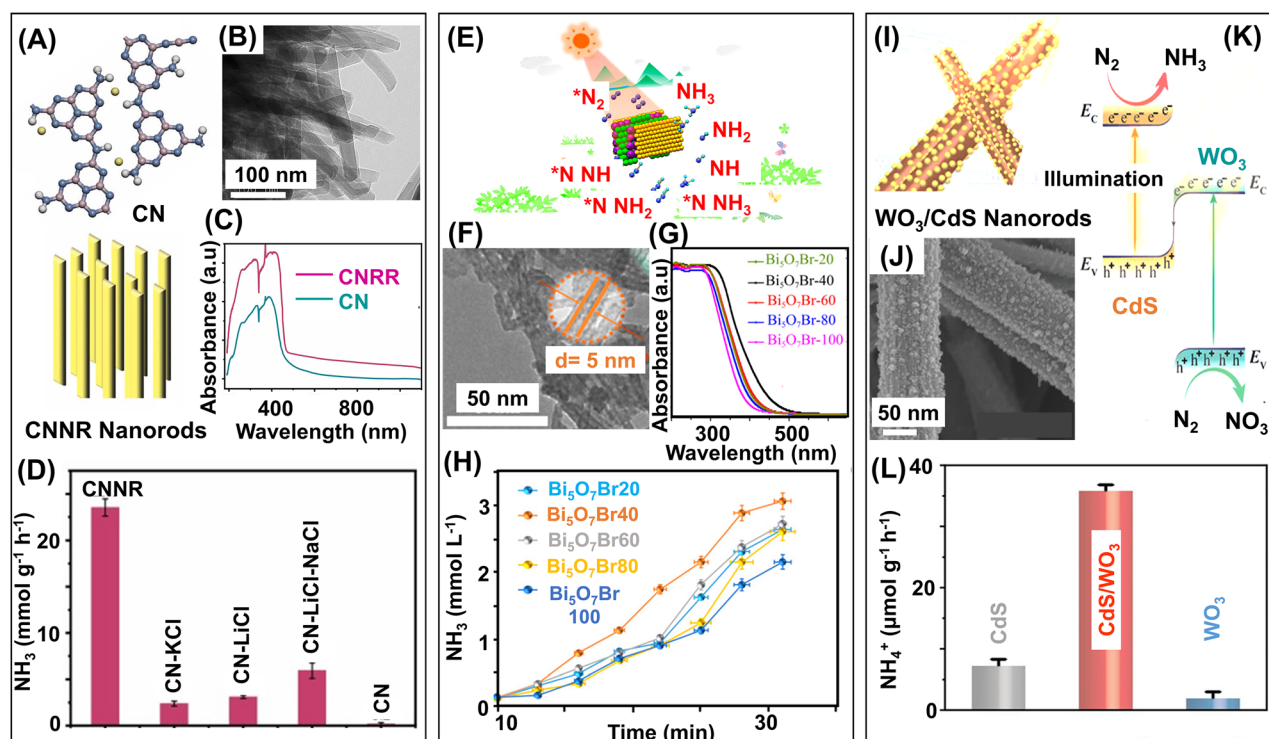

Fig. 8 One-dimensional (1D) photocatalysts for ammonia synthesis. (A) Schematic representation of the structure of graphitic carbon nitride (CN) and graphitic carbon nitride nanorods (CNNR). (B) TEM image of CNRR. (C) UV-Vis DRS of CN and CNRR. (D) NH_3 yield comparison for different carbon nitride photocatalysts. Reproduced with permission from ref. 107. Copyright 2022, Elsevier. (E) Schematic representation of NH_3 synthesis by Bi_5O_7Br nanotubes. (F) TEM image of Bi_5O_7Br-40 nanotubes prepared at 40 °C. (G) UV-Vis DRS of different Bi_5O_7Br prepared at various temperatures. (H) Comparison of NH_3 evolved by using different Bi_5O_7Br catalysts prepared at various temperatures. Reproduced with permission from ref. 144. Copyright 2020, American Chemical Society. (I) Schematic representation of the CdS-decorated WO_3 nanorods, forming a heterojunction. (J) FE-SEM image of WO_3/CdS nanorods. (K) Schematic representation of the electron transfer process at the WO_3/CdS heterojunction for photocatalytic "overall N_2 fixation". (L) NH_3 yield comparison between CdS, WO_3, and WO_3/CdS catalysts. Reproduced with permission from ref. 159. Copyright 2022, Wiley-VCH.

This journal is © The Royal Society of Chemistry 2025

Chem. Soc. Rev., 2025, **54**, 5021–5080 | **5037**

molecules, and can also alter the optical and electronic properties of photocatalysts. In the case of photocatalysts like Bi_5O_7Br nanotubes with oxygen vacancies (V_O), the adsorption of N_2 can elongate the $N\equiv N$ bond and form $V_O-N\equiv N$, which consequently helps in the activation of N_2 (Fig. 8E–H).[144] The concentration of V_O has to be optimum because a too high amount of V_O can entrap the charge carriers to such an extent that it may reduce the rate of photocatalysis. Asymmetric defects induced by V_Os can also enhance the segregation of photogenerated electron–hole pairs through charge redistribution and thereby enhance photocatalytic N_2 reduction reactions. One such example of asymmetric defects is demonstrated by the MoO_{3-x} nanometric wires fabricated by the hydrothermal process using glycine for inducing defects.[143] Mo-based catalysts are quite popular N_2 fixation catalysts as the unoccupied d-orbitals of Mo present a strong affinity towards N_2. The defects infused by the V_Os in the structure of MoO_{3-x} result in charge redistribution and promote N_2 adsorption and activation.

Heterojunction engineering and heteroatom doping are two more approaches besides defects engineering to enhance photocatalytic ammonia synthesis. One such example of a catalyst that has been fabricated using all three approaches is Cu ion-doped $W_{18}O_{49}$ ultrathin nanowires ($Cu-W_{18}O_{49}$-x UTNW).[150] In situ reduction of the $Cu-W_{18}O_{49}$-x UTNW with ascorbic acid as an antioxidant and $NaBH_4$ as a reducing agent form $Cu_2O-W_{18}O_{49}$-x UTNM, the actual photocatalyst for N_2 reduction. This catalyst is adorned with oxygen vacancies (V_O) which promote N_2 adsorption and activation, and facilitate $N\equiv N$ bond dissociation. The in situ-generated Cu_2O forms an S-scheme heterojunction with $W_{18}O_{49}$-x UTNW, which modifies the internal electric field and enhances the separation and transfer of the photogenerated carriers. All these strategies developed for fabricating the nanowires result in efficient photofixation of N_2 to form NH_3. The formation of a heterojunction between two materials induces a strong electronic coupling that promotes interfacial charge transfer and, at the same time, inhibits the recombination of electron–hole pairs. One such recent work reported the construction of a heterojunction between two redox semiconductors, CdS nanoparticles and WO_3 nanorods, forming a 0D–1D-type heterostructure (Fig. 8I–L).[159] The reductive-type CdS has a negative conduction band (CB) position and the electrons in CB_{CdS} have a strong reduction ability. The oxidative component WO_3 has a higher positive valence band (VB) position and the holes in VB_{WO3} have a strong oxidation ability. The heterojunction builds an interface and an electric field between CdS and WO_3 components. Upon photoexcitation, this built-in electric field promotes the separation of electrons and holes, and migrates them via interfacial charge transfer to CdS and WO_3, respectively. These electrons with strong photoreducing ability can efficiently convert N_2 to NH_3, and the holes can simultaneously oxidize N_2 to NO_3^- under mild conditions, thereby completing the "overall nitrogen fixation" reactions. Another example of such heterojunction formation is $Bi/Bi_2Sn_2O_7$ nanocomposites where etching of oxygen vacancies (V_O) in the Bi–O bonds

present in $Bi_2Sn_2O_7$ pyrochlore is utilized for the in situ preparation of metallic Bi.[160] The Schottky junctions formed at the interface of metallic Bi and semiconducting $Bi_2Sn_2O_7$ lead to the separation of photogenerated charge carriers. Moreover, the contact between the semiconducting $Bi_2Sn_2O_7$ and metallic Bi facilitates directional electron transfer from $Bi_2Sn_2O_7$ to Bi, enriching the concentration of photogenerated electrons at the active sites of metallic Bi. These electrons can effectively reduce N_2 to form NH_3. These results highlight the significance of engineering one-dimensional heterostructured catalysts for photocatalytic production of ammonia.

4.3. 2D photocatalysts and heterostructures

Due to their light-harvesting properties, semiconductors play a major role in the photocatalytic synthesis of ammonia. When a semiconductor absorbs a photon with energy equal to or greater than its band gap, electrons are excited from the valence band to the conduction band, creating holes in the valence band. These electrons and holes can migrate to the surface of the semiconductor and initiate the corresponding reduction and oxidation reactions. But sometimes, the photogenerated electrons and holes can recombine either on the surface or in bulk, which in turn hampers the photocatalytic redox reactions. The recombination of charge carriers can be slowed down by introducing defects in the lattice or by forming heterostructures with other low-dimensional materials. TiO_2, ZnO, CdS, and CdSe are some common semiconductors, but the most widely used semiconductor in photocatalysis is TiO_2. TiO_2 is cheap, stable, non-toxic, and has band positions aligned to allow water oxidation and reduction reactions to occur simultaneously.[185] The semiconductors can be 0D, 1D, or 2D. Among these, 2D semiconductor nanosheets have more surface area and active sites, offering better chances of doping and making them potentially more active than 0D or 1D structures. In TiO_2, the most widely explored semiconductor photocatalyst, the oxygen vacancies (V_O) have a potential role in regulating its photocatalytic properties. Rutile $TiO_2(110)$ structure is composed of alternating rows of Ti^{4+} and bridging O (O_b) atoms.[70] These O_b atoms form the vacant sites and the two excess electrons are transferred to each of the 3d orbitals of the two neighbouring Ti^{4+}, which reduces Ti^{4+} to Ti^{3+}. The position of the donor level of Ti^{3+} lies below the conduction band of TiO_2. This donor level traps electrons from the conduction band and reduces N_2 to NH_3, confirming Ti^{3+} to be the active site for photocatalysis. Hirakawa and co-workers have identified the active sites of TiO_2 for the reduction of NO_3^- to N_2 and NH_3, respectively.[186] They deduced that the Lewis acid sites (Ti^{4+}) of TiO_2 can perform non-selective reduction of NO_3^- to N_2 and NH_3. The surface defects formed by oxygen vacancies (V_Os) can donate electrons to Ti^{4+} and reduce them to Ti^{3+}, and these Ti^{3+} sites can selectively reduce NO_3^- to NH_3. So, by maintaining the ratio of surface defects and Lewis acid sites, a higher selectivity of NH_3 (97%) can be achieved. The high energy level of LUMO π^* makes the donation of electrons to π^* orbitals more energy-demanding. The rate-limiting step is the reduction of NO_3^- to NO_2^-. Liberation of this NO_2^- intermediate from

5038 | Chem. Soc. Rev., 2025, **54**, 5021–5080

This journal is © The Royal Society of Chemistry 2025

Lewis acid sites of TiO_2 is mainly responsible for N_2 generation. The surface defects of TiO_2 can entrap intermediates like NO_2^- and NO and suppress the formation of N_2. Heteroatom doping is another effective strategy for increasing active sites for adsorption and activation of N_2. In a typical case, anatase TiO_2 doped with B proves to be an excellent visible-light-driven catalyst for ammonia synthesis with a band gap of 1.92 eV and a thermodynamic barrier of 0.44 eV.[145] The B non-metal doping narrows the band gap of TiO_2 and makes it photoactive in the visible region. The advantages of using B as a dopant are manifold: (i) B forms interband states near the conduction band of TiO_2 and reduces the recombination of charge carriers; (ii) the hybrid orbitals of B can form π-back bonding with N to activate N_2; (iii) B atoms prohibit binding with H^+ and thereby suppress the competing HER; and (iv) B atoms, along with the transition metal, act as active sites for N_2 reduction. In another work, C-doping by bottom-up approach from Ti_3SiC_2 MAX precursor forms two-dimensional C-doped TiO_x nanosheets (Fig. 9A–D).[71] These $C-TiO_x$ nanosheets show enhanced photocatalytic activity under visible light irradiation. C-doping increases the number of Ti^{3+} centres in the catalyst,

induces photoactivity in visible light, and breaks N≡N, which is the rate-limiting step. Ti^{3+} centres act as the active sites and the two adjacent Ti^{3+} centres chemisorb and activate N_2 molecules. The optimal ratio of Ti^{3+}/Ti^{4+} in this TiO_x nanosheet is maintained at 72.1% and, with the addition of Ru/RuO_2 co-catalyst, charge recombination is reduced. Apart from TiO_2, tungsten oxide semiconductors are also well-known photocatalysts. Oxygen vacancy (V_O)-rich $W_{18}O_{49}$ semiconductors with sea-urchin morphology, after low-content Ru modification by $NaBH_4$ reduction get transformed into rough 2D sheets.[161] This sheet-like morphology exposes more active sites and facilitates the adsorption of N_2 molecules. The V_OS enhance the interfacial hydrogen spillover process, thus H^* generated from water as the proton source is utilized in the hydrogenation of N_2 to NH_3. Ru captures electrons from $W_{18}O_{49}$ and acts as the active site for H_2O dissociation. The V_OS play multiple roles, such as facilitating H^* migration from Ru for efficient hydrogen spillover, promoting the adsorption of N_2, acting as active sites for hydrogenation reaction, and lowering the overall energy barrier for NH_3 photosynthesis reaction. Plasmonic semiconductors also act as effective photocatalysts for ammonia production.
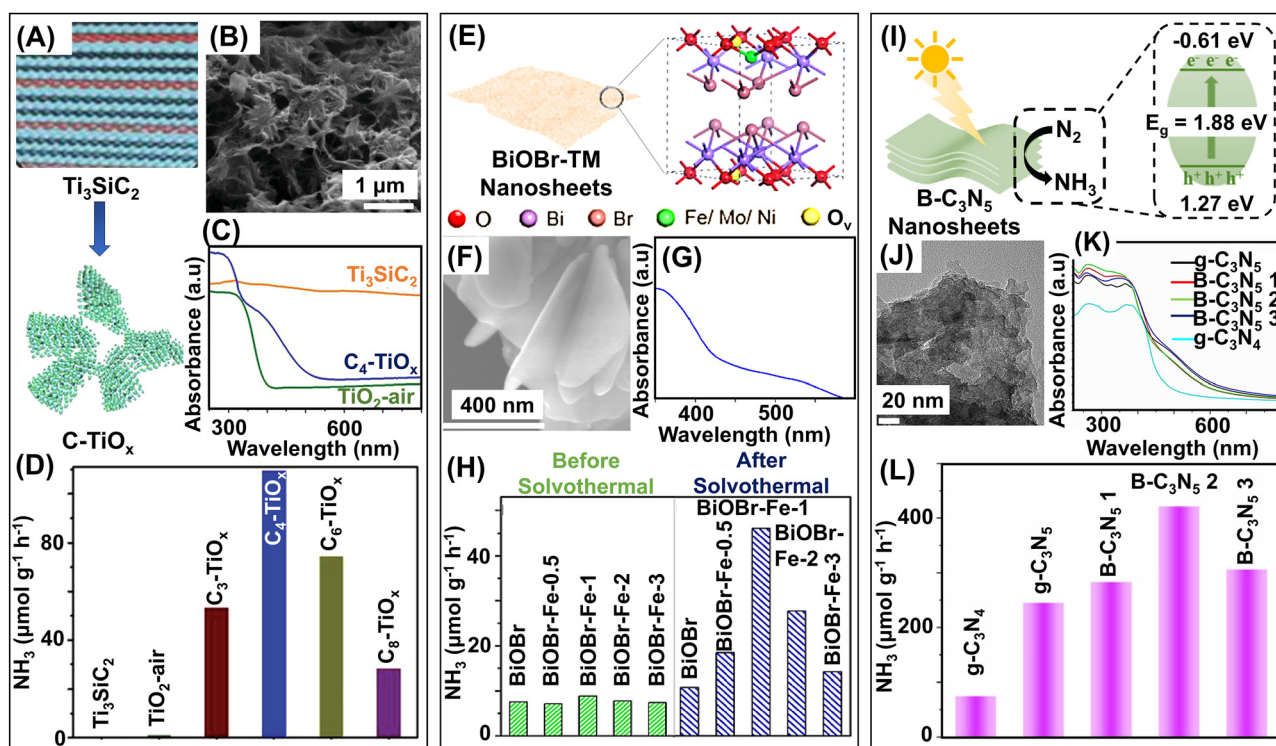

Fig. 9 Two-dimensional (2D) photocatalysts for ammonia synthesis. (A) Schematic representation of the preparation of 2D $C-TiO_x$ nanosheets by thermal oxidation etching at 200 °C. (B) SEM image of C_4-TiO_x obtained after four hours of thermal oxidation etching. (C) UV-visible absorption spectra of Ti_3SiC_2, TiO_2–air, and C_4-TiO_x. (D) NH_3 yield comparison between Ti_3SiC_2, TiO_2–air, and $C-TiO_x$ catalysts obtained after varying durations of thermal etching. Reproduced with permission from ref. 71. Copyright 2021, Wiley-VCH. (E) Schematic representation of the transition metal (TM)-doped BiOBr nanosheets where TM is Fe, Mo, or Ni, obtained by solvothermal reactions. The structure in the dotted box represents the crystal lattice of the TM-doped BiOBr. The best performance is observed for TM = Fe. (F) SEM image of BiOBr-Fe-S-1 catalyst obtained by Fe doping in BiOBr in 1 molar ratio and after solvothermal reaction. (G) The light absorption spectrum of BiOBr-Fe-S-1. (H) NH_3 yield comparison between pristine BiOBr and doped BiOBr before and after solvothermal reactions for different molar ratios of Fe doping. Reproduced with permission from ref. 73. Copyright 2021, Elsevier. (I) Schematic representation of photocatalytic N_2 reduction to NH_3 by B-doped C_3N_5 nanosheets. (J) TEM image of $B-C_3N_5$. (K) UV-Vis DRS of and (L) NH_3 yields by $g-C_3N_4$, $g-C_3N_5$, and $B-C_3N_5x$ photocatalysts (x is the mass percentage of ammoniumborate to 3-amino-1,2,4-triazole). Reproduced with permission from ref. 147. Copyright 2022, Elsevier.

The localized surface plasmon resonance (LSPR) promotes photoconversion of N_2 and the surface oxygen vacancies (V_O) present in these catalysts adsorb and activate the N_2 molecules. However, the V_Os can sometimes get oxidized by the photo-generated holes which might diminish the LSPR properties of the catalyst upon heat treatment. To solve this problem, in one of the recent works, plasmonic MoO_{3-x} nanosheets with Sb doping have been developed.[162] Though Sb doping does not effectively increase the concentration of V_O, the low oxidation state of Sb can help stabilize the LSPR effect of the plasmonic MoO_{3-x}. The uncoupled electrons present in the d orbitals of low-valent Sb help maintain the LSPR in the NIR region, thus producing NH_3 from photocatalytic N_2 fixation. Bismuth-based semiconductors like bismuth oxyhalides and bismuth-based binary metal oxides are effective photocatalysts in the visible light range and have high chemical stability. However, their weak interactions with N_2 limit their use as catalysts. This drawback can be overcome with heteroatom doping, vacancy formation, formation of heterostructures, or modification of exposed crystal facets. Chen and co-workers modified BiOBr nanosheets with transition metals like Ni, Fe, and Mo by hydrothermal method and introduced oxygen vacancies (V_Os) *via* the solvothermal method (Fig. 9E–H).[73] The transition metals and V_Os tune the band gap of BiOBr and enhance electron transfer to the anti-bonding orbital of N_2, thereby triggering adsorption and activation of N_2. The simultaneous presence of V_Os and transition metals alters the band positions, diminishing the recombination of charge carriers. The modified BiOBr enhances the photoreduction of N_2 by six times compared to normal BiOBr, forming 46.1 μmol g^{-1} h^{-1} of NH_3. Using cocatalysts is another intriguing technique to increase the efficiency of photocatalytic ammonia synthesis. Cocatalysts are generally photocatalytic metallic particles or semiconductors and are used to promote electron transfer processes, inhibit the recombination of charge carriers, and switch to a preferable range of incident light for photocatalysis. In a typical BiOBr semiconductor photocatalyst, the efficacy of solar light-powered N_2RR is enhanced 65 times by using Bi nanoparticles as a cocatalyst.[146] Bi NPs lower the rate of competing HER and construct a Schottky junction at the Bi/BiOBr interface, which facilitates the interfacial transfer of electrons. The unidirectional transfer of electrons toward the Bi active sites accelerates the solar light N_2 conversion efficiency to ammonia. Instead of converting highly pure, air-separated, and expensive N_2, aerobic N_2 reduction of air (N_2/O_2) can be used to produce NH_3 cost-effectively. The addition of water oxidation cocatalysts like CoOOH with BiOCl nanosheets can also enhance photocatalytic NH_3 formation.[44] The cocatalyst facilitates the OER half-reaction and, consequently, boosts the N_2RR to NH_3. Solvother-mally prepared trace Bi^0-loaded Bi_2MO_6 (M = W, Mo) can prepare ammonia *via* aerobic photocatalytic reduction of N_2.[187] The role of a trace amount of Bi^0 is crucial in this reaction. The formation of excess Bi^0 is inhibited by the presence of O_2 in the reaction medium. The polarization dipole field produced by Bi^0 favours an effective separation of photogenerated charge carriers and promotes ammonia synthesis

from the photocatalytic reduction of N_2. Though the process is an inexpensive route for ammonia production, it has limitations because the O_2 present in the reaction medium might react with photogenerated e$^-$s and h$^+$s to create reactive oxygen species like $O_2^{\bullet-}$, $^{\bullet}OH$, which can oxidize the synthesized ammonia or react with the catalyst itself. Therefore, the aerobic reduction of N_2 needs further optimization before it can be effectively used for ammonia synthesis. The problems of aerobic reduction and the expensive nature of pure N_2 can be circumvented by using nitrates as the N-source, often present in wastewater systems. In one of the recent works by our group, a BiOI-based "AmmoGen" microrobot has been prepared for the photocatalytic synthesis of NH_3 from NO_3^- upon visible light irradiation.[188] The efficiency of the conventional photo/chemical synthetic techniques for ammonia production is limited by intensive mass-transfer processes. To address this challenge, our group has envisioned a novel technology for ammonia generation, where the photocatalytic BiOI particles are hybridized with magnetic Fe_3O_4 nanoparticles to fabricate an "AmmoGen" microrobot, that can photoreduce nitrate to ammonia using renewable light energy sources. Experiments with "static" particles and "dynamic" microrobots demonstrate that the magnetic propulsion of the "AmmoGen" microrobots significantly improves the mass transfer process, and enhances the photocatalytic ammonia production. This work on microrobots, in principle, can help improve photocatalytic reactions and be utilized in the future for value-added small molecule synthesis. Piezoelectric materials like Bi_3TiNbO_9[189] and $BaTiO_3@C$[190] have also emerged recently as efficient photocatalysts for CO_2 reduction and organic pollutants degradation. In piezoelectric materials, a polarization-induced electric field is formed by the displacement of the positive and negative charge centres onto opposite sides and the resultant internal electric field (IEF) reduces the recombination of photogenerated electron–hole pairs, enhancing the photocatalytic activity of these materials. Layered bismuth-based piezoelectric $SrBi_4Ti_4O_{15}$ nanosheets with oxygen vacancies (V_O), formed by low-temperature hydrothermal treatment with glyoxal can effectively photoreduce N_2 to produce NH_3.[191] These nanosheets manifest self-polarization, originating from the $[TiO_6]$ octahedral distortion, with the polarization direction parallel to the $[Bi_2O_2]^{2+}$ layer. This polarization field and V_O synergistically promote N_2 adsorption, activation, and reduction to NH_3 *via* three electron-transfer pathways. TiO_2-decorated layered silicate magadiite piezo-photocatalytic nanosheets also exhibit significant enhancement in NH_3 production compared to TiO_2 or silicate magadiite separately.[192] The TiO_2 nanoparticles deposited on silicate magadiite enhance the piezoelectric potential and the polarization-induced internal electric field increases the lifetime of the photogenerated charge carriers in these nanosheets, and the synergistic piezo and photo activities of the catalysts enhance the photocatalytic production of NH_3 from N_2 reduction.

Another commonly used photocatalytic 2D material is graphitic carbon nitride (g-C_3N_4). It consists of tri-s-triazine rings interconnected *via* tertiary amines, which makes it thermally

5040 | *Chem. Soc. Rev.*, 2025, **54**, 5021–5080

This journal is © The Royal Society of Chemistry 2025

and chemically stable.[126] The electronic structure of g-C_3N_4 makes it a prospective photocatalyst as it can absorb solar light due to its small band gap, unlike graphene. The structure of g-C_3N_4 bears a close resemblance to graphite due to π conjugation and the two-dimensional structures. Heteroatom doping can modify the electronic properties of g-C_3N_4 and the vacant active sites can increase the efficiency of the catalytic reactions. For instance, Wang and co-workers prepared B-doped porous g-C_3N_4 nanosheets by thermal treatment.[77] The B-dopant induces a small-scale p–n type heterojunction, which promotes efficient charge separation in the catalyst. B doping changes the electronic structure by inducing localized electron states in the band gap and promotes strong tail absorption in the visible light region. Also, doping passivates the active N atoms of g-C_3N_4, ensuring that the NH_3 produced does not originate from the exposed N atoms. The B atoms act as active sites for the adsorption and activation of N_2 and exhibit good photo-catalytic activity with 313.9 μmol g^{-1} h^{-1} yield rate of NH_3. Incorporating N-vacancies (V_N) and adding cocatalysts can also improve the photocatalytic performance of g-C_3N_4 as exhibited by the Ni_3B/V_N-g-C_3N_4 catalyst.[163] The introduction of V_N enhances visible light absorption and electrical conductivity properties of g-C_3N_4. Noble metal-free cocatalyst Ni_3B nanoparticles act as active sites for the adsorption and activation of N_2. The Schottky junctions formed between Ni_3B and V_N-CN also facilitate the separation of photogenerated charge carriers and migration of electrons for photoreduction of N_2. Introducing one more N atom to g-C_3N_4 forms g-C_3N_5, a two-dimensional material with more π conjugation, which promotes superior charge separation, narrower band gap, and better solar absorption when compared to g-C_3N_4. Li et al. reported a B-doped g-C_3N_5 synthesized by a one-step thermal polymerization technique (Fig. 9I–L).[147] The five azole rings of g-C_3N_5 facilitate electron transfer and decrease the adsorption energy of N_2. B-doping increases the photocatalytic efficiency of g-C_3N_5 like in the previous case (B-doped g-C_3N_4) with B as the active site for photocatalysis and NH_3 yield of 421.18 μmol g^{-1} h^{-1}, which is 1.72 times that of g-C_3N_5.

Graphdiyne (GDY) is another emergent 2D carbon material, comprising sp and sp^2 hybrid states endowed with unique properties like highly conjugated and super-large π structures, infinite number of pores, natural band gap, a hole-transport layer, high charge carrier mobility, electronic conductivity, and stability, which make them excellent photocatalysts.[193] Recent studies indicate that GDY can form heterojunctions with different low-dimensional materials to design excellent catalysts for ammonia photosynthesis. Fe site-specific magnetite when incorporated with GDY, the GDY modulates the coordination environment of magnetite to form two selective valence states, namely, tetrahedrally coordinated Fe and octahedrally coordinated Fe.[148] The coordination environment and valence charge transition regulate the photocatalytic properties of Fe_3O_4 and significantly enhance the photocatalytic nitrogen reduction to ammonia. Graphdiyne is also capable of modulating the surface plasmon resonance of quantum dots (QDs), which is evident from the heterojunction-based GDY-CoO_x QDs

catalysts.[164] The natural porous structure, the acetylenic bonds, and the high reduction ability of the GDY incorporate the CoO_x QDs and the combined effects of enhanced surface plasmon resonance and modification of valence states of the metal atom enhance the photocatalytic nitrogen fixation reaction to produce ammonia.

4.4. Organic framework-based photocatalysts and heterostructures

Organic framework-based photocatalysts, viz., porous–organic frameworks (POFs), comprising covalent–organic frameworks (COFs), porous–aromatic frameworks (PAFs), covalent–triazine frameworks (CTFs), and metal–organic frameworks (MOFs), are emergent catalysts for photocatalysis owing to their unique physical and optoelectronic properties such as tuneable light absorption, large specific surface area, periodic arrangement of building blocks, precisely controlled pore size, and easy functional modifications. These properties make these materials unique for applications like catalysis, gas absorption and storage, and sensing. Different morphologies varying from 2D to 3D can be designed by tuning the structure and assembly of covalent bonds. This section will describe a few examples of such organic frameworks and their advantages in photocatalytic ammonia generation. Metal phthalocyanine-derived POFs (MPc-POFs (M = Fe, Co, Ni, Cu, Zn)) consist of conjugated planar π-electron organic macrocycles and their optical and electronic properties can be controlled for optimizing photocatalytic N_2RR.[165] Most photocatalytic N_2RR systems proceed via gas-in-solvent (GIS) systems where gaseous N_2 is purged in water. However, these systems are limited by certain disadvantages like low solubility of N_2 in water, sluggish N_2 transfer at the interface, and interaction of water with the catalyst. In an attempt to promote N_2 transfer and utilization at the active sites of the catalyst, these POFs use a solvent-in-gas (SIG) system as the reaction medium, where MPc-POFs perform the catalysis in direct N_2 gas, and the hydrogenation step is performed in suspended proton source provided as the dispersed phase. Herein, the active sites of the MPc-POFs have access to abundant N_2 molecules and can produce ammonia at an ultrafast rate of 1820.7 μmol g^{-1} h^{-1}, which is approximately eight times higher than that obtained from conventional GIS (226.2 μmol g^{-1} h^{-1}).

2D COFs are porous polymers where any photoactive species can be incorporated into the ordered pores of their frameworks such that they can function as catalysts for different photocatalytic reactions.[194,195] The organic units in the 2D π lattices of COF semiconductors can facilitate the separation and transport of photogenerated charge carriers.[194] The one-dimensional polygon channels in the porous COFs also help in mass transport. Single-atoms like Au can be easily anchored into porphyrin-based COFs (COFX-Au, X = 1–5) for photocatalytic NH_3 synthesis (Fig. 10A–D).[166] The performance of the photocatalytic NH_3 synthesis can be controlled by tuning the microenvironment of the single-atom Au catalytic centre resulting from the position of different functional groups at the proximal and distal positions of porphyrin units. In the first case, a
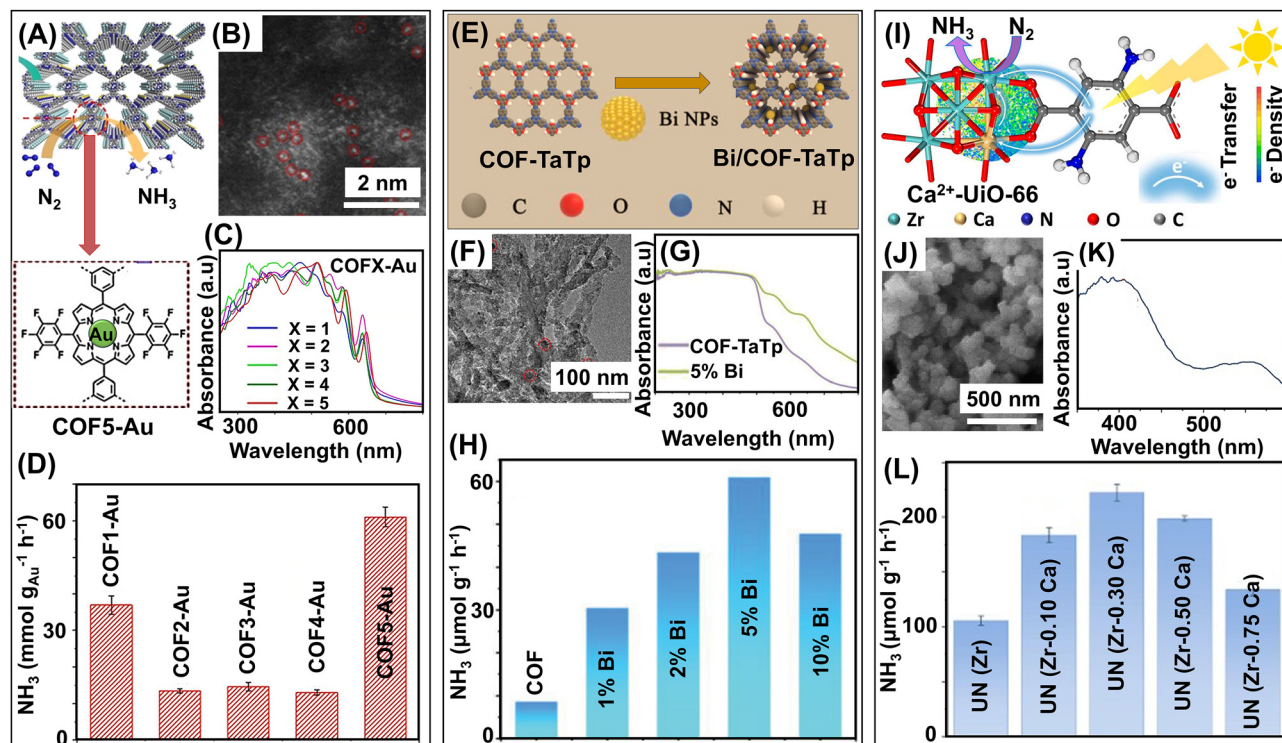
This journal is © The Royal Society of Chemistry 2025

Chem. Soc. Rev., 2025, **54**, 5021–5080 | **5041**

Fig. 10 Organic framework-based photocatalysts for ammonia synthesis. (A) Schematic representation of nitrogen reduction to ammonia by the porphyrin-based covalent organic framework anchoring Au single-atoms (COF5-Au). The structure in the dotted box represents the microenvironment of the Au catalytic centre. (B) Aberration-corrected HAADF-STEM image of COF1-Au, where Au single-atoms are marked by red circles. (C) UV-Vis diffuse reflectance spectra of COFX-Au, where X = 1–5. (D) NH_3 yield comparison of COFX-Au catalysts. Reproduced with permission from ref. 166. Copyright 2023, American Chemical Society. (E) Schematic representation of the fabrication of Bi NP-decorated imine linked COF-TaTp (Bi/COF-TaTp). (F) TEM image of 5% Bi/COF-TaTp, (G) UV-Vis diffuse reflectance spectra of COF-TaTp, and 5% Bi/COF-TaTp. (H) NH_3 yield comparison between pristine COF and different percentages of Bi NPs. Reproduced with permission from ref. 168. Copyright 2022, Wiley-VCH. (I) Schematic representation of photocatalytic N_2 reduction to NH_3 by Ca^{2+}-doped UiO-66. (J) SEM image of UN(Zr-0.30Ca)-4. (K) Light absorption spectrum of UN(Zr-0.30Ca)-4. (L) NH_3 yield comparisons between UN(Zr), UN(Zr-0.10Ca), UN(Zr-0.30Ca), UN(Zr-0.50Ca), and UN(Zr-0.75Ca) were obtained by feeding $ZrCl_4$ and $CaCl_2$ at Ca : (Zr + Ca) ratios of 0.1, 0.3, 0.5, and 0.75. Reproduced with permission from ref. 170. Copyright 2023, Elsevier.

strong electron-withdrawing group is attached in COF1-Au, which yields NH_3 at a rate of 37.0 ± 2.5 mmol g_{Au}^{-1} h^{-1}. This is 171 times more than that of the porphyrin–Au molecular catalyst. The yield is also 2.8 times higher than COF4-Au, where an electron-donating group is used as the functional group. Thus, it can be deduced that the electron-withdrawing groups can facilitate the separation and transportation of photogenerated electrons within the entire COFX-Au framework. Following this deduction, NH_3 production is increased to 61.1 ± 2.7 mmol g_{Au}^{-1} h^{-1} by attaching two strong electron-withdrawing groups to the COF. The performance of photocatalytic N_2RR can also be enhanced by spatial confinement of N_2 near the surface of the COF for better adsorption and activation. This can be achieved by incorporating hydrophilic carboxyl groups (–COOH) into diketopyrrolopyrrole-based COF (DPPCOOH-COF) and forming a localized hydrogen bond network.[167] The –COOH groups promote water to form a layered or porous structure that interacts with the N_2 molecules and localizes them near the active pyrrole units. This leads to enhanced adsorption and activation of N_2 by the DPPCOOH-COF and reduces the energy for photocatalytic NH_3 generation. The photocatalytic activity of COFs is sometimes limited by the fast

recombination of photogenerated charge carriers and the lack of sufficient active sites. Metal active sites can be easily incorporated into the COFs due to their ordered cavities and large specific surface area. Imine-linked 2D COFs have numerous N atoms, which endow the COFs with strong Lewis acidity, and this property of the imine COF-TaTp facilitates the adsorption of N_2, which is a weak Lewis base (Fig. 10E–H).[168] Furthermore, the strong interaction of the Bi metal with the imine nitrogen atom and hydroxyl functionalities of the imine COF facilitates the formation of Bi/COF-TaTp composites through N–Bi–O coordination. The incorporated Bi acts as the active site, which promotes the transfer of charge carriers and activation of N_2 molecules through the donation and back-donation mode. Additionally, the Bi sites inhibit the competitive HER and thus facilitate the photocatalytic NH_3 production from N_2RR.

Metal–organic frameworks (MOFs), another class of organic frameworks composed of metal ions or clusters and organic ligands are also important for photocatalytic applications. Sometimes, the catalytically active metal centres in MOFs are fully coordinated by bridging organic ligands and terminal ligands, and become inaccessible to the reactants. Hence, to address this issue, a defective Fe-based MIL (100) MOF has

5042 | *Chem. Soc. Rev.*, 2025, **54**, 5021–5080

This journal is © The Royal Society of Chemistry 2025

been designed by partial removal of these ligands, such as bridging organic ligands and terminal inorganic ligands (OH^- and H_2O), leading to the formation of defective structures.[169] The dual defects expose the coordinatively unsaturated Fe sites, which act as the catalytic active centres for adsorbing and activating N_2 molecules. The defects also modify the electronic structures, which favours the transfer of d-orbital electrons from Fe sites into the N_2 π^* antibonding orbital to form the key intermediate *NNH in the photocatalytic N_2RR for NH_3 formation. As discussed previously, hydrogen evolution reaction (HER) is a major competitive reaction for photocatalytic N_2RR processes, which limits the production of NH_3. In an attempt to harmonize the competition between HER and N_2RR reactions, a core–shell MOF-based catalyst has been prepared by depositing Ni nanoparticles on the polydopamine shell and NH_2-MIL125 MOF core.[196] Photocatalytic HER occurs at the NH_2-MIL125 MOF core and the evolved H_2 is captured by the Ni nanoparticles and converted into adsorbed *H species. The produced *H is then transferred back to the NH_2-MIL125 core via NiO, which reacts with N_2 and produces NH_3. This "hydrogen state switching" strategy ensures the supply of requisite protons from HER for hydrogenation of N_2 to NH_3 formation, thus "transforming-competition-into-cooperation". Like other photocatalysts, metal atom doping in MOFs can lead to enhanced photoproduction of NH_3. This is manifested in Ca^{2+}-doped UiO-66, a Zr-based MOF, where low electronegative Ca^{2+} increases the electron donation capability of Zr active sites (Fig. 10I–L).[170] Furthermore, the incorporated diamino ligand modifies the band gap of Ca^{2+}-UiO-66 to enhance the light absorption range and separation of charge carriers. All these factors contribute to amplified photoreduction of N_2 to produce NH_3 under the full spectrum of light. The formation of heterojunctions can also enhance the photoactivity of MOFs via inhibition of recombination of charge carriers. An example of such MOF is the heterojunction formation between MXene and MIL-125(Ti) MOF via ligand bridging.[171] A ligand pre-coupling strategy is employed in this work to create the ligand-bridged MXene/MIL-125(Ti), where a coordination bond between the terminal oxygen group of MXene is coupled to the carboxyl group of the ligand in MIL-125(Ti). This ligand bridge forms a one-directional transport channel for electron transfer from MIL-125(Ti) to MXene. This strategy diminishes the interfacial charge transfer resistance and reduces the recombination of photogenerated electron–hole pairs, thus boosting the photocatalytic N_2 fixation to produce NH_3. The design of nanoarchitectonics using S-scheme heterojunction-based MOFs can also facilitate photocatalytic nitrate reduction to ammonia. A nanohouse-like catalyst structure is constructed employing the nanoarchitectonics technology, where NH_2-MIL-125 MOF with a nanoplate-like morphology serves as the floor.[172] Hollow ZIF-8 cages form the surrounding walls and roof of the nanohouse, and $Co(OH)_2$ nanosheets are locked inside this nanohouse and connected to the ground by forming a heterojunction with NH_2-MIL-125 MOF. Each component of this unique sandwich-structured superstructure forming the nanohouse array plays a crucial role in photocatalytic NO_3^-

reduction. The positively charged, hydrophobic, and porous ZIF-8 structure modifies the microenvironment of the NH_2-MIL-125/$Co(OH)_2$ heterojunction by increasing the NO_3^- enrichment, suppressing competitive HER, and promoting NH_4^+ release. The S-scheme heterojunction between NH_2-MIL-125/$Co(OH)_2$ enhances the separation of photogenerated electron–hole pairs and boosts the photo-redox capability of the nanohouse catalyst, promoting NH_3 production from NO_3^-.

5. Low-dimensional electrocatalysts for ammonia synthesis

Electrocatalysts are generally more energy-efficient than photocatalysts because all photons are not effectively utilized in photocatalysis. This inefficiency arises from mismatches between the wavelengths of incident light and the photoactive material's absorption spectrum, as well as from the recombination of photogenerated charge carriers, which reduces the overall efficiency. Electrocatalytic reactions occur under ambient conditions with the external input of electrical energy, which can be easily harnessed from renewable sources like solar, hydro, tidal, or wind energy. The prerequisites for electrocatalysts are: (i) good conductivity; (ii) high surface area and presence of abundant active sites for adsorption of N-containing species; (iii) resistance to corrosion at the working potential range and in the presence of electrolytes; and (iv) long-term stability. The low-dimensional electrocatalytic materials used for ammonia synthesis include transition metal nanoclusters, noble metal-based materials, metal oxides, phosphides, carbides and nitrides, single-atoms, and carbon-based materials. Electrocatalytic materials can be modified by defect engineering, forming heterostructures, or regulating the crystal planes and microenvironment of the catalyst to ensure better electrocatalytic performance. This section will discuss these strategies for designing low-dimensional electrocatalytic materials to synthesize ammonia from N_2 or NO_x sources (Fig. 11 and Table 4).

For the electrocatalytic synthesis of ammonia, the optimal design of an electrocatalytic reactor is pertinent. The electrocatalytic reactor, in principle, consists of the electrocatalytic cell, electrolyte, electrodes, and ion exchange membrane. Electrocatalysts are loaded on the cathode and upon application of a voltage at the electrodes, the electrocatalytic reaction produces ammonia at the cathode by reduction of N_2 or NO_x. Simultaneously, water is oxidized at the anode to generate oxygen. The electrocatalytic cells can be classified as: (i) back-to-back cells; (ii) proton exchange membrane cells; (iii) single-chamber cells; or (iv) H-type cells.[246] A back-to-back cell has two gas diffusion electrodes containing N_2 (cathode) and H_2O (anode), partitioned by cation/anion exchange membranes. The proton exchange membrane cell has a similar configuration except that the anodic component is in aqueous form. Because the electrolyte and the cathode have no direct contact, HER is limited in these kinds of cells. However, the reaction medium consists of gas and solid, which lowers the efficiency
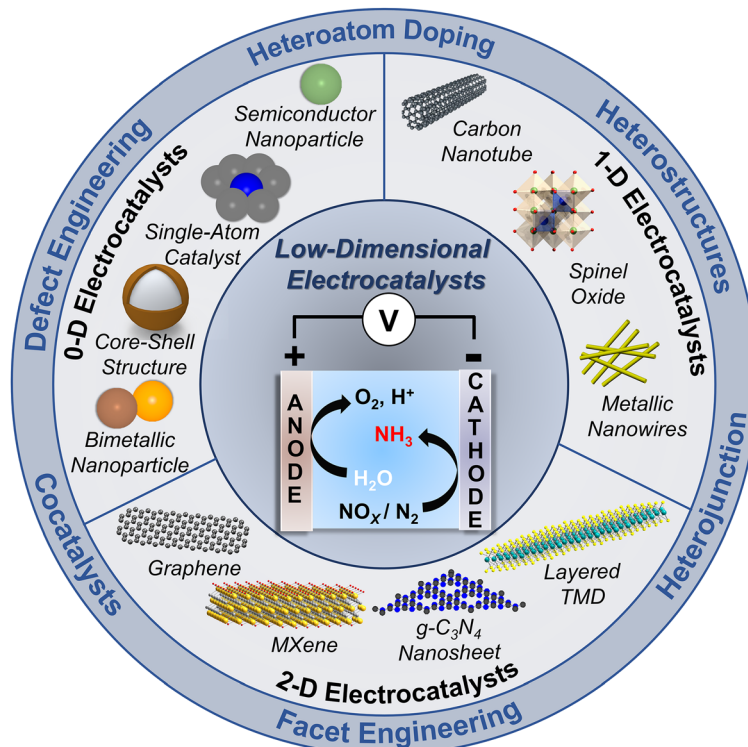
This journal is © The Royal Society of Chemistry 2025

Chem. Soc. Rev., 2025, **54**, 5021–5080 | 5043

Fig. 11 Low-dimensional electrocatalysts for ammonia synthesis. Classification of electrocatalysts into 0D, 1D, and 2D, and schematic representations of few selected electrocatalytic LDMs.

of the catalytic processes. The single-chamber cell, as evident from its name, has cathodic and anodic reactions occurring in the same electrolyte in one chamber. The electrolyte used here is liquid, but the simultaneous presence of the cathode and anode in one chamber can further oxidize the ammonia produced at the cathode. This problem can be overcome by using an H-type cell, the most frequently used electrochemical cell, where the cathodic and anodic compartments are separated by an ion-exchange membrane. The electrolyte is mostly aqueous and, depending on the reaction conditions may be acidic (H_2SO_4 or HCl), neutral (phosphate buffer or Na_2SO_4), or alkaline (KOH).[247] The three-electrode setup is mostly used with a working electrode (*e.g.*, glassy carbon plate, glassy carbon rotating disk, carbon paper, self-supported), reference electrode (*e.g.*, Ag/AgCl), and counter electrode (*e.g.*, Pt, graphite rod).[247] Electrocatalysts are deposited on the working electrodes and proper optimization of the electrocatalysts is pertinent. The most common strategies to improve the efficiency of electrocatalysts for ammonia production include crystal facet engineering, heteroatom doping, and the introduction of vacancies and defects. Taking into account the earlier discussion about the disadvantages of photocatalytic N_2 reduction and the advantages of photocatalytic NO_3^-/NO_2^- reduction, it can be said that they also hold for electrocatalytic reductions.

While devising catalysts for electrocatalytic N_2RR or NO_xRR to NH_3, the main objectives are to ensure good conductivity of the catalysts, availability of adequate active sites for electro-reduction, and restraining the side reactions like HER or

formation of by-products like N_2 and NO by partial reduction of NO_x^-. In the following subsections, we will discuss the design of low-dimensional electrocatalysts and a strategy to overcome the bottlenecks, aiming to enhance both the faradaic efficiency and selectivity of the resulting NH_3. The most commonly used 0D, 1D, and 2D electrocatalysts use simple one-pot synthetic strategies, whereas their heterostructures rely on multi-step synthesis. Synthesis of 0D metallic and metal oxide nanoparticles or nanocrystals uses strategies like seed-mediated growth, galvanic replacement, or reduction methods.[98,197,201,203] Single-atom engineering relies on different thermal modulation techniques like pyrolysis or thermolysis.[102,205] 1D electrocatalysts like monometallic, bimetallic, multimetal alloys, metal oxides, carbon-based nanowires, nanorods, and nanofibers are prepared by chemical/electrochemical reduction, different deposition techniques, electrospinning methods, and thermal reactions.[45,61,106,207,209,213,215] The most commonly used 2D electrocatalysts like graphdiynes, metal, metal oxides, and transition metal dichalcogenides use thermal synthetic strategies like solvothermal, hydrothermal, annealing, or pyrolysis.[222,225,227,228,236] The synthesis of MXenes and MBenes relies on etching, thermal treatments, and the functionalization of terminal groups.[233–235] The electrocatalytic properties of these materials can be enhanced by defect engineering, heteroatom doping, facet engineering, using cocatalysts, formation of heterojunctions, and heterostructures.[197,203,206,225] A more detailed and precise discussion of the different synthetic and modification strategies of ammonia-synthesizing electrocatalysts is presented in Table 4.

5044 | *Chem. Soc. Rev.*, 2025, **54**, 5021–5080

This journal is © The Royal Society of Chemistry 2025

Table 4 Synthetic and modification techniques for selected ammonia-generating low-dimensional electrocatalysts

Classification	Materials	Electrocatalysts	Synthesis/modification	Ref.
0D LDMs and heterostructures	Metallic nanoparticles (NPs) and nanoclusters (NCs)	Pd NCs	Seed-mediated method, facet engineering	197
		Au NPs	Seed-mediated method	198
		Ag NCs	Replacement reaction on Cu foam	199
		Au$_x$–Ni NPs	Donor–acceptor construction, galvanic replacement method	98
		Hollow PdCu NPs	*In situ* reduction and nucleation	200
		Fragmented Bi^0 NPs	*In situ* reduction and fragmentation of Bi-MOF nanorods under applied potentials	201
	Metallic oxides	TiO$_2$@N–C NPs	N-impregnated carbon coating strategy	202
		Cu NPs-V$_O$-TiO$_2$	Defect engineering, chemical reduction	203
	Single-atoms (SAs)	Fe$_1$ SA-NC	Thermal modulation	204
		Fe SA-N/P-C	*In situ* phosphatizing–adsorption–thermolysis process	102
		Cu$_1$ SA-NC/CNT-FEM	Pyrolysis, probe sonication	205
		Cu(I) SA-N$_3$C$_1$	N-doping, wet chemical synthesis, pyrolysis	206
1D LDMs and heterostructures	Metallic nanowires (NWs)	Cu NWs	Chemical reduction	207
		Ru-CuNW	Cation exchange method, thermal annealing, electrochemical prereduction	208
		Rh NCs/SAs-Cu NWs	Electrochemical reduction, galvanic replacement	209
		TA-Au NWs	Surface modification with tannic acid (TA)	210
	Multimetal alloys	Cu$_6$Sn$_5$ alloy	Co-electrodeposition method	61
		IrNi, IrRhNi, and IrFeNi alloys	Chemical Co-reduction, solvothermal method	211
	Metallic oxides	P-TiO$_2$/TP	P-Doping, hydrothermal growth, ion-exchange, phosphating process	212
		a-B$_{2.6}$C@TiO$_2$/Ti	Hydrothermal synthesis, sputter deposition	213
		Fe$_2$TiO$_5$	Defect engineering, electrospinning method	106
	Spinel oxides (AB$_2$O$_4$)	NiCo$_2$O$_4$ NWs/CC	Hydrothermal synthesis, thermal annealing	214
		Mn$_2$–Co$_3$O$_4$ NTs	Hydrothermal synthesis, thermal annealing	215
		C-Co$_3$O$_4$ NTs	C-Doping, "surface locking" mechanism, *in situ* topotactic conversion	216
	Carbon nanotubes (CNTs)/nanofibers	MWCNTs/SWCNTs	Calcination and acid treatment	217
		Ni NPs-N-CNRs	N-doping, electrospinning, carbonization, selective etching with acid	218
		Fe SA-N-carbon nanofibers	N-Doping, C-defects, electrospinning-pyrolysis method	45
2D LDMs and heterostructures	Graphene	Amorphous graphene	Laser irradiation	219
		Amorphous graphene	Transient laser heating	220
		Cu-*cis*-N$_2$O$_2$/graphene	Breaking of coordination symmetry, thermal annealing	221
	Graphdiyne (GDY)	Mo^0-GDY	Solvothermal method	222
		Ru SAs-GDY-graphene	Eglinton coupling reaction, microwave synthesis, impregnation method	223
		Cu SAs-GDY	Impregnation method	224
		Fe$_3$C-GDY	Pyrolysis, interface engineering, heterojunction formation	225
	Carbon nitrides (CN)	B-BCN	Tuning B/N Lewis acid pairs	226
		BCN	Defect engineering, annealing, tuning frustrated Lewis pairs	227
	Metal and metal oxide-based nanosheets (NS)	Ru NS	Hydrothermal method, plasma treatment	228
		hcp-Co NS	Hydrothermal method	229
		CuCo NS	Co-Electrodeposition method	230
		Amorphous RuO$_2$ NS	Defect engineering, molten salt synthesis	231
	MXenes	Ti$_3$C$_2$-V$_O$	Defect engineering, functionalization of terminal group	232
		OH-terminated Ti$_3$C$_2$	Etching, exfoliation, functionalization of terminal group	233
		B-Ti$_3$C$_2$T$_x$	Etching, annealing, B-doping, pyrolysis	234
	MBenes	FeB$_2$	Reflux method	235
	Transition metal dichalcogenides (TMDs)	F-MoS$_2$	Strain engineering, F-doping, hydrothermal method	236
		V-MoS$_2$	Defect engineering, V-doping, hydrothermal method	237
		Metastable 1T''' MoS$_2$	Solid state reaction, thermal annealing, deintercalation of K ions	238
Organic framework-based heterostructures	Metal–organic frameworks (MOFs)	Cu-OUC MOF	Hydrothermal method	239
		Fe$_2$M MOF (M = Fe, Co, Ni, Zn)	Hydrothermal method, Solvothermal method	240

This journal is © The Royal Society of Chemistry 2025

Chem. Soc. Rev., 2025, **54**, 5021–5080 | 5045

Table 4 (continued)

Classification	Materials	Electrocatalysts	Synthesis/modification	Ref.
3D-Printed electrodes based on LDMs	Metallic NPs	NiCoBDC MOF-HsGDY	Interface engineering, dual-template, Glaser-coupling, solvothermal methods	241
		PCN-250-Fe$_3$ MOF	Crystallization, thermal activation	242
		Cu Metallic NPs	Sintering, nanostructuring using electrochemical methods, chemical treatment	243
	Carbonaceous material-based heterostructures	MnO$_x$ coated 0D carbon black, 1D carbon nanotubes	Thermal activation, atomic layer deposition (ALD)	244
		TiO$_2$-coated carbon	Thermal activation, atomic layer deposition (ALD)	245

5.1. 0D electrocatalysts and heterostructures

Among different 0D materials, metallic nanoparticles have been extensively studied for electrocatalysis over the last few decades. The plasmonic character and possibilities of tuning the size, shape, and structure of nanoparticles have made them significant for catalysis. The packing of metal atoms in a particle can be different: tuning the size of nanoparticles exposes different crystallographic facets, which can provide different types of catalytic sites.[248] Several metal nanoparticle-based catalysts have been reported recently; here, we will discuss a few of these and their roles in catalysis. Electrocatalytic denitrification of NO$_x$ for simultaneous removal of N-containing oxides and ammonia production proves quite efficient on metal surfaces, particularly transition metals. Among different transition metals, Cu is the most efficient for electrocatalytic NO$_x$RR.[249,250] Cu produces NH$_3$ selectively as Cu can bind *NO intermediate and by not binding *H, it provides selectivity against competitive HER.[92] Bimetallic nanoparticles are quite common as they offer two different sites for catalysis. Ni–Au nanoparticles can electrochemically reduce N$_2$ to NH$_3$, a reaction facilitated by donor–acceptor couples of Ni and Au (Fig. 12A–D).[98] Donor–acceptor pairs can adsorb and activate N$_2$ and also help the desorption of NH$_3$. Bimetallic PdCu nanocrystals can electrosynthesize ammonia selectively from nitrates (Fig. 12E–H).[200] For synthesis, C$_{12}$N–COOH is employed as the template and dimethyl borane as the reducing agent to form the PdCu hollow nanospheres from Pd- and Cu-containing precursors. The hollow structure of PdCu can trap the intermediates and thus promote the nitrate reduction reaction (NO$_3$RR) with an effective FE of 87.3%. Crystal-phase engineering can effectively improve the performance of N$_2$RR and NO$_x$RR. Nanostructures with controlled facets can exhibit high efficiency for the production of NH$_3$. Several researchers have performed extensive studies to uncover the correlation between ammonia production and crystal facets. For instance, body-centered cubic (BCC) PdCu nanoparticles surpass face-centered cubic (FCC) PdCu nanoparticles in terms of N$_2$RR electrocatalysis due to strong d–d orbital interactions between Pd(4d) and Cu(3d) sites.[47] A comparative study between exposed (100), (111), and (110) facets of Pd reveals that the (100) facet is most active electrocatalytically as it is extremely stable under electrocatalytic reaction conditions, and the energy barrier for desorption of *NH$_3$ to NH$_3$ is lower than for other facets.[197] Pd nanocatalysts show face-dependent reduction capability for NO$_3^-$ as well as NO$_2^-$ in the order of Pd(111) > Pd(100) > Pd(hk0) for NO$_3$RR and Pd(100) > Pd(hk0) > Pd(111) for NO$_2$RR in alkaline conditions.[251] Cuboctahedral Pd with exposed (111) and (100) facets produce the highest quantity of ammonia. Exposure of the two facets makes the cuboctahedra bifunctional, where the (111) facets catalyse the conversion of NO$_3^-$ to NO$_2^-$ and the (100) facets promote the conversion of NO$_2^-$ to NH$_3$. Theoretical calculations on Cu-based surfaces reveal that among Cu(100), Cu(111), and Cu(110), the best electrocatalytic NO$_3$RR performance is exhibited by Cu(111) in neutral and alkaline conditions, and by Cu(100) in strongly acidic conditions.[252] The local coordination

5046 | Chem. Soc. Rev., 2025, **54**, 5021–5080

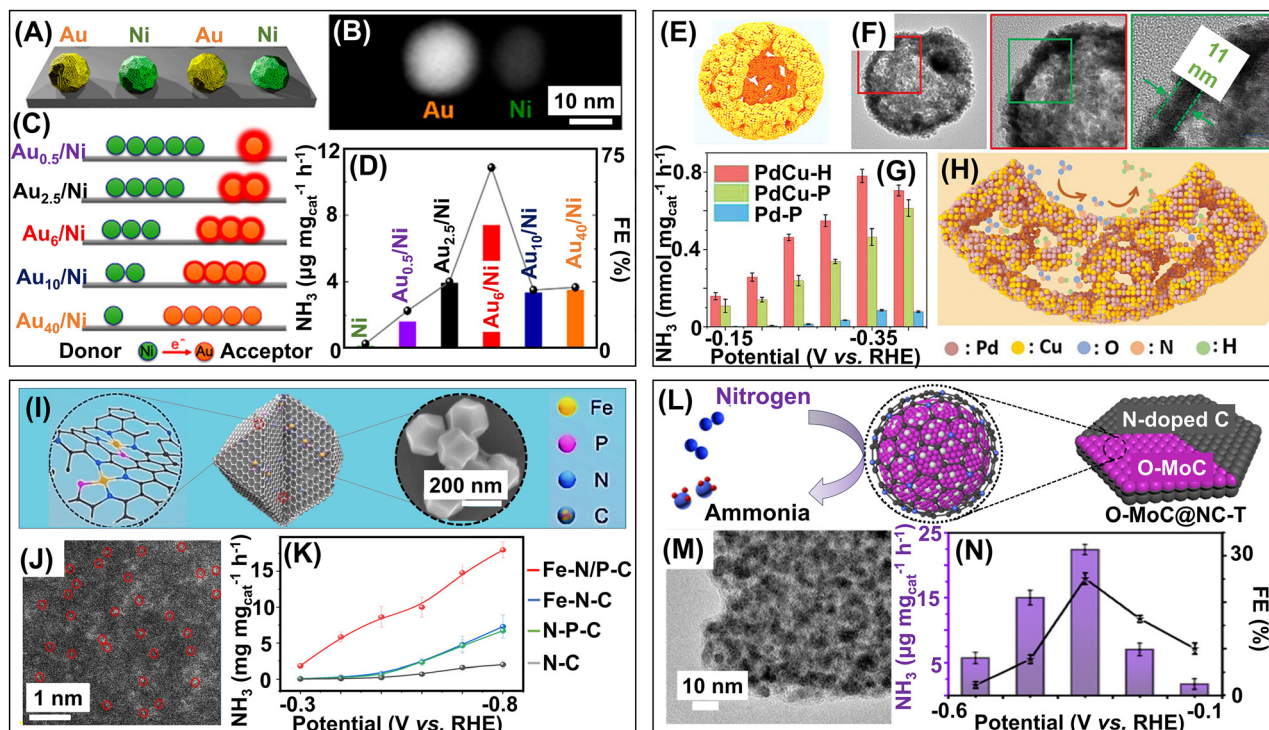This journal is © The Royal Society of Chemistry 2025

Fig. 12 Zero-dimensional (0D) electrocatalysts for ammonia synthesis. (A) Schematic representation of the donor–acceptor couples of Ni and Au nanoparticles. (B) SEM image of Au and Ni nanoparticles. (C) Schematic representation of the electron transfer between donor–acceptor couple Au_x/Ni with different Au loadings. (D) NH_3 yields and Faradaic efficiencies using only Ni and Au_x/Ni nanoparticles donor–acceptor couple catalysts at −0.14 V vs. RHE. Reproduced with permission from ref. 98. Copyright 2019, American Chemical Society. (E) Schematic of the simulated structure of hollow PdCu (PdCu-H) nanoparticle. (F) TEM image of PdCu-H particle at different magnifications and different locations. (G) NH_3 yields using hollow PdCu-H, PdCu-P nanoparticles, and commercial Pd–P. (H) Schematic illustration of NO_3^- reduction over PdCu-H catalyst. Reproduced with permission from ref. 200. Copyright 2023, Wiley-VCH. (I) Schematic representation of the 0D Fe single atom N, P co-modified carbon catalyst (Fe–N/P–C) obtained on pyrolysis from ZIF-8. (J) Aberration-corrected HAADF-STEM of Fe–N/P–C where the Fe single-atoms are marked by red circles. (K) NH_3 yields using N−C (N-modified carbon), N−P−C, Fe−N−C, and Fe−N/P−C catalysts. Reproduced with permission from ref. 102. Copyright 2023, Wiley-VCH. (L) Schematic representation of N_2 electroreduction to NH_3 using oxygen-doped MoC nanoparticles embedded in graphitized carbon shells (O-MoC@NC). (M) TEM image of O-MoC@NC-800 synthesized at 800 °C annealing temperature. (N) NH_3 yields and Faradaic efficiencies after 2 hours of reaction at different potentials. Reproduced with permission from ref. 261. Copyright 2019, American Chemical Society.

environment and the electronic states are different for every exposed facet, and these results indicate that the pH and the exposed facets on the surface of the electrocatalyst affect NO_3RR accordingly. Fabrication of Au NPs with multiple high-index facets via a modified seed-mediated method can enhance the adsorption of *NNH intermediate, thus promoting the N_2RR reactions.[198] The adsorption of H*, an HER intermediate, is less on the high-indexed facets, which demotes the competing HER reaction, resulting in a moderately high FE of 73.32% for N_2RR at −0.3 V vs. RHE. Doping with heteroatoms can also impact the electrocatalytic performance. Cu-doped Fe_3O_4 particles can effectively reduce NO_3^- to NH_3 in a more thermodynamically facile manner with an effective FE ∼100% at −0.6 V vs. RHE.[253] Doping the catalyst surface with Cu lowers the energy barrier and strengthens the adsorption of different reaction intermediates. Doping with 0D materials like Ru atoms can also enhance the catalytic properties of emergent materials like MXenes.[254] Ru atoms can back-donate electrons to N_2, which increases its adsorption and activation. The thermodynamic energy required for the first hydrogenation

step is also lowered and these synergistic roles of Ru active sites promote N_2RR. Apart from crystal facet engineering and doping, the surface structure of electrocatalysts can also be modulated by defect engineering. Surface defects like oxygen vacancy (V_O) can tune the electronic structure of the metal with unsaturated coordination, allowing them to act as active sites to enhance the adsorption of O-containing species like NO_3^- on the surface of the electrocatalyst. Incorporation of the ultra-low level of Pd in Cu_2O induces hierarchical cavity defects and surface defects on the surface of octahedral Cu_2O.[255] The cavities and V_Os impart voids, which results in enhanced mass transport and adsorption of NO_3^- and H_2O reactants on the surface of Pd–Cu_2O. Moreover, the V_Os weaken the N–O bond of nitrates, and the Pd can act as active sites to generate active H_{ads} from H_2O, which helps in protonation to form NH_3. It is to be noted that different noble metals like nanocrystalline Pd,[256] nanocrystalline Ag,[199] and their composites like Ru/g-C_3N_4[257] and bimetallic Cu–Pt[258] have been used for catalytic NO_3RR. However, considering the scarcity of noble metals and their expensive nature, these are not very cost-effective. For this

This journal is © The Royal Society of Chemistry 2025

Chem. Soc. Rev., 2025, **54**, 5021–5080 | **5047**

reason, researchers have shifted their focus to lower-cost transition metal-based electrocatalysts. Several Bi-, Cu-, and Fe-based nanoparticle and single-atom catalysts with efficient and selective ammonia synthesis have been reported till now. One such work demonstrates that Bi-based-MOF, which acts as a precatalyst and, upon electroreduction, produces fragmented Bi^0 nanoparticles *in situ*.[201] The stable Bi NPs produced can act as effective N_2RR catalysts in both acidic and neutral reaction conditions, though the FEs reported are quite low due to competing HER. Zhou *et al.* have reported selective electroreduction of NO_3^- to NH_3 by *in situ*-generated 0D-Cu^0 cubes from its oxide (Cu_2O precursor) while the Cu/Cu_2O favours nitrite production.[259] Nitrate reduction at the 0D-Cu cubes is preferred because it has a lower activation energy barrier for nitrates when compared to Cu/Cu_2O and Cu microspheres. The intrinsic activity of NO_3RR is higher on 0D-Cu cubes than on 0D-Cu microspheres because the 0D-Cu cube surface has more Cu(100) facets, whereas the surface of 0D-Cu microspheres is dominated by Cu(111) facets. Atomically dispersed 0D materials like metallic clusters and single-atoms are emergent catalysts for ammonia synthesis owing to their novel features like unique coordination environment and high atom economy. Atomic dispersed Au nanoclusters (Au-NCs) prove to be effective electrocatalysts for ammonia synthesis when embedded on TiO_2 nanosheet support.[260] Pristine TiO_2 is not a very effective electrocatalyst for ammonia production due to lower charger transport and the absence of abundant catalytically active sites. However, the Au atoms in Au-NC/TiO_2 can significantly enhance the adsorption and activation of NO_3^- and promote the NO_3RR-to-NH_3 by lowering the energy activation barrier.

Single-atom (SA) confinement also proves to be an effective strategy for devising electrocatalysts that enhance the metal utilization efficiency in catalysis. Nowadays, the use of single-atom catalysts is quite frequent in HER, CO_2RR, NO_3RR, and metal-based SAs are prolific in electrocatalysis. Fe SAs and Cu SAs are the most widely used single-atom electrocatalysts for ammonia generation reported so far. The coordination environment of the single-atoms is vital because charge localization around the single-atom depends on the coordination. The coordination environment also impacts the electronic structure and geometry of the central single-atom and modulates the adsorption of reactants, which in turn has a direct effect on catalytic efficiency. The most common coordination is N_4. Fe–N_4 SAs have higher atomic site activity when compared to bulk or nanostructural catalysts due to a lower thermodynamic barrier.[262] Fe–N_4 coordination is also beneficial because due to the lack of neighbouring metal centres, N–N coupling cannot occur. This prevents the formation of N_2 and simultaneously promotes the selectivity of NH_3. To elucidate the structure–performance relationship, Liu *et al.* have prepared Fe active sites with three different coordination environments: square pyramidal Fe–N_4–OH, slightly broken square planar Fe–N_4, and trigonal pyramidal Fe–N_3.[204] The interaction between Fe atoms and O atoms of NO_3^- is determined using DFT, which reveals a strong overlap between the 3d orbitals of Fe and 2p orbitals of

O (NO_3^-) in the case of Fe–N_3 as the d orbitals are more localized in N_3 coordination when compared with Fe–N_4 and Fe–N_4–OH. This ensures that the adsorption of NO_3^- is more favourable on Fe–N_3, making Fe–N_3 a more active catalyst for NO_3RR. Also, the localization of electrons is near the N atoms for Fe–N_4 and Fe–N_4–OH, whereas for Fe–N_3 the electrons are at both the Fe and N sites, enhancing the charge transfer required for NO_3RR. Nitrate reduction can also be enhanced by changing the coordination environment from N_4 to N_2O_2.[263] The O atoms can regulate the d orbitals of Fe such that the adsorption energy of nitrates decreases on Fe–N_2O_2 when compared with Fe–N_4. The conversion of *NOH to *N is easier on Fe–N_2O_2. The conductivity and selectivity are also greater, which makes Fe–N_2O_2 a potentially better electrocatalyst than Fe–N_4. Besides N and O atoms, P atoms are also used for the coordination of single-atoms. The P atoms can break the local charge symmetry of the Fe atoms and facilitate the adsorption of nitrate as well as other key reduction reaction intermediates (Fig. 12I–K).[102] The atomic interface of the Fe atom is asymmetric, which optimizes the electron density in such a way that it lowers the energy of formation of the NO_3RR intermediates and effectively improves the catalytic performance. Cu SAs also play a predominant role in electrocatalytic NO_3RR as Cu is electroactive, has tuneable electronic structures, and is also cost-effective. The coordination environment for Cu SAs is also crucial for catalysis like Fe SAs. The most frequently used Cu SAs have Cu–N_4 coordination where the symmetry is C_{4v}.[205,264,265] Symmetric coordination induces weak polarity, which reduces the attractive power of active sites for NO_3^- and lowers ammonia production.[266] Asymmetric coordination like Cu–N_2O_2 in *cis* configuration has more polar active sites, which promotes the adsorption of NO_3^-.[221] Moreover, the *cis* configuration splits the 3d orbitals of Cu, which reduces the energy of the formation barrier of *ONH intermediate. Modification of the coordination environment to Cu–N_3C_1 has manifold benefits.[206] It increases the energy barrier of competing HER, reduces the desorption of intermediates produced, increases the adsorption of H*, and enhances the electrocatalytic hydrogenation process. However, the structural sensitivity of these metal SA catalysts can sometimes decrease the selectivity of ammonia. For instance, Co-based SAs can more selectively produce hydroxylamine (NH_2OH) from the electroreduction of NO, whereas metallic Co in a hexagonal close-packed (hcp) lattice produces NH_3 selectively.[267] The hcp-Co has excellent electron and proton transfer properties, resulting in superior activity for ammonia production. Co-SA has a positively charged active centre and this modified electronic structure accounts for the exceptional hydroxylamine selectivity. hcp-Co can lead to vertical and strong NO adsorption, whereas moderate adsorption occurs on the Co-SA. Hence, the formation of NOH* intermediate is more favourable over hcp-Co, while HNO* formation is preferable on Co-SA. This local structural difference between hcp-Co and Co-SA leads to the selective formation of NH_3 and NH_2OH, respectively.

Besides photocatalysis, 0D semiconductor nanoparticles can also perform efficient electrocatalysis owing to their

5048 | *Chem. Soc. Rev.*, 2025, **54**, 5021–5080

This journal is © The Royal Society of Chemistry 2025

conductive properties. For instance, nitrogen-impregnated carbon increases the conductivity and causes partial oxygen defects on the surface of TiO_2.[202] This leads to the coexistence of Ti^{3+} and Ti^{4+}, which increases charge transfer and, thus, facilitates the catalytic reactions. Here, in addition to ammonia, hydrazine is also obtained as a by-product for the electrocatalytic N_2RR, which somewhat limits the selectivity of ammonia. The formation of heterostructures can also improve the photocatalytic properties of TiO_2. In Cu nanoparticle-loaded oxygen-deficient TiO_2 (Cu NP–V_O–TiO_2), a strong metal support interaction is induced between Cu and TiO_2, improving electron density and electron transfer processes.[203] This interaction also modifies the local charge distribution properties of the catalyst such that it is asymmetrical, resulting in polarization of the adsorbed N_2 and, consequently, improved N_2 activation. The experimental results reveal that the oxygen vacancies and Cu NPs act as active sites, and the metal support interaction helps in electron transfer from Cu to the oxygen-deficient TiO_2. In N_2RR, no hydrazine has been obtained as a by-product, thus confirming the good selectivity of NH_3. Further, the absence of hydrazine indicates that the catalytic mechanism proceeds *via* the associative distal pathway.

Core–shell nanostructures are a class of 0D nanomaterials composed of an inner core and outer shell with a distinct boundary between them. The interface connectivity between the core and shell materials sometimes offers new properties like a tuneable electronic surface and abundant active sites, which are beneficial for catalytic reactions. The core–shell structures have another advantage in catalytic reactions. The thickness of the shells and the composition of the core materials can affect the adsorption–desorption properties of intermediates and products so that the catalytic activity can be tuned easily by modification of the core–shell structures and compositions. Qu *et al.* synthesized a core–shell structure comprising oxygen-containing molybdenum carbides (O-MoC) and nitrogen-doped carbon layers (N-doped C) by pyrolysis of ammonium heptamolybdate and dopamine, which can electrocatalytically reduce N_2 to ammonia (Fig. 12L–N).[261] The interaction between O-MoC and N-doped C results in an electronic structure that makes the competing HER negligible. This increases the FE of the catalyst, and no by-products like hydrazine are produced here, which also increases the selectivity of NH_3 produced.

5.2. 1D electrocatalysts and heterostructures

The structure of 1D materials has diverse advantages, which makes them prospective in the field of catalysis. The aspect ratio of length : height for 1D structures is always greater than 1. The diameter of the 1D nanowires can be tuned to match the wavelength of photons and the diffusion length of charge carriers, tailored to specific catalytic applications.[268] The high surface-to-volume ratio of these materials ensures the availability of enough active sites on the surface for catalysis. These characteristics alter the properties of 1D structures compared to their bulk counterparts, making them advantageous for catalysis. For instance, 1D Au nanowires coated with oxygen-

rich tannic acid can electrochemically reduce N_2 to NH_3.[210] Tannic acid is loosely packed on the surface of Au nanowires and has high porosity, which improves access to most of the metal sites on the surface of the catalyst for adsorption and activation of N_2. The oxygen richness of the coating at the gold and tannic acid interface enhances N_2RR. Hydrazine has not been detected at any potential, thus confirming the selectivity of NH_3. Examples of other catalytic nanowires include single-atom-dispersed Cu nanowires where single-atoms (SAs) like Ru and Rh dopants are atomically dispersed in a Cu nanowire matrix to form a 0D–1D type heterostructure.[208,209] The Ru/Rh SAs offer diverse atomic and electronic properties that make them suitable for catalytic conversion of nitrates to ammonia. The NO_3RR reaction occurs at the Ru/Rh sites while the Cu sites suppress the competitive HER. The selectivity of NO_3^- to NH_3 reaches as high as 99.8%. The authors have also coupled NO_3RR to the air-stripping process and successfully obtained NH_3 and NH_4Cl, thus proving that the system can convert the nitrates present in wastewater to value-added products. Cu materials are widely used for NO_3RR reactions because the energies of the d orbital of Cu and the lowest occupied π^* orbital of NO_3^- are similar, which is favourable for NO_3RR.[269] But Cu materials perform NO_3RR at comparatively negative potentials because of the low nucleophilicity and affinity of nitrate on the Cu surface, which makes the competing HER more favourable.[270] To address this issue, researchers have modified the electronic structure of Cu-based catalysts using metal heteroatoms or by doping with non-metals. For instance, B-doping in Cu nanowires can transfer electrons from the 3d orbitals of Cu to the empty 2p orbitals of B, thereby inducing electron localization and improving catalytic activity at the Cu sites.[271] DFT calculations indicate that boron incorporation also suppresses competing HER, increases the adsorption of intermediates like $*NO_3$, and enhances the conversion of $*NO$ to $*HNO$. According to a recent study, CO_2 molecules enhance the reduction of nitrites to ammonia on Cu nanowire catalysts, achieving a FE of nearly 100% in a broad potential range.[207] Reaction mechanism investigations show that CO_2 is first reduced to form $*CO$, which then facilitates the reduction of $*NO$ intermediates to $*N$. This leads to a decrease in the energy barrier of deoxygenation of $*NO$ intermediates, which is the rate-determining step of the nitrite electroreduction process. Additionally, the adsorbed $*CO$ species can accelerate the hydrogenation of $*NH_2$ intermediates to form NH_3 at an enhanced rate. Besides the electroreduction of nitrite, CO_2 molecules can also accelerate the reduction of other nitro-containing compounds such as the conversion of nitrate to ammonia and nitrobenzene to aniline.

Monometallic nanomaterials with unconventional crystal phases, such as face-centered cubic (fcc) and hexagonal close-packed (hcp) phases exhibit enhanced catalytic activities over their common phase counterparts. However, monometallic materials sometimes lack sufficient active sites for the adsorption and stabilization of multiple intermediates, particularly in multi-step reduction reactions like NO_xRR and N_2RR. In this attempt, multimetal alloy nanomaterials with unconventional

This journal is © The Royal Society of Chemistry 2025

Chem. Soc. Rev., 2025, **54**, 5021–5080 | **5049**

phases have been fabricated which can enhance the electrocatalytic reactions toward ammonia synthesis. One example of such alloy is Cu–Sn-based pine-needle structures that convert NO to ammonia in a flow cell.[61] Theoretical investigation implicates that the energy barriers of protonation are low over Cu_6Sn_5-derived surface structures, which results in enhanced ammonia production. IrNi-based alloy nanobranches (NBs) with unconventional hcp phase demonstrate superior electrocatalytic NO_2RR performance toward ammonia synthesis.[211] Solvothermally fabricated IrNi, IrRhNi, and IrFeNi alloy NBs consist of a Ni-rich core and an Ir-rich shell. Theoretical studies indicate that the Ir–Ni interactions within the hcp IrNi alloy can accelerate the electron transfer processes for NO_2RR. The hcp IrNi alloy surface also produces more active hydrogen, which reduces the energy barriers for the hydrogenation steps for ammonia formation.

One-dimensional carbon-based nanomaterials like carbon nanotubes (CNTs) and carbon nanorods (CNRs) exhibit excellent catalytic properties toward ammonia production, owing to their electron conductivity, large surface area, and stability. CNTs have a graphite sheet-like structure with sp^2 hybridized-C atoms, and the sheets can be rolled to form a cylinder-like structure.[272] The inner and outer walls of CNTs provide numerous active sites for catalysis. Single-walled and multi-walled carbon nanotubes (SWCNTs and MWCNTs) are promising 1D materials for efficient electrochemical NO_3RR. However, the work of Harmon et al. suggests that when heteroatoms like O and N are introduced into MWCNTs, the efficiency of catalytic NO_3RR decreases (Fig. 13A–C).[217] This observation proves that the catalytic reaction occurs at the C atoms present on the surface of the carbon nanotubes. The electron-rich O and N dopants reduce the number of active C sites on the surface, thus diminishing the catalytic reaction. Some Fe contaminant from the synthetic counterparts is present in SWCNTs, but not on the surface; hence, it does not affect the NO_3RR significantly. The authors also found that the surfaces of SWCNTs are more catalytically active and selective for NO_3RR than for MWCNTs. This might be because the SWCNTs have larger curvature than MWCNTs, which modifies the bonding and, consequently, the electronic structure of the active C atoms. For SWCNTs, the FE for NH_3 is 90% at -0.85 V vs. RHE. Other byproducts like gaseous H_2 (FE 6%), liquid NO_2^- (FE 4%), and NH_2OH are also detected. Carbon nanorods (CNRs) are one-dimensional rod-shaped carbon materials with a moderate aspect ratio, high surface area, and good conductivity. The electrocatalytic properties of CNRs can be modulated by doping with heteroatoms like N, and the incorporation of transition metals like Ni.[218] Ni-embedded N-doped carbon nanorods (Ni-NCNR) can selectively electroreduce nitric oxide to form ammonia. The Ni atoms act as the active sites for adsorption and activation of NO. N-doping alters the electronic structure and enhances the interaction between the Ni active sites and CNR support; hence Ni incorporation and N-doping synergistically enhance NORR for NH_3 production. N-doped 1D carbon nanofibers with carbon defects can also accelerate electrocatalytic N_2RR for NH_3 synthesis.[45] The carbon defects enhance the

water-splitting process, generating abundant protons for the protonation of N_2 to NH_3. Further, the C defects assist the coordination of the Fe atom with four N atoms. The $Fe–N_4$ sites, together with the adjacent C defects, promote the protonation reactions by reducing the energy barrier of the process, benefiting the overall N_2RR process.

Spinel oxides have a general formula of AB_2O_4, where A and B are transition metal cations. A is a divalent cation and B is a trivalent cation, occupying tetrahedral and octahedral sites, respectively.[273] Due to the distinct electronic structures and reactivities of A and B, their interactions with the reactants also differ significantly. Hence, spinel-type oxides have more catalytic activity compared to single-metal oxides. Bimetallic spinel oxides have a tuneable band gap, better electrical conductivity, and adsorption ability of reactants than single-metal spinel oxides.[274] Such a redox-active bimetallic spinel oxide, $NiCo_2O_4$, can perform electrocatalytic NO_3RR to NH_3 under ambient conditions (Fig. 13D–H).[214] These spinel oxides have multivalent metals and high electronic conductivity, which are favourable for catalytic reactions. Also, the effect of bimetallic centres Ni and Co result in efficient NO_3RR, and the FE reaches a maximum value of $\sim$99% at -0.3 V vs. RHE, although small amounts of NO_2^- and N_2H_4 were obtained as by-products with NH_3. Ni^{2+} acts like a p-type dopant and replaces a Co^{3+} in Co_3O_4 to form $NiCo_2O_4$. This converts the semiconductor minority spin channel to conducting, and $NiCo_2O_4$ possesses half-metal characteristics. The DFT calculations show that the half-metal characteristic of $NiCo_2O_4$ facilitates electron transfer. Nitrates are easily adsorbed on the surface of Co_3O_4 compared to $NiCo_2O_4$ but, surprisingly, the NO_3RR is more favourable for $NiCo_2O_4$. This proves that the Sabatier Principle holds correct, i.e., the adsorption of reactants on the surface should be intermediate, and too weak or too strong interaction disfavours the catalytic process. The catalyst is also used as a cathode in a $Zn–NO_3^-$ battery with a high yield of 48.5 μmol h^{-1} cm^{-2} NH_3 and an FE of 96.1%. Another such spinel oxide electrocatalyst, Mn-incorporated Co_3O_4 ($Co_3O_4–Mn_2$) nanotubes is synthesized via hydrothermal method and annealing (Fig. 13I–K).[215] Mn partially replaces the Co cation in the CoO_6 octahedron of Co_3O_4 to form $Co_3O_4–Mn_2$. Mn incorporation not only improves conductivity but also suppresses the HER. The surface sites of $Co_3O_4–Mn_2$ are less active than Co_3O_4. A Co : Mn ratio 1 : 2 produces the highest FE of 99.5% at -1.2 V vs. RHE. Doped spinel oxides like carbon-doped cobalt oxide (C/Co_3O_4) hollow nanotubes also exhibit highly efficient NH_3 synthesis from NO_2^- reduction with FE of almost 100% in the potential range of -0.1 to -0.6 V vs. RHE.[216] The C doping facilitates charge transfer by inducing a local electric field and reduces the energy barrier for the $*N + e^- + H_2O \rightarrow *NH + OH^-$ step, the rate-determining step of the NO_2RR process. This electrocatalytic system is further utilized to construct a $Zn–NO_2^-$ battery that can concurrently degrade NO_2^-, generate value-added NH_3, and create electricity.

Semiconductors are often used extensively as electrocatalysts. However, typical semiconductor materials have less electronic conductivity, which impedes their electrocatalytic
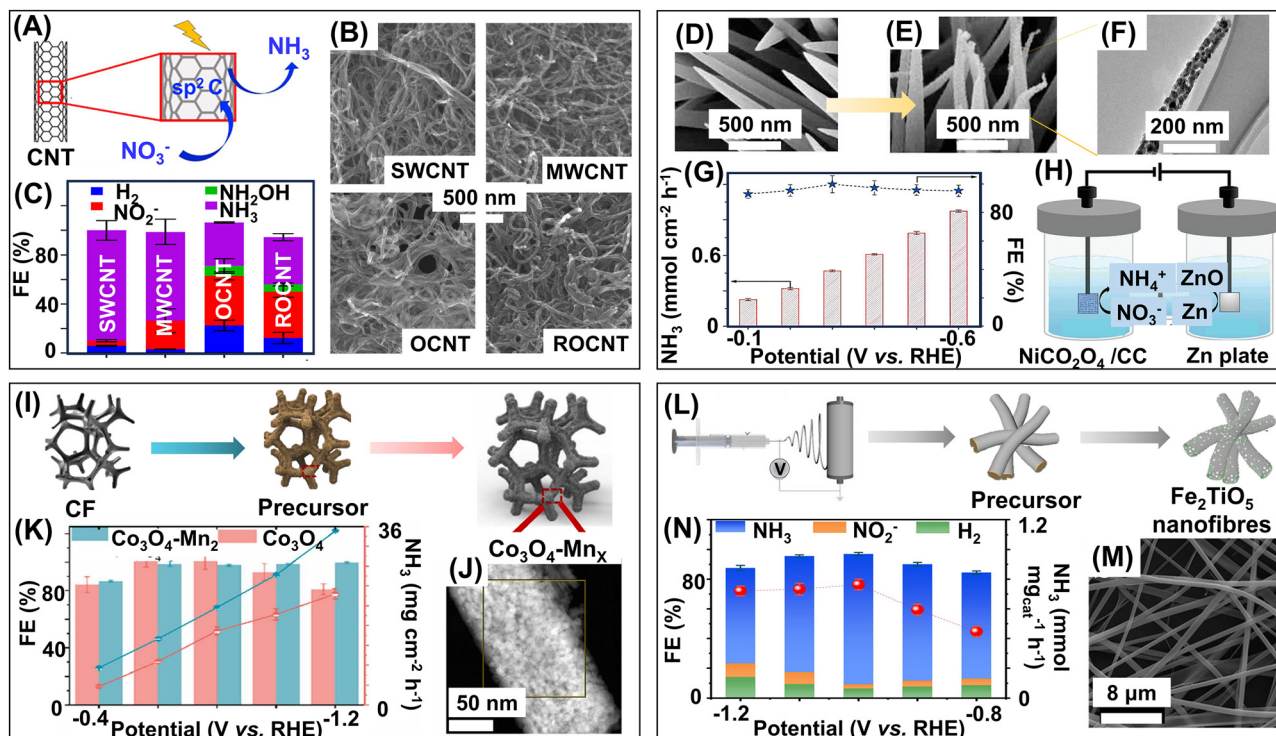
5050 | Chem. Soc. Rev., 2025, 54, 5021–5080

This journal is © The Royal Society of Chemistry 2025

Fig. 13 One-dimensional (1D) electrocatalysts for ammonia synthesis. (A) Schematic representation of electrochemical NO_3^- reduction to NH_3 by 1D carbon nanotube (CNT). (B) SEM images of single-walled carbon nanotubes (SWCNTs), multi-walled carbon nanotubes (MWCNTs), mildly oxidized MWCNTs (OCNTs), and reduced OCNTs (ROCNTs). (C) Faradaic efficiencies of possible products H_2, NO_2^-, NH_2OH, and NH_3 obtained from NO_3^- reduction using SWCNT, MWCNT, OCNT, and ROCNT catalysts. Reproduced with permission from ref. 217. Copyright 2022, American Chemical Society. (D) SEM image of NiCO precursor. (E) SEM image of $NiCO_2O_4$ obtained from the precursor upon annealing. (F) TEM image of $NiCO_2O_4$ nanowire. (G) NH_3 yields and Faradaic efficiencies obtained at different potentials using $NiCo_2O_4$/CC nanowire catalyst. (H) Schematic illustration of $Zn-NO_3^-$ battery using $NiCo_2O_4$/CC as the cathode. Reproduced with permission from ref. 214. Copyright 2022, Wiley-VCH. (I) Schematic representation of the fabrication of Mn-incorporated Co_3O_4 ($Co_3O_4-Mn_x$) nanotubes. (J) TEM image of $Co_3O_4-Mn_2$ nanotube, where Mn : Co ratio is 2 : 1. (K) NH_3 yields and Faradaic efficiencies obtained using $Co_3O_4-Mn_2$ and Co_3O_4 catalysts at various potentials. Reproduced with permission from ref. 215. Copyright 2023, Elsevier. (L) Schematic representation of the synthetic procedure of Fe_2TiO_5 nanofibers. (M) SEM image of Fe_2TiO_5 nanofibers. (N) Faradaic efficiencies of possible products H_2, NO_2^-, and NH_3 obtained from NO_3^- reduction using Fe_2TiO_5 nanofibers at different potentials. Reproduced with permission from ref. 106. Copyright 2022, Wiley-VCH.

activity. The electronic structure of semiconductors can be modified by introducing defects like oxygen vacancies (V_O) or by heteroatom doping. Besides modulating the electronic structure, doping TiO_2 nanobelts with the P atom induces charge redistribution and generates V_Os around the doping sites.[212] As a result, P-TiO_2 exhibits better NO$_2$RR performance to produce ammonia compared with pristine TiO_2. Amorphous boron carbide sputtered on TiO_2 (a-$B_{2.6}C$@TiO_2) nanobelts also exhibits selective NH_3 synthesis *via* electrocatalytic NORR.[213] Theoretical studies indicate that the B–C bonding in the boron carbide layer effectively injects electrons to the NO π_{2p^*} orbital, thus activating NO and ensuring the complete reduction of NO to NH_3 by lowering the energy barriers. Employing this electrocatalytic a-$B_{2.6}C$@TiO_2 as the cathode, a Zn–NO battery is assembled to produce ammonia and electricity concurrently. Pseudo-Brookite Fe_2TiO_5 nanofibers are narrow-band gap semiconductors with TiO_2-like atomic and electronic properties (Fig. 13L–N).[106] The highly reducing Fe atoms can easily replace the Ti^{4+} and induce abundant oxygen vacancies (V_Os) in the structure. The V_Os can reduce the adsorption energy of NO_3^-

and boost the catalytic activity for NH_3 production. Iron phosphide (FeP), a transition metal phosphide-based narrow-band gap semiconductor, is also an effective electrocatalyst for NO$_2$RR from wastewater to generate ammonia.[275] The NO_2^- ions bind to the (211) and (011) facets of the two adjacent Fe atoms present in FeP, which are the main active facets for NO$_2$RR. Further, FeP has moderate atomic hydrogen (H*) adsorption capability, which facilitates NH_3 formation, whereas excessive H* adsorption leads to competitive HER, reducing the selectivity of NH_3.

5.3. 2D electrocatalysts and heterostructures

Two-dimensional carbon-based electrocatalysts are emergent materials for the electrosynthesis of ammonia owing to their diverse benefits such as low cost, easy modification of atomic or molecular structures, and tolerance to acidic and alkaline electrolytes. State-of-the-art 2D carbon-based electrocatalysts for ammonia synthesis include graphene, graphdiyne, and carbon nitrides. These materials also provide superior support for anchoring 0D or 1D nanomaterials to promote their

This journal is © The Royal Society of Chemistry 2025

Chem. Soc. Rev., 2025, **54**, 5021–5080 | **5051**

catalytic activity. Engineering their structures by introducing defects or heteroatom doping are various strategies to enhance their catalytic activity. Graphene, one of the most commonly used 2D catalysts, has a nanosheet-like structure with sp^2 hybridized carbon atoms, and excellent conductivity and chemical stability.[276] The 2D π-conjugated structure of graphene also contributes to the adsorption of N-containing reactants on its surface and facilitates the catalytic reaction. Recently, amorphous graphene has been used extensively for catalytic purposes. The amorphous atomic structural features, as well as the graphene structural features, promote catalytic activity. Such an amorphous graphene electrocatalyst is synthesized by laser irradiation and is composed of disordered four- to eight-membered polygons (Fig. 14A–C).[219] The catalytic activity of amorphous graphene has been compared with crystalline reduced graphene oxide (rGO). It is observed that the adsorption properties of amorphous graphene are more due to structural deformations while rGO has lower adsorption properties due to aromaticity. Another graphene-based catalyst with amorphous/crystalline heterophase is synthesized by infrared laser induction.[220] This graphene has intermediate crystallinity between amorphous carbon and crystalline graphene, and contains aromatic rings and distorted polygons. The presence of heterophase can modulate the electronic properties of the catalyst as the density of defects and state near the Fermi level increases, resulting in high capacitance. The heterophased graphene has abundant electrons and long-range disorders that favour $8e^-$ NO_3RR to NH_3. The formation of heterostructures with graphene has certain advantages: (i) promotion of the transfer of electrons to graphene is readily achievable because the Fermi level of graphene is at 0 V vs. NHE, whereas the position of the conduction band of the other component is generally higher than the Fermi level of graphene; (ii) separation of charge carriers is easier due to the rapid electron transfer from the second catalytic component to graphene; (iii) abundant anchoring sites are present in functionalized graphene for the dispersion of nanoparticles or single-atoms. Single-atoms (SAs) are one of the most emerging catalysts in recent times as discussed above. The SAs mostly coordinate to four N atoms, but this induces weak polarity to the SAs, which is unsatisfactory for catalytic processes. If this coordination with N can be partially substituted with heteroatoms like O or S, then the polarity on SA sites will increase, resulting in the adsorption of more NO_3^-. Functionalized graphene with two N and two O in cis configuration can encapsulate Cu SAs.[221] As discussed before, the polarity of Cu sites causes more NO_3^- adsorption on the electrocatalytic surface and the cis configuration modifies the 3d orbitals of Cu so that it can form a π-complex with *ONH and reduce the energy barrier of the catalytic process. This reveals that functionalized graphene can also moderate the coordination of the SA catalyst and simulate its catalytic activity.

Graphdiyne (GDY), a carbon allotrope with one-atom-thickness is an emerging 2D carbon material. It comprises sp and sp^2 hybridized carbon atoms and has unique properties like high surface area, large cavity structure, large network plane, excellent hole transport properties, uneven surface charge, and multiple active sites, which make it an excellent two-dimensional catalyst.[193,277] Recent studies indicate that GDY-based low-dimensional materials exhibit excellent activity, selectivity, and stability toward electrocatalytic ammonia synthesis. Due to the presence of the reductive alkaline bond in the structure of GDY, it can self-reduce Pd^{2+} to form Pd-GDY.[278] The coupling interaction between the Pd, C1, and C2 sites of GDY enhances the electron transfer process, thereby increasing the activity and selectivity of electrocatalytic N_2RR to produce ammonia with 100% selectivity in a neutral medium. Individual zero-valent atoms have unique catalytic properties owing to their electronic structure, high activity, and selectivity. One such zero-valent Mo^0-GDY catalyst has been prepared based on the incomplete electron transfer properties between the GDY and Mo atom.[222] The atomically dispersed Mo^0 atoms endow the catalyst with excellent activity toward electrocatalytic nitrogen reduction and hydrogen evolution reactions with highly efficient ammonia and hydrogen production, respectively. The confinement of single-atoms (SAs) like Ru, Rh, and Co in GDY structures also confers excellent properties toward electrocatalytic nitrogen reduction reactions to produce ammonia.[271,279] Single-atom (SA) and double-atom (DA)-adorned GDY like Cu_2-GDY also exhibits enhanced NORR for ammonia generation.[224] This work shows that the d-band centre plays a pivotal role in the adsorption and hydrogenation of NO. The NO molecule activation on SAs and DAs is driven by electron "donation/back-donation" interactions between the metal atom and NO. On the SAs, the thermodynamic process (NH_3 and H_2O molecule desorption) dominates the entire NORR process, and Cu-GDY exhibits high NORR with selective NH_3 formation over H_2. In contrast, on the DAs, the electrochemical hydrogenation processes control the NORR, and Cu_2-GDY exhibits the highest selectivity toward NH_3 among Fe_2, Co_2, Ni_2, and Cu_2. These works explore the utilization of hybridized 0D atomically dispersed catalysts on 2D GDY-based structures toward electrocatalytic ammonia generation. Over the past few years, GDY-based heterojunction catalysts have also been developed to enhance electrocatalytic ammonia synthesis. For instance, the Fe_3C@GDY heterojunction catalyst has electron-donating triple bonds in GDY and electron-accepting Fe_3C, wherein, the sp-carbon–metal–carbon structures at the interface promote charge transfer and electrical conductivity in the catalyst.[225] GDY can also regulate the coordination environment of the Fe atoms and thereby improve the adsorption and desorption of the reactants and intermediates, promoting electrocatalytic nitrate reduction to ammonia. The incomplete charge transfer between the donor–acceptor Fe_3C@GDY interface also enhances the activity and selectivity of the catalytic ammonia production. Compared to the pristine catalysts, the heterogenized GDY structures have faster electron transfer properties and the integration with GDY also provides enhanced stability to the heterogenized catalysts.

Boron (B)-based carbon 2D materials have also emerged as efficient electrocatalysts for ammonia synthesis. Doping carbon-based materials with boron or nitrogen results

5052 | Chem. Soc. Rev., 2025, 54, 5021–5080

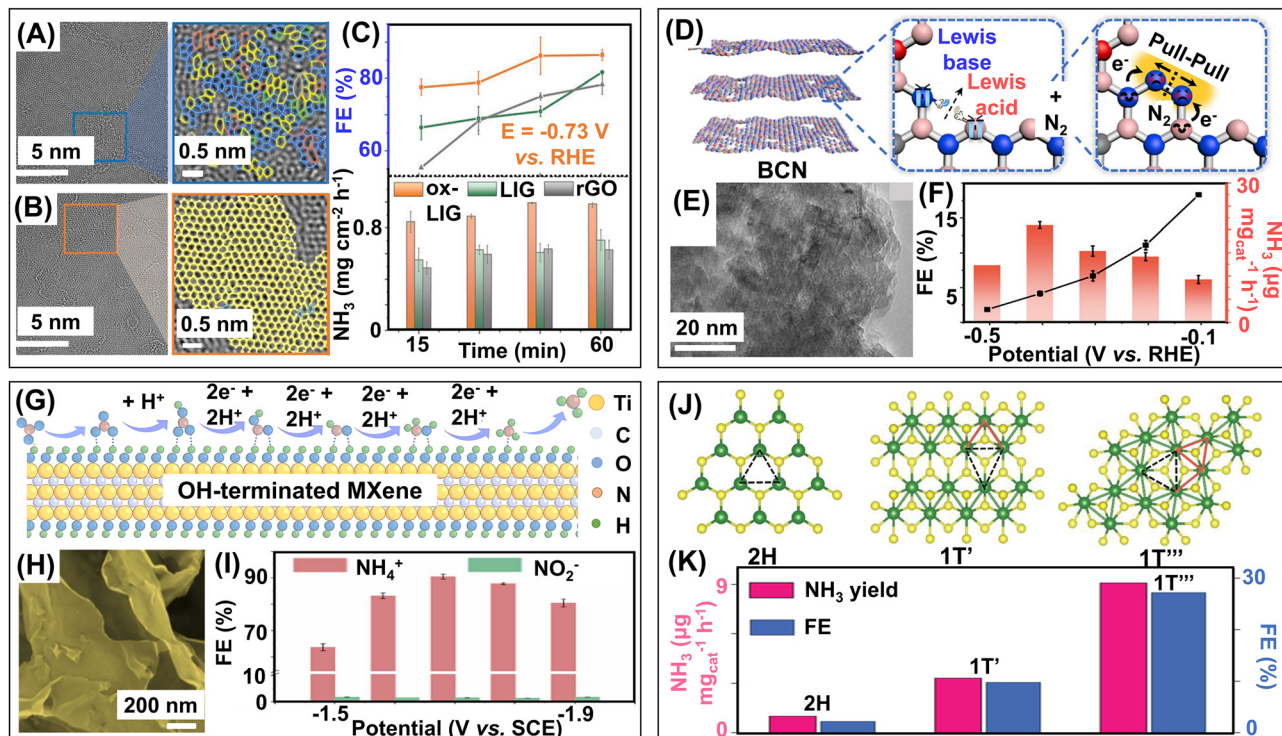This journal is © The Royal Society of Chemistry 2025

Fig. 14 Two-dimensional (2D) electrocatalysts for ammonia synthesis. (A) HRTEM images of amorphous graphene obtained by laser induction in air (ox-LIG) at different magnifications. (B) HRTEM image of reduced graphene oxide (rGO) at different magnifications. (C) NH$_3$ yields and Faradaic efficiencies obtained at different time intervals using amorphous graphene obtained by laser induction in air (ox-LIG), in an inert atmosphere (LIG), and reduced graphene oxide (rGO) at a potential of −0.73 V vs. RHE. Reproduced with permission from ref. 219. Copyright 2023, Wiley-VCH. (D) Schematic representation of defective boron carbon nitride (BCN) nanosheets with unsaturated B and N atoms as a frustrated Lewis pair (FLP). The pulling effect of FLPs captures and activates N$_2$, for N$_2$ reduction to NH$_3$. (E) STEM image of BCN. (F) NH$_3$ yields and Faradaic efficiencies obtained using BCN catalyst at different potentials. Reproduced with permission from ref. 227. Copyright 2022, Wiley-VCH. (G) Schematic representation of OH-terminated Ti$_3$C$_2$ MXene, where the hydrogen bonding between −OH groups and NO$_3^-$ facilitates NO$_3^-$ reduction to NH$_3$. (H) SEM image of Ti$_3$C$_2$ MXene. (I) Faradaic efficiencies of NH$_4^+$ and NO$_2^-$ obtained at different potentials using Ti$_3$C$_2$ MXene. Reproduced with permission from ref. 233. Copyright 2023, Wiley-VCH. (J) Lattice structures of the 2H, 1T′, and 1T″ phases of MoS$_2$. (K) Comparison of NH$_3$ yields and Faradaic efficiencies for 1T‴ and 1T′ MoS$_2$ at a potential of −0.3 V vs. RHE and for 2H MoS$_2$ at a potential of −0.4 V vs. RHE. Reproduced with permission from ref. 238. Copyright 2021, Wiley-VCH.

in charge redistribution, boosting the chemisorption of reactants.[280] The B and N doping also tune the band gap, spin, and charge density of the boron carbon nitride (BCN), promoting N$_2$RR and NO$_x$RR over HER. The empty sp^2 orbital of B can interact with the lone pair of N electrons to adsorb and activate the N-species and hinder the binding of H$^+$ to suppress the competitive HER. Surface anion vacancies can enhance the availability of electrons and provide suitable active sites for binding N$_2$ molecules. Defective BCN nanosheets with unsaturated B (e$^-$-deficient) and N (e$^-$-rich) atoms form the frustrated Lewis acid (LA) and base (LB) pairs (Fig. 14D–F).[227] These adjacent LA and LB pairs can efficiently adsorb N$_2$ to form a six-membered ring as an intermediate and allow dissociation of N≡N at much lower energy due to the pull–pull effect by heterolysis. The presence of frustrated Lewis pair B and N as dual active sites increases the electrocatalytic activity of BCN and promotes N$_2$RR. The tunability of the Lewis pairs of B and N has substantial impacts on N$_2$RR.[226] The B-enriched BCN exhibits better N$_2$RR activity than the N-enriched BCN. Theoretical studies indicate that the energy of each step of N$_2$RR by

B-enriched BCN is relatively lower than that of N-enriched BCN, which results in enhanced N$_2$RR by B-BCN.

2D metal and metal oxide-based nanostructures are extensively used in electrocatalysis due to their high surface-to-volume ratio, unique electronic structures, and abundant exposed active sites. For instance, Ru nanosheets with low coordination numbers can exhibit electrocatalytic properties toward NORR to NH$_3$.[228] The low coordination number of the Ru sites promotes the adsorption of NO molecules and lowers the energy barrier of the rate-determining hydrogenation step. The use of expensive noble metals can be circumvented by replacing them with redox-active transition metals, such as Co. Co nanosheets with hexagonal-close-packing (hcp) act as efficient catalysts for NORR compared to the face-centered cubic (fcc) phase of Co nanosheets.[229] Enhanced electron donation from the d-π* orbitals of hcp-Co to the adsorbed *NO facilitates NORR. Additionally, the proton diffusion process in the hcp-Co is energetically favourable, ensuring the availability of more protons for the protonation of NO to NH$_3$. Bimetallic catalysts provide more active sites than monometallic catalysts for

This journal is © The Royal Society of Chemistry 2025

Chem. Soc. Rev., 2025, 54, 5021–5080 | 5053

multistep N_2RR and NO_xRR and are often used to synthesize ammonia as they mimic bimetallic nitrogen reductase (MoFeP). A bio-inspired CuCo bimetallic nanosheet mimicking Cu–nitrogen reductase is formed by electrodeposition of the corresponding metals and this bimetallic catalyst can electroreduce NO_x^- to NH_3.[230] The two active metal centres in the catalyst have separate roles—the Cu centre facilitates the adsorption of NO_x^- while the Co centres participate in the donation of electrons and protons. DFT calculations show that the adsorption of *NO (the rate-determining step) consumes less energy for CuCo, when compared to Cu and Co metals, separately. The FE for the $Cu_{50}Co_{50}$ catalyst reaches $\sim$100% at -0.2 V $vs.$ RHE with a current density of 1035 mA cm^{-2}. Metal oxides with defects and vacancies can also enhance the catalytic activity of N_2RR and NO_xRR by altering the local coordination environment and electronegativity. Amorphous RuO_2 nanosheets exhibit superior NO_3RR when compared to their crystalline counterparts.[231] This superiority is attributed to atomic disorder in the structure of RuO_2, which endows it with numerous oxygen vacancies (V_OS). The rate-determining step is calculated to be the conversion of *NH_2 to *NH_3, which is facilitated on the surface of amorphous RuO_2. The formation of by-products like NH_2OH and H_2 are also suppressed on amorphous RuO_2, which boosts the selectivity of NH_3.

MXenes formed of carbides and nitrides are emerging 2D materials used in catalysis as they have unique properties like high electrical conductance and capacitance.[281,282] The introduction of defects on the surface reduces repulsive electrostatic forces and thus decreases the energy required for the adsorption of N_2 or NO_x^-.[283] Functionalization of MXenes suppresses competitive HER and improves the catalytic synthesis of ammonia.[232] Functionalized Ti_3C_2 MXenes with terminal oxygen groups formed by mild calcination reveal the active sites for electrocatalytic NO_3RR (Fig. 14G–I).[233] Small amounts of N_2 and hydrazine by-products are obtained, resulting in moderate selectivity of NH_3 with an FE of 90.4% at -1.7 V $vs.$ RHE. Under electrochemical conditions, the oxygen groups are converted to hydroxyl groups in $situ$ to form interfacial hydrogen bonding, thus accelerating the electrocatalytic NO_3RR process. These surface hydroxyl groups help the adsorption of NO_3^- and contribute to hydrogenation, forming NH_3; hence, the –OH group functions as both an active site and a reactant. The adsorption of H on the O atoms also diminishes the HER process, increasing the selectivity of NH_3. Like other 2D materials, heteroatom doping of MXenes can also effectively increase the rate of NO_3RR and enhance the formation of NH_3. Doping of B atom into the lattice of B-$Ti_3C_2T_x$ (T_x depicts the surface terminating group) MXenes can alter their electronic structure and accelerate the NO_3RR kinetics compared to the pristine $Ti_3C_2T_x$ MXenes to produce ammonia with a high current density and at a low working potential.[234] The B dopants facilitate the adsorption and activation of NO_3RR intermediates, reduce the energy barrier and thereby enhance ammonia production.

MBenes, a newly emerging class of 2D layered materials similar to MXenes, are gaining attention as promising electrocatalysts. Unlike MXenes, MBenes lack passivating surface functional groups, which allows the constituent metal and boron atoms to be fully exposed, enhancing their catalytic activity. The combined effects of metal and boron make MBenes attractive catalytic materials. The metal atoms participate in water splitting and the boron atom activates the N-containing species. A FeB_2 MBene synthesized via the reflux method exhibits efficient NO_3RR with an FE of 96.8% at -0.6 V $vs.$ RHE.[235] Fe acts as the *H donor and B atoms act as the *H acceptor, and this tandem action promotes the NO_3RR process. Theoretical studies reveal that the adsorption and activation of NO_3^- take place at the B sites rather than Fe, confirming B as the active site for catalysis. Water catalysis occurs at Fe and the *H that is generated is transmitted to B through the hydrogen spillover process for subsequent hydrogenation reactions. Another study screens a series of M_2B_2-type (M = IVB to V transition metals from the periodic table) MBenes for electrocatalytic NORR.[284] Among the screened MBenes it has been observed that the Fe_2B_2, Mn_2B_2, and Rh_2B_2 can efficiently convert NO to NH_3 with smaller limiting potentials, whereas Nb_2B_2 and Hf_2B_2 have low limiting potentials for the NO conversion to NH_3. Mechanistic investigations indicate that hydrogenation of *NO to *NOH has lower energy than *HNO; hence, these MBenes have high selectivity for promoting the NORR to NH_3 over competitive HER.

Layered transition metal chalcogenides like MoS_2 have also been actively used as catalysts for N_2 and NO_x^- reductions. The positive charge on the Mo atom can polarize and activate the adsorbed reactants via Mo–N interactions. Heteroatom doping and defect engineering techniques have been employed to enhance the interaction between Mo and N species. Layered structured MoS_2 is a well-known catalyst for HER. Substituting S atoms with F introduces strain in the layered structure and compresses the interlayer spacing in the MoS_2 nanosheets.[236] Additionally, F is more electronegative than S and these factors can suppress HER and promote N_2RR. The introduction of defects in the form of dopants like V can remarkably enhance the efficiency of electrocatalytic NO_3RR.[237] V is highly conductive and can alter the electronic structure of the MoS_2 metalloenzyme. The V-MoS_2 electrocatalyst can lower the energy barrier of conversion of NO* to NOH* and also enhance the selectivity of NH_4^+. Recent works reveal that the metastable phase of MoS_2 is more active for performing catalytic reactions and can efficiently reduce N_2 to NH_3 (Fig. 14J–K).[238] Metastable MoS_2 provides access to partially filled t_{2g} orbitals, which can simultaneously form σ bonds with N and transfer electrons to N_2. The work compares the 2H (stable), 1T′, and 1T‴ (metastable) phases of MoS_2 for the catalytic reactions, and the 1T‴ phase with maximum electron density was found to be the most suitable for N_2RR. Mo–Mo clustering in the metastable phases is responsible for the enhanced electron density in these phases, facilitating activation of N_2 and accelerating N_2RR, which is almost nine times greater than the stable 2H phase. MoS_2 nanosheets deposited on graphite can also produce ammonia from the electroreduction of NO.[285] The positively charged Mo-edge sites of MoS_2 promote the adsorption

5054 | $Chem. Soc. Rev.$, 2025, **54**, 5021–5080

This journal is © The Royal Society of Chemistry 2025

and activation of NO *via* an "acceptance–donation" mechanism, which promotes NORR to NH_3 and disfavours the binding of protons and coupling of the N−N bond, ruling out the formation of H_2 and N_2 and enhancing the selectivity of NH_3 produced.

5.4. Metal–organic framework (MOF)-based electrocatalysts and heterostructures

Metal–organic frameworks (MOFs), composed of metal ions or clusters linked by organic ligands in a three-dimensional arrangement, are one of the most explored emergent materials in catalysis. Their porous structure, high specific surface area, excellent stability, and presence of active sites offer unique features required for catalysis. For instance, a 2D Cu-based MOF, $\{[Cu(HL)]·H_2O\}_n$, (Cu-OUC, H_3L = 5-(2′-carboxylphenoxy)isophthalic acid) exhibits efficient electrocatalytic NO-to-NH_3 conversion.[239] The Cu-OUC MOF activates NO *via* a two-way charge transfer mechanism of "electron acceptance and donation", where the *NO formation step is the rate-determining step. Additionally, the Cu-OUC MOF also acts as the cathode for constructing a Zn–NO battery, which besides converting harmful NO into NH_3 also generates electricity. The reaction rates of ammonia formation depend on the type of metal centres present in the MOFs. In Fe_2M trinuclear cluster-based MOFs, where M = Co, Ni, Fe, Zn, the rates of adsorption and activation of nitrate and protons are in the order of Co > Fe > Ni > Zn (Fig. 15A–C).[240] The unsaturated metal sites of the trinuclear complex help in the adsorption and reduction of nitrates while the dinitrogen ligand aids in the interfacial transfer of electrons due to the delocalized conjugation between the lone electron pairs of nitrogen and the π electrons of the ligand's aromatic ring. Ammonium sulfate is obtained by the electroreduction of nitrates and can be directly used as fertilizer for plants without further processing. MOFs have also been used as precursors for deriving metal- and carbon-based catalysts, which inherently have higher reactivity and stability when compared to conventional catalysts. $Co–Fe/Fe_2O_3$ has been derived from Co-doped Fe-MOF-74 by pyrolysis, where Co dopant increases conductivity and tunes the electronic properties such that $Co–Fe/Fe_2O_3$ shows efficient electrocatalysis.[286] The temperature at which pyrolysis is carried out is crucial as experimental evidence suggests that the graphitic carbon produced at 900 °C shows the highest electrocatalytic performance while that produced at 1000 °C shows reduced catalysis due to the collapse of structural properties. The Co center activates NO_3^- and tunes the energy of the d orbitals of adjacent Fe atoms, facilitating charge transport; thus, both Co and Fe atoms participate in NO_3RR. Co also restrains HER, thus increasing the selectivity and FE to 99% and 85.2%, respectively. The conversion of NO_3^- to NH_3 involves deoxygenation and hydrogenation of nitrates with water *via* proton-coupled electron transfer. This coupling reaction between nitrates and water can be boosted if a multifunctional interface can be produced by incorporating a second component with the MOF. For instance, when the bimetallic Ni/Co-MOF interface is surface-coated with H-substituted graphdiyne, deoxygenation, and hydration reactions are promoted due to the formation of the multifunctional interface (Fig. 15D–F).[241] The intersection

between the MOF and graphdiyne acts like a bifunctional membrane by facilitating the transport of electrons and reactants to the Ni and Co sites, where the concerted reaction occurs. An integrated-electrocatalysis cell using MOF-based gas diffusion electrodes (GDEs) can electroreduce NO (NORR) and electrooxidize NO (NOOR) simultaneously to produce NH_4NO_3 under dilute concentrations of NO.[287] For preparing the MOFs-GDEs, UIO-66, ZIF-8, and ZIF-67 are modified with Cu nanowires for NORR and Ni/NiO for NOOR to enhance the production of NH_4^+ and NO_3^-, respectively. The enhanced NO reduction and oxidation is due to the transfer of adsorbed NO from the adsorption layer to the catalyst layer, which is experimentally verified by the enhanced NO mass transfer from gas to electrolyte across the modified electrode. Modifying MOFs without doping or other functionalization can improve fabrication time efficiency and enhance material properties for ammonia production. One such example is Fe metal center-based MOF, which in its thermally activated form can generate ammonia with FE of $\sim$90% at −1.0 V *vs.* RHE, which is much higher when compared with the non-activated pristine form of the MOF (Fig. 15G–I).[242] The activation of MOFs is expected to provide access to more active Fe sites for the adsorption of nitrates. The thermal activation process frees the pores of the MOF from trapped components and exposes the high-valent Fe(III) sites for the catalytic reaction. Such activation processes can further open avenues for tailoring the surface structures of desired electrocatalysts like MOFs for energy conversion reactions.

5.5. 3D-printed electrodes based on low-dimensional materials

To design active and stable electrocatalysts for ammonia production, researchers have focused on designing 3D-printed electrodes. Previously, 3D-printed electrodes have been employed in catalytic reactions like carbon dioxide reductions,[18] oxygen evolution,[288] and hydrogen evolution[289] reactions; however, the use of 3D electrodes in N_2RR and NO_xRR is quite recent and has some advantages over conventionally prepared catalysts. The 3D printing technique enhances the designing of the catalysts and the reaction vessels by automating the prototype and simulations to prepare an optimized catalytic system.[48] This eliminates the manual time required for optimization for conventional catalysts, boosting the performance of the process. The 3D printing process allows for precise control over the shape, structure, and geometry of substrates, leading to enhanced catalytic performance. The 3D-printed substrates can be post-modified with desired active materials by sintering, sputter coating, electrodeposition, and atomic layer deposition.[290–293] For instance, in a recent study by our group, a Cu electrode is fabricated by fused fabrication filament (FFF) 3D printing (Fig. 16A–I).[243] The 3D-printed electrode is subjected to thermal treatment and sintering to induce conductivity and the metallic phase to the electrode. An electrochemical modification is then induced to the electrode followed by $NaHCO_3$ treatment for forming nanostructures on the surface of the electrode with exposed (100) facets. The main composition of the electrode responsible for electrocatalytic NO_3RR has been observed to be Cu/Cu_2O. These 3D-printed Cu electrodes can perform efficient NO_3^--to-NH_3 conversion with FE 96.5% at

This journal is © The Royal Society of Chemistry 2025

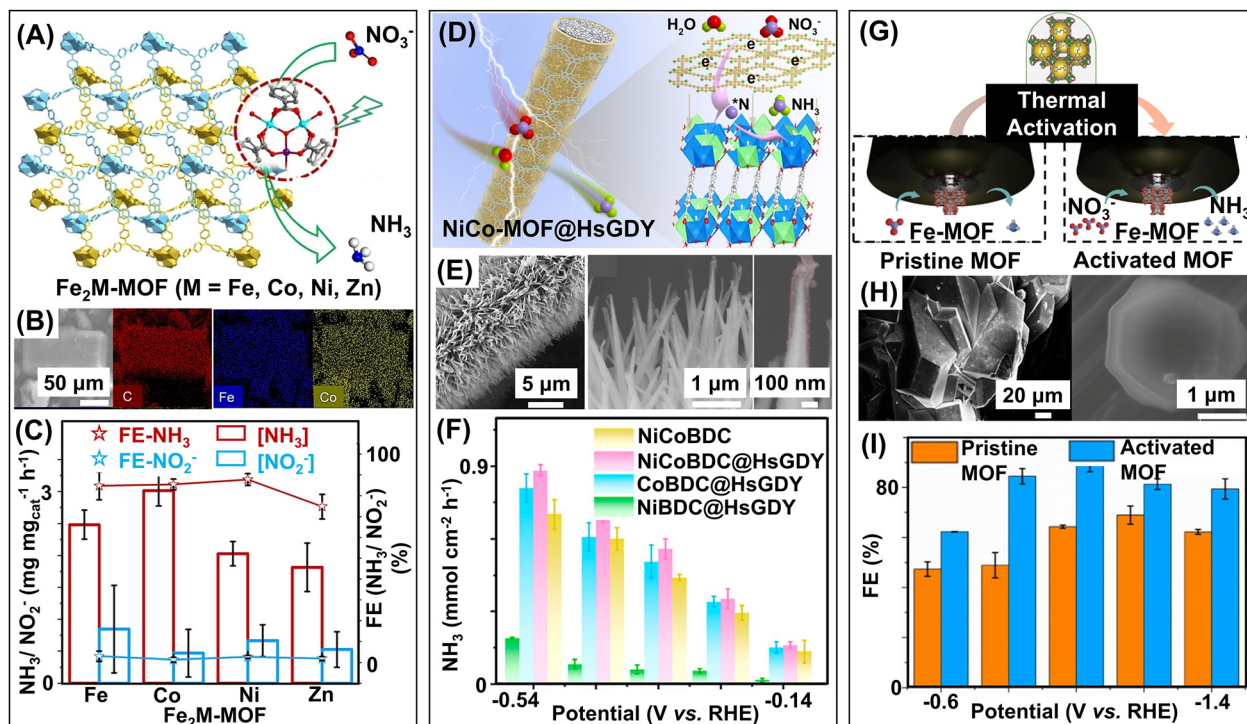*Chem. Soc. Rev.*, 2025, **54**, 5021–5080 | **5055**

Fig. 15 Metal–organic framework (MOF)-based electrocatalysts for ammonia synthesis. (A) Schematic representation of NO_3^- reduction to NH_3 by Fe-based trinuclear cluster metal–organic framework (MOF) Fe_2M-MOF, where M = Fe, Co, Ni, or Zn. (B) SEM image and element mapping of C, Fe, and Co present in Fe_2Co-MOF. (C) NH_3 and NO_2^- yields and the corresponding Faradaic efficiencies using Fe_2M-MOFs at a potential of −1.1 V vs. RHE. Reproduced with permission from ref. 240. Copyright 2023, Wiley-VCH. (D) Schematic representation of Ni/Co-MOFs (NiCoBDC) with hydrogen-substituted graphdiyne (HsGDY) nanowire array for electrochemical NO_3^- reduction to NH_3. (E) SEM images of NiCoBDC@HsGDY nanoarray at different magnifications. (F) NH_3 yields at different potentials using NiCoBDC, NiCoBDC@HsGDY, CoBDC@HsGDY, and NiBDC@HsGDY. Reproduced with permission from ref. 241. Copyright 2023, American Chemical Society. (G) Schematic representation of the thermal activation of the Fe-MOF from pristine to activated form. (H) SEM images of activated Fe-MOF at different magnifications. (I) Comparison of Faradaic efficiencies for NO_3^- reduction between pristine and activated Fe-MOFs at different potentials. Reproduced with permission from ref. 242. Copyright 2023, American Chemical Society.

−0.92 V vs. RHE with 95.6% selectivity for NH_3. Another work from our group compares the electrocatalytic properties of two 3D-printed electrodes: (i) 0-dimensional porous carbon black and (ii) 1-dimensional porous carbon nanotubes (Fig. 16J–M).[244] The 0D carbon black 3D-printed electrode is electrocatalytically inert while the 1D carbon nanotubes actively participate toward NO_3RR. The defects and metallic impurities (TiO_2, Fe_3O_4) in 1D CNTs can impact the electrocatalytic reactions. However, the exact content and distribution of the impurities and defects are not quantifiable in industrial catalysts; hence, proper control over electrocatalysis is not always possible over industrial catalysts. To achieve better control, an ultra-thin layer of manganese oxide is deposited onto the 1D carbon nanotubes using the atomic layer deposition technique. This fine-tunes the surface properties of the catalysts and enhances their electrocatalytic performance. The carbon nanotubes are conductive and manganese oxide has electrocatalytic properties, and the synergistic effect from these two components makes the 3D-printed 1D $CNT@MnO_x$ efficient toward NO_3RR. Surface-modified 3D-printed carbon substrates with atomic layer deposition (ALD) of TiO_2 can function as bifunctional platforms for electrocatalytic nitrite oxidation reaction (NO_2OR) and nitrite reduction reaction (NO_2RR).[245] This 3D-printed heterostructure possesses the intrinsic surface properties of carbon

nanotubes as well as Ti-dominated metallic impurities, and the formation of interfaces between the conductive carbon and ALD-coated TiO_2 enhances its electrocatalytic properties toward both NO_2OR and NO_2RR. The electrocatalytic properties of the TiO_2-coated 1D carbon electrode are associated with the ALD-coated TiO_2 layer, which can be tuned by modulating the number of ALD cycles. The 100-TiO_2 electrode, formed by non-continuous TiO_2 deposition on the 1D carbon framework is endowed with abundant carbon/TiO_2 interfaces. These interfaces play a vital function in the electrocatalytic reactions and enhance the formation of NH_4^+ and NO_3^- from electro-reduction and oxidation, respectively.

6. Low-dimensional photoelectrocatalysts for ammonia synthesis

Photoelectrocatalysts combine the dual benefits of both photocatalysts and electrocatalysts. Photocatalysts provide light energy for catalysis, and electrocatalysts offer the advantage of the electric bias. In conventional photocatalysts, the efficiency is sometimes limited by the recombination of the charge

5056 | Chem. Soc. Rev., 2025, **54**, 5021–5080

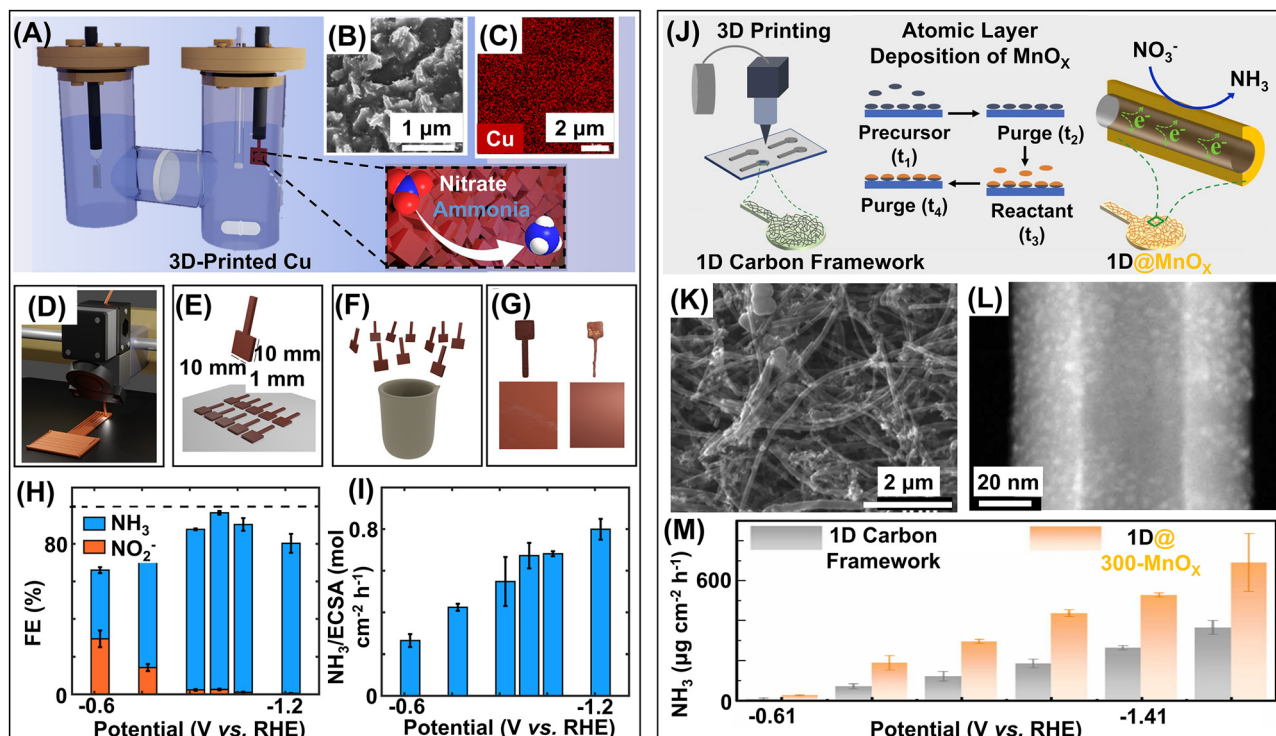This journal is © The Royal Society of Chemistry 2025

Fig. 16 3D-printed electrodes designed with low-dimensional materials for ammonia synthesis. (A) Schematic representation of the electrocatalytic cell for NO_3^- reduction to NH_3 using a 3D-printed Cu electrode. (B) SEM image and (C) Cu elemental mapping of the electrode. (D) Schematic representation of the 3D-printed electrode. (E) Pictorial representation of the dimensions of the electrodes, where the length and width are 10 mm each, and the height is 1 mm. (F) Sintering of the electrodes. (G) 3D-printed Cu electrode before (left) and after (right) acid treatment. (H) Faradaic efficiencies of NH_3 and NO_2^- at different potentials using 3D-printed Cu electrodes. (I) NH_3 yields at different potentials using 3D-printed Cu electrodes. Reproduced with permission from ref. 243. Copyright 2023, American Chemical Society. (J) Schematic representation of NO_3^- reduction to NH_3 using 1-D@MnO_x fabricated by atomic layer deposition of MnO_x on a 3D-printed 1D carbon framework. (K) SEM image of 1D carbon framework. (L) HAADF-STEM image of 1D@500-MnO_x. (M) NH_3 yields at different potentials using 3D-printed 1D carbon and 1D@500-MnO_x electrodes. Reproduced with permission from ref. 244. Copyright 2023, Elsevier.

carriers. In photoelectrocatalysis, the recombination is paused by applying an external potential greater than the onset potential, which draws out charge carriers from the photoelectrode. N_2 and NO_x^- act as effective feedstock for the production of ammonia. Over the last few years, a diverse class of electrocatalysts has been studied for NH_3 generation. However, many of these electrocatalysts face a significant drawback: they require high overpotential to achieve considerable Faradaic efficiency (FE) for ammonia production. Photoelectrocatalysis can reduce this potential; the photoelectrodes can harness the light energy to generate a photovoltage and compensate for the reducing potential. The reduction potential for NO_3RR is near that of water splitting. Thus, from a thermodynamic viewpoint, the catalysts capable of photoelectrochemical water splitting are also prospective catalysts for NO_3RR. But kinetically, NO_3RR is more challenging and energy demanding as it requires $8e^-$s for complete conversion of NO_3^- to NH_3; otherwise, lower-reduced products like NO_2^-, NO, N_2, and NH_2OH might be formed. Modification of the photocathode with proper catalysts and cocatalysts leads to active NO_3RR and selective production of NH_3. Herein lies the advantages of photoelectrocatalysts. The following subsections will discuss the design of emerging low-dimensional photoelectrocatalysts developed over recent years for ammonia generation (Fig. 17). The design of photoelectrocatalysts generally involves multi-step reactions for heterogenization with multiple-component photocatalysts and electrocatalysts. As the photoelectrocatalysts are composed of photocatalysts and electrocatalysts, the synthetic strategies resemble the photo- and electrocatalysts mentioned in Sections 4 and 5 of this review. The synthesis and modification techniques of some selected photoelectrocatalysts are listed in Table 5.

6.1. 0D photoelectrocatalysts and heterostructures

Photoelectrocatalysts for N_2RR and NO_xRR toward ammonia synthesis encounter similar challenges like photocatalysts and electrocatalysts. The design of stable and selective photoelectrocatalysts for ammonia production using various strategies with improved efficiency is discussed here. Narrow-band gap materials like CuO, Cu_2O, and black P are mostly used for photocathodes.[49,302] Sometimes, photoelectrocatalysts comprise heterostructures of different low-dimensional materials. Plasmonic nanoparticles like Au loaded on 2D WO_3@rGO enhances photoelectrocatalytic performance (Fig. 18A–C).[294] The excellent catalytic properties of $AuWO_3$@rGO for N_2RR are attributed to its electronic conductivity, porous structure,

This journal is © The Royal Society of Chemistry 2025

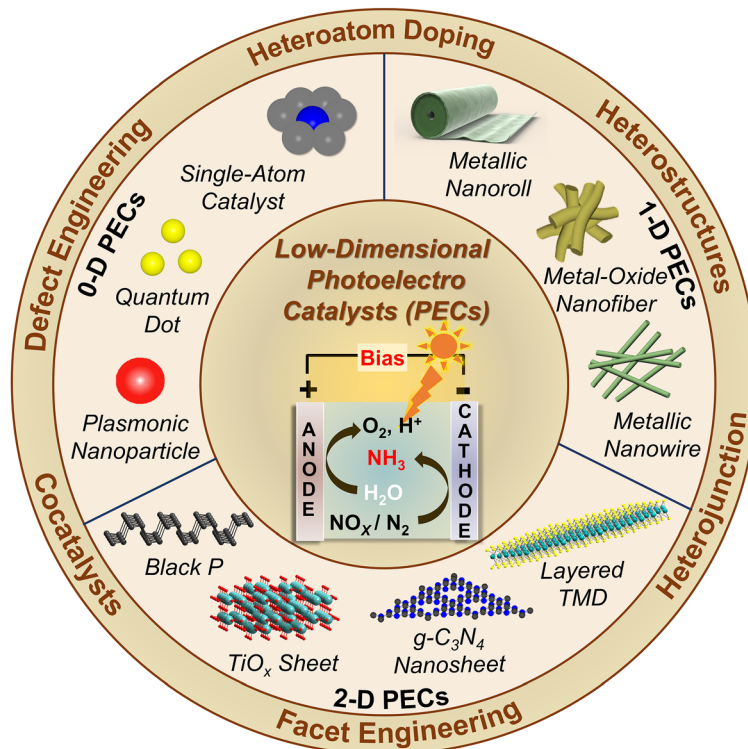Chem. Soc. Rev., 2025, **54**, 5021–5080 | **5057**

Fig. 17 Low-dimensional photoelectrocatalysts (PECs) for ammonia synthesis. Classification of photoelectrocatalysts into 0D, 1D, and 2D, and schematic representations of few selected photoelectrocatalytic LDMs.

Table 5 Synthetic and modification techniques for selected ammonia-generating low-dimensional photoelectrocatalysts

Classification	Materials	Photoelectrocatalysts	Synthesis/Modification	Ref.
0D LDMs and heterostructures	Metallic nanoparticles (NPs)	Au NPs-WS$_2$@RGO	Hydrothermal, microwave methods, chemical reduction	294
		Ag NPs-black Si	Etching, deposition methods	51
		NiO–Au NPs-TiO$_2$	Chemical reduction, thin film preparation, deposition methods	295
	Quantum dots (QDs)	Bi$_2$S$_3$ QDs-MoS$_2$	*In situ* growth of QDs, hydrothermal and solvothermal methods	296
	Single-atoms (SAs)	Ru SAs–Cu$_2$O	SA embedding by simple mixing	181
1D LDMs and heterostructures	Metal and metal oxide-based heterostructures	MoS$_2$ nanoflakes-La$_2$Zr$_2$O$_7$ nanofibers	Electrospinning, hydrothermal methods	87
		Ni–MoS$_2$/Si nanowires	Ni-Doping, metal-assisted chemical etching, hydrothermal, cast-coating methods	88
		Si-α-Fe$_2$O$_3$ nanorods	Hydrothermal, thermal annealing methods	297
		B–Bi nanorolls	B-Doping, chemical reduction	298
2D LDMs and heterostructures	Metal oxide-based heterostructures	TiO$_x$–CdS–Cu$_2$ZnSnS$_4$	Defect engineering of cocatalysts, chemical bath deposition, spray coating	299
	Carbonaceous materials	CoTiO$_3$ nanorods/N-rGO nanosheets	Interface engineering, N-doping, p–n junction, reflux method	300
		CuPc–CeO$_2$	Defect engineering, thin film fabrication, chemical deposition	301

and high surface area. When low-band gap black silicon is integrated with plasmonic silver (Ag) nanoparticles, the hot electron generation and plasmonic resonant energy transfer properties of Ag, combined with the light absorption capabilities of black silicon, significantly enhance photoelectrocatalytic N$_2$RR.[51] The Ag nanoparticles also protect the black silicon from oxidation. The plasmon hot electrons generated from plasmonic Au nanoparticles also activate the NO$_3$RR processes. In a typical NiO/Au plasmon/TiO$_2$ photosystem, NO$_3^-$ are

reduced to ammonia by the plasmon hot electrons at room temperature and neutral pH.[295] These hot electrons also suppress H$_2$ formation and the hot holes are converted to atmospheric O$_2$. The plasmon electrons enhance the electrochemical process by achieving optimal efficiency at lower potentials. The lower working potentials confirm the suppression of competing HER, overcoming one of the major drawbacks of electrocatalytic NO$_3$RR. Quantum dots (QDs) also exhibit excellent photoelectrocatalytic properties, *e.g.*, Bi$_2$S$_3$ QDs grown

5058 | *Chem. Soc. Rev.*, 2025, **54**, 5021–5080
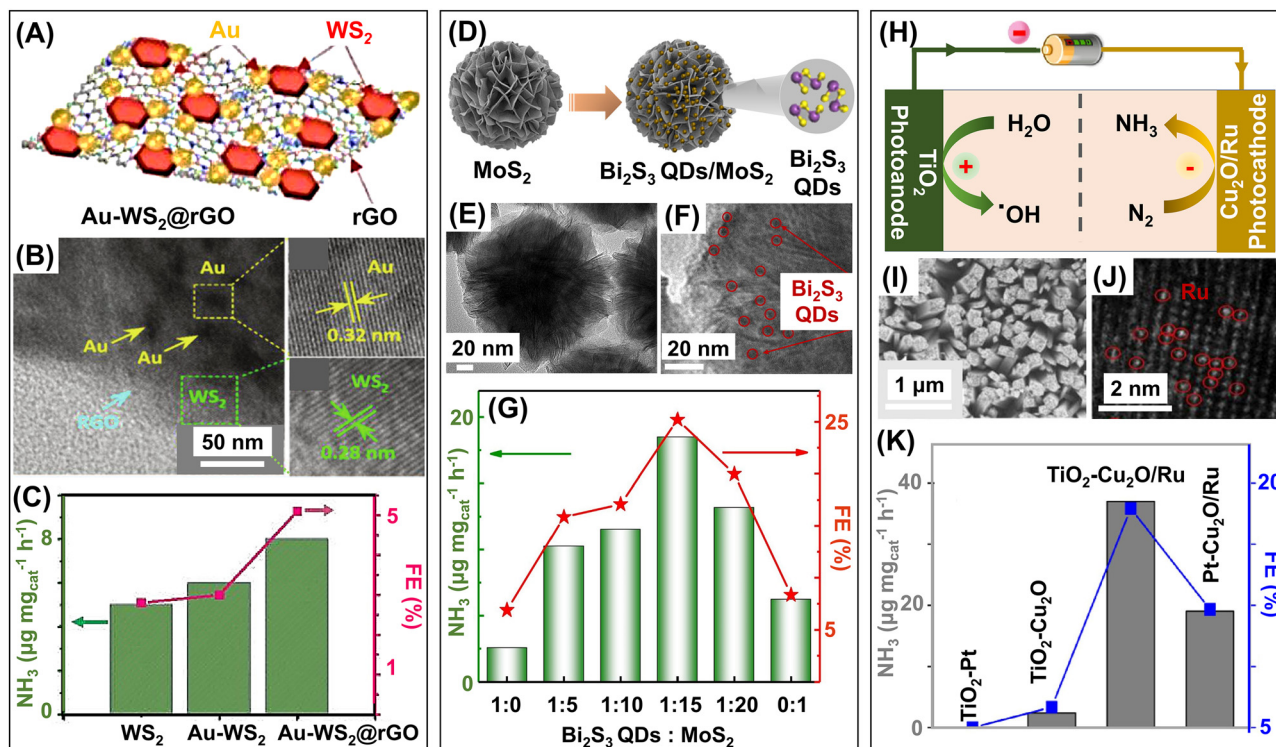
This journal is © The Royal Society of Chemistry 2025

Fig. 18 Zero-dimensional (0D) photoelectrocatalysts for ammonia synthesis. (A) Schematic representation of the 0D plasmonic Au nanoparticles anchored on 2D WS_2@rGO. (B) HRTEM image of Au−WS_2@rGO; zoomed-in images show d-spacing corresponding to (111) and (002) planes of metallic Au and hexagonal phase of WS_2, respectively. (C) NH_3 yields and corresponding Faradaic efficiencies using WS_2, Au−WS_2, and Au−WS_2@rGO at a potential of −0.4 V vs. RHE. Reproduced with permission from ref. 294. Copyright 2023, Elsevier. (D) Schematic representation of Bi_2S_3 quantum dots (QDs) grown over MoS_2 nanoflowers. (E) TEM image of MoS_2 nanoflower. (F) TEM image of Bi_2S_3 QDs marked by red circles, grown over MoS_2. (G) NH_3 yields and the corresponding Faradaic efficiencies using different loadings of Bi_2S_3:MoS_2. Reproduced with permission from ref. 296. Copyright 2022, Elsevier. (H) Schematic representation of the photoelectrochemically driven N_2 reduction to NH_3, where TiO_2 is the photoanode and Ru single-atoms decorated over Cu_2O is the photocathode. (I) SEM image of TiO_2 photoanode. (J) HRTEM image of Cu_2O/Ru photocathode, where the Ru single-atoms are denoted by red circles. (K) NH_3 yields and the corresponding Faradaic efficiencies using different photoelectrocatalysts. Reproduced with permission from ref. 181. Copyright 2022, Elsevier.

in situ over MoS_2 nanoflowers (Fig. 18D–G).[296] Upon photoexcitation with visible light, interfacial charge transfer occurs from the QDs to MoS_2. This process results in the separation of photogenerated charge carriers, leading to a higher concentration of photogenerated electrons on the MoS_2 side. The electron-rich MoS_2 then actively participates in the catalytic reduction of N_2 to NH_3. Single-atoms (SAs) like Ru can also be effective for designing photoelectrocatalysts. Using Ru SAs embedded Cu_2O as photocathode and TiO_2 as photoanode in two-chamber cells can function as a dual system for ammonia synthesis and degradation of bisphenol A (Fig. 18H–K).[181] The electrons supplied by the TiO_2 photoanode can reduce N_2 to NH_3 at the photocathode and, simultaneously, the bisphenol A can be degraded at the photoanode by the $^\bullet$OH radicals. This technique is highly prospective in water treatment and energy generation, and further bifunctional systems like this will be discussed in Section 7.1.

6.2. 1D photoelectrocatalysts and heterostructures

Creating hybrid heterostructures and leveraging the interactions of the components stands out as one of the most effective strategies in photoelectrocatalysis. Incorporating MoS_2 nanoflakes on 1D $La_2Zr_2O_7$ nanofibers creates a heterostructure

that combines their individual properties for effective photoelectrochemical ammonia synthesis.[87] MoS_2 offers the advantages of semiconductors while $La_2Zr_2O_7$ introduces interfacial oxygen vacancies, and the combined effects result in an efficient photocathode. The photogenerated electrons from MoS_2 are transferred to the vacant oxygen sites of $La_2Zr_2O_7$, which participates in N_2 reduction. The use of doped materials is another effective strategy for designing photoelectrocatalysts. Ni-doped MoS_2 coated on silicon nanowires acts as an efficient photocathode for ammonia production in porous water (Fig. 19A–E).[88] Combining two materials with limited catalytic properties into a heterostructure can enhance their catalytic performance by creating a unique interface between the components. Si nanowires and MoS_2 individually exhibit lower conductance. But when MoS_2 is doped with Ni and coupled with Si nanowires to form a heterostructure 1D–2D type electrode, the electron transfer rate is accelerated and so is the efficiency of photoelectrochemical N_2RR. Porous water has a high solubility of N_2, which removes the solubility constraint. MoS_2 and Si nanowires are low-band gap materials that form a type I heterojunction, and doping with Ni provides additional active sites and increases the motility of charge carriers; and all these factors together enhance N_2RR. Doping can also benefit the design of photoanodes. For instance, Mo-doped $BiVO_4$
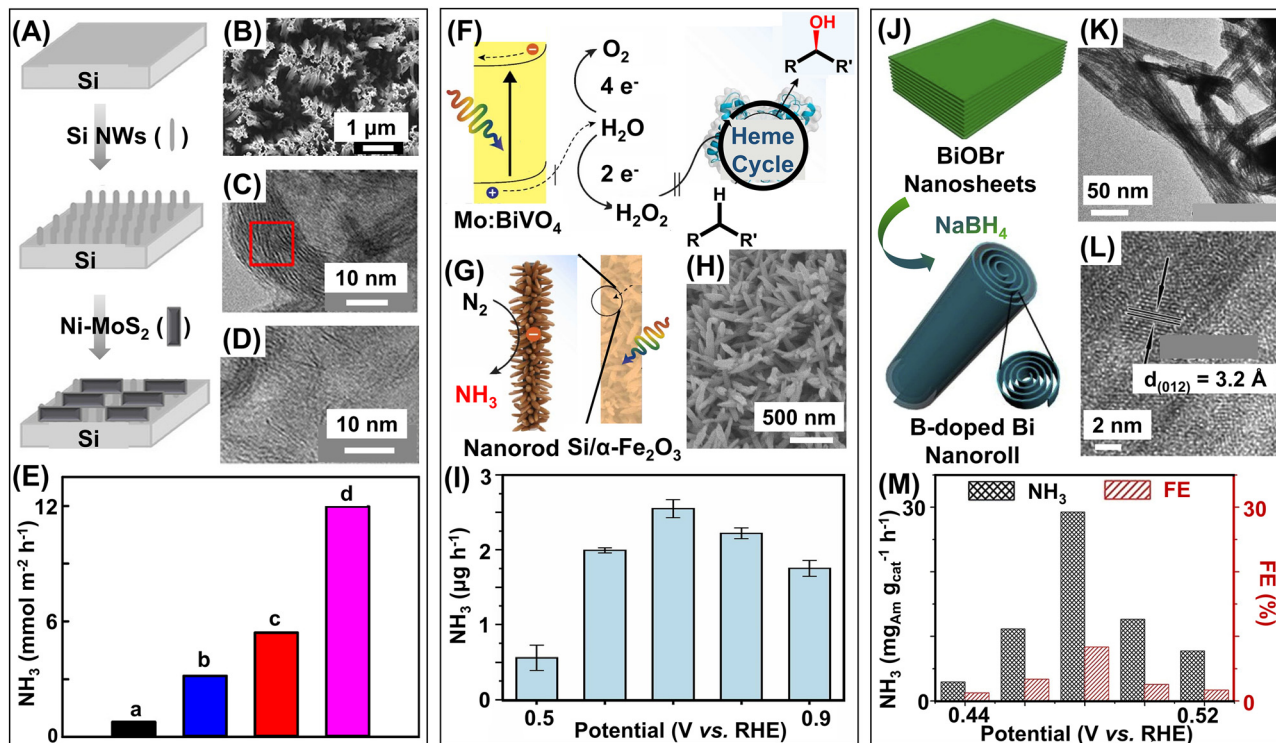
This journal is © The Royal Society of Chemistry 2025

Chem. Soc. Rev., 2025, **54**, 5021–5080 | **5059**

Fig. 19 One-dimensional (1D) photoelectrocatalysts for ammonia synthesis. (A) Schematic representation of the fabrication of Ni-doped MoS_2/Si nanowires (Ni−MoS_2/Si NWs) photocathode. (B) SEM image of 1D Si nanowires. (C) TEM image of MoS_2. (D) TEM image of Ni−MoS_2. (E) NH_3 yields obtained using (a) Si nanowires, (b) MoS_2/Si NW, (c) Ni−MoS_2/Si NW, and (d) Ni−MoS_2/Si NW in porous coordinated polymer (PCP) at a potential of 0.25 V vs. RHE. Reproduced with permission from ref. 88. Copyright 2023, American Chemical Society. (F) Schematic illustration of Mo:$BiVO_4$ photoanode oxidizing H_2O to produce H_2O_2 in situ, which activates peroxygenase for enantioselective oxyfunctionalization reactions. (G) Schematic illustration of Si-wired α-Fe_2O_3 photocathode for paired N_2 reduction to NH_3. (H) SEM image of α-Fe_2O_3. (I) NH_3 yields obtained using the above illustrated photoelectrochemical setup at different potentials. Reproduced with permission from ref. 297. Copyright 2023, Elsevier. (J) Schematic representation of the fabrication of 1D Bi-doped Bi nanorolls from 2D BiOBr nanosheet precursors. (K) TEM image and (L) HRTEM image of B-doped Bi nanorolls. (M) NH_3 yields and corresponding Faradaic efficiencies using B-doped Bi nanorolls. Reproduced with permission from ref. 298. Copyright 2021, Elsevier.

photoanodes can transfer electrons from water to the Si photovoltaic-wired hematite-based photocathode (Fig. 19F–I).[297] Upon irradiation, the photocathodes can reduce N_2 to NH_3. The process is coupled with H_2O_2-dependent oxyfunctionalization, which produces valuable materials simultaneously at the photocathode and photoanode. The doping of B in 1D Bi nanorolls photocathode also facilitates N_2RR by decreasing the energy barrier of the step $N_2 \rightarrow$ *NNH (Fig. 19J–M).[298] The surface curvature of the nanorolls improves the adsorption of N_2. Upon irradiation, the TiO_2 photoanodes supply the necessary photogenerated electrons to the B-doped Bi photocathode N_2RR. Ordered Si nanowires, decorated with Au particles as the designed photocathode material, can operate at positive potential (0.2 V vs. RHE) using solar energy.[85] The hexagonal, ordered nanowire array of p-type semiconductor, Si allows efficient mass transport and reduces the recombination of charges. The Au particles act as the cocatalyst and aid in the selective formation of NH_3 with an FE of 95.6%.

6.3. 2D photoelectrocatalysts and heterostructures

2D black phosphorus (P) nanosheets offer significant properties that are beneficial for N_2RR. Black P is also a direct band gap material with a wide range of light absorption properties. It has abundant surface and edge sites and weak hydrogen

adsorption properties. 2D black P photocathodes can produce N_2 effectively and have excellent stability for up to 12 hours (Fig. 20A–D).[302] The formation of a strong interfacial junction between p-type perovskite oxide $CoTiO_3$ and N-doped reduced graphene oxide (N-rGO) can also optimize N_2RR.[300] The interfacial heterojunction can promote the electron transfer encapsulated between the atomic layers on N-rGO by reducing the diffusion path length and the recombination of charge carriers. Additionally, the heterojunction broadens the wavelength window, enabling more efficient light harvesting. Defects and vacancies also boost the photoelectrocatalytic reactions. In an organic–inorganic hybrid like Cu phthalocyanine (CuPc)/CeO_2 heterostructure, the Ce^{3+}/Ce^{4+} pairs modify the oxygen vacancies, which play a predominant role in the adsorption and activation of nitrates.[301] The 2D macromolecular CuPc has similar properties like p-type semiconductors, which are active under UV-visible light and can efficiently convert solar charge carriers. Also, the d orbitals of Cu match the energy level of LUMO π* of NO_3^-, allowing charge transfer between Cu and NO_3^-. However, CuPc lacks an adequate number of active sites on its surface, necessitating its integration with other catalysts such as CeO_2[301] or $BiVO_4$[303] to perform NO_3RR. CeO_2 has Ce^{3+} and Ce^{4+} oxidation states and abundant oxygen vacancies, which

5060 | Chem. Soc. Rev., 2025, **54**, 5021–5080

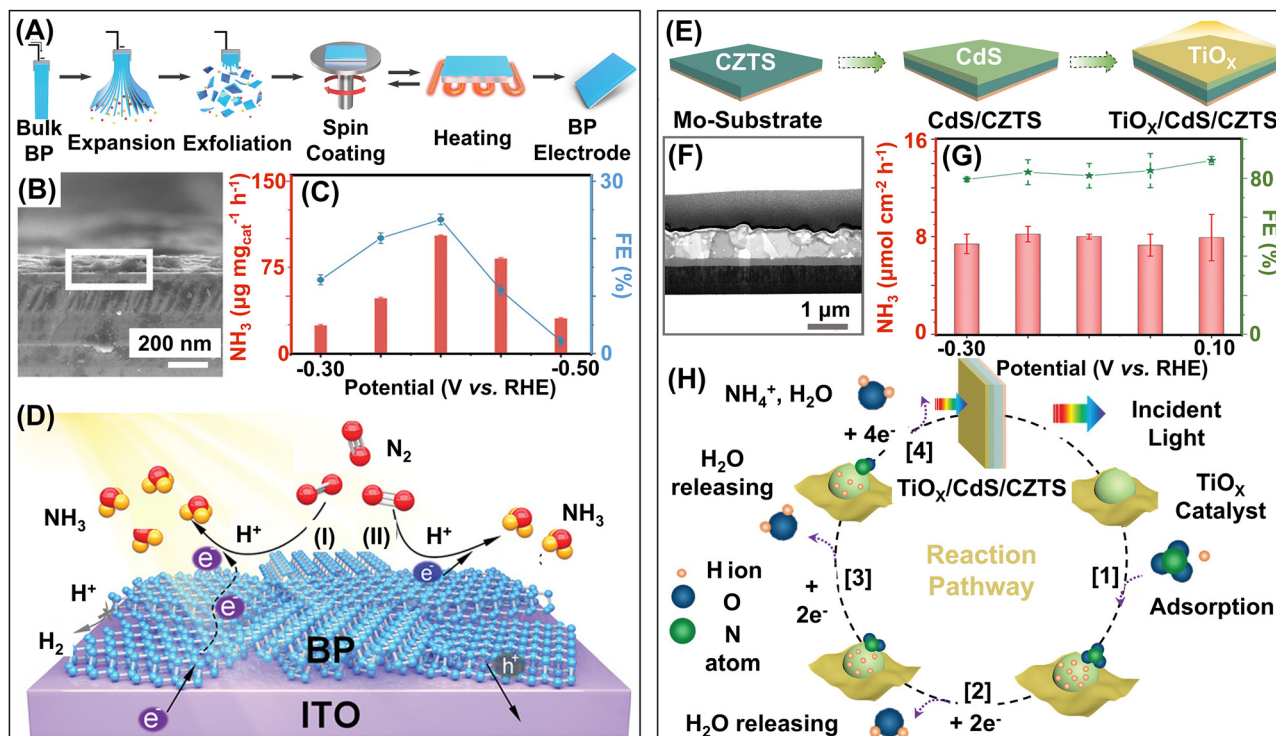This journal is © The Royal Society of Chemistry 2025

Fig. 20 Two-dimensional (2D) photoelectrocatalysts for ammonia synthesis. (A) Schematic representation of the black phosphorus (BP) electrode fabrication using layer-by-layer assembly of exfoliated ultra-thin BP nanosheets. (B) Cross-section SEM image of the fabricated BP electrode. (C) NH_3 yields and the corresponding Faradaic efficiencies using BP electrodes at different potentials. (D) Schematic representation of the photoelectrochemical N_2 reduction to NH_3 by the BP electrodes fabricated on ITO. Reproduced with permission from ref. 302. Copyright 2020, Wiley-VCH. (E) Schematic representation of the step-by-step synthesis of TiO_x/CdS/CZTS electrodes. (F) Cross-section STEM image of TiO_x-250/CdS/CZTS electrodes, synthesized at 250 °C. (G) NH_3 yields and the corresponding Faradaic efficiencies using TiO_x-250/CdS/CZTS electrodes at different potentials. (H) Schematic representation of the mechanism of photoelectrochemical NO_3^- reduction to NH_3 by the TiO_x/CdS/CZTS electrodes. Reproduced with permission from ref. 299. Copyright 2022, Wiley-VCH.

can entrap photogenerated charge carriers and facilitate the adsorption of nitrates. $BiVO_4$ is a p-type semiconductor with a large band gap, which limits its photocatalytic performance, and coupling with CuPc makes $BiVO_4$/CuPc an effective catalyst. Defect-engineered materials like TiO_x with oxygen vacancies (V_Os) are effective cocatalysts for NO_3RR. For the construction of the photocathode, a p–n junction is fabricated by coating Cu_2ZnSn_4 with the CdS layer (Fig. 20E–H).[299] Cu_2ZnSn_4 has excellent light harvesting properties, and CdS has efficient charge separation properties. TiO_x cocatalyst with Ti^{3+}/V_O sites allows better adsorption of NO_3^- and $*NO_2$ intermediate on the photocathode. The efficient electron transfer reduces the work function and extends the carrier lifetime, which results in an FE of 89.1% for ammonia at 0.1 V *vs.* RHE. The benefit of the photoelectrochemical strategies mentioned above is that they couple photocatalysis and electrocatalysis, and the synergistic effect can enhance the charge separation, reduction capability of electrons, equilibrium of electron distribution, and also reduce the probability of oxidation of ammonia produced.[304]

7. Applications

Besides ammonia production by NO_xRR and N_2RR, these reactions are also important in many aspects. For instance, nitrates

and nitrites are common pollutants found in wastewater and their reduction can help in environmental remediation. NO_xRR and N_2RR, when coupled with CO_2RR, C–N coupling can favour the formation of urea. Various relevant and important oxidation reactions can be coupled with these reduction reactions. All these aspects are highlighted in the following sections.

7.1. Water purification

Nitrates and nitrites, the precursors of ammonia synthesis, are common sources of pollutants in surface and groundwater. Hence, wastewater containing nitrates and nitrites can act as N-feedstock for ammonia production, helping in wastewater treatment and producing sustainable energy resources. The major sources of nitrate contamination in water originate from fertilizers used in agriculture, industrial waste (including ammonia-producing industries using the Haber–Bosch process), stormwater runoff from metropolitan areas, and sewage water. The concentration of nitrates in wastewater depends on the source of pollution: 1.95 M in low-level nuclear wastewater, 41.6 mM in industrial wastewater, and 7.4 mM in textile wastewater.[305] Nitrates can lead to eutrophication and nitrites produced from the reduction of nitrates pose serious health risks to humans and the animal kingdom. Nitrates and their metabolites can also cause blue baby syndrome, hypertension,
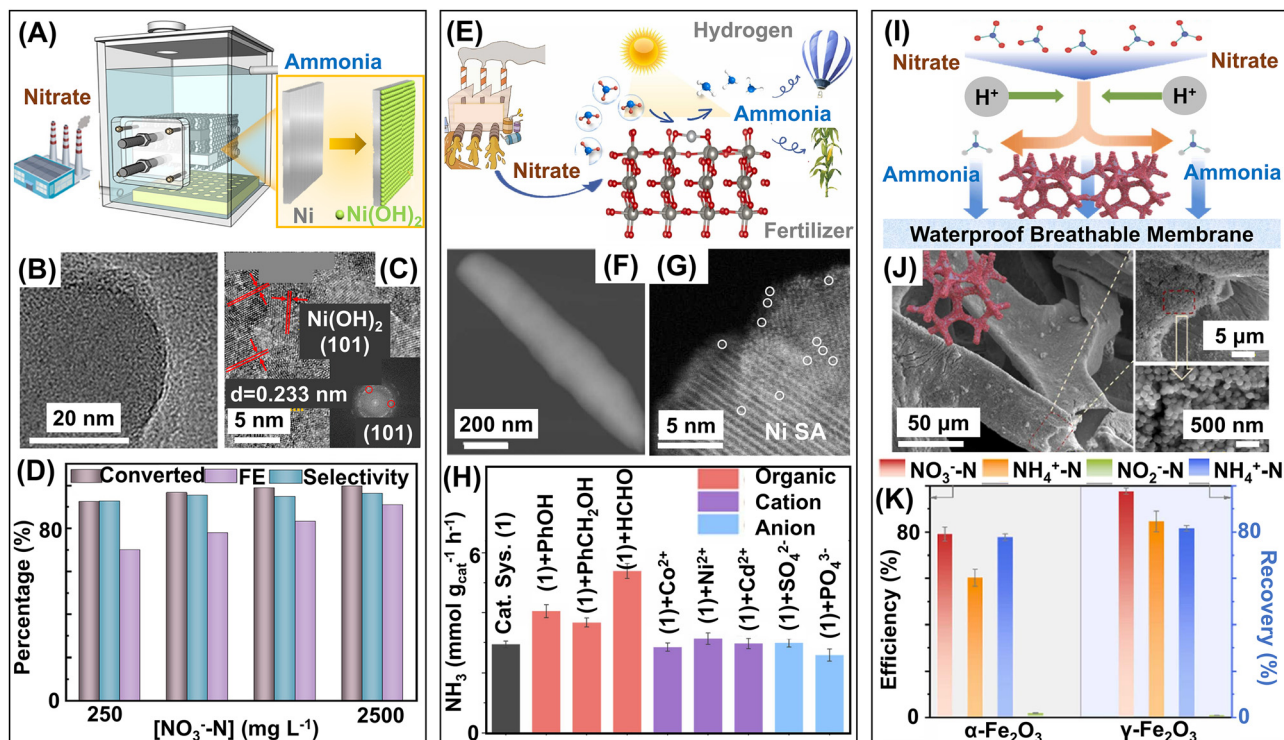
This journal is © The Royal Society of Chemistry 2025

Chem. Soc. Rev., 2025, **54**, 5021–5080 | **5061**

Fig. 21 Low-dimensional catalysts for ammonia synthesis coupled with water purification. (A) Schematic representation of electrochemical reactor for wastewater purification containing NO_3^- using self-activated 0D $Ni(OH)_2$ particles formed on Ni substrate, $Ni(OH)_2$@Ni cathode. (B) TEM image of $Ni(OH)_2$@Ni cathode. (C) HRTEM image of the $Ni(OH)_2$@Ni cathode showing the lattice fringes with d-spacing of 0.233 nm and FFT (inset) corresponding to the (101) plane of $Ni(OH)_2$. (D) Effects of NO_3^--N concentration on the conversion efficiency, Faradaic efficiency of NO_3^- reduction, and NH_4^+–N selectivity under the fed-batch conditions. Reproduced with permission from ref. 312. Copyright 2021, American Chemical Society. (E) Schematic representation of the photocatalytic synthesis of value-added ammonia from nitrate-containing wastewater using Ni single-atoms-decorated defective WO_3. (F) SEM image of Ni/H_xWO_{3-y} catalyst. (G) HRTEM image showing the Ni single-atoms marked by white circles. (H) NH_3 yields using Ni/H_xWO_{3-y} catalyst and upon addition of different organic, cationic, and anionic pollutants. Reproduced with permission from ref. 41. Copyright 2024, Elsevier. (I) Schematic representation of the electrochemical NO_3^- to NH_4^+ by natural hematite electrode. (J) SEM image of α-Fe_2O_3 deposited on Ni foam at different magnifications. (K) Comparative study of NO_3^- removal, NO_2^- selectivity, NH_4^+ selectivity, and recovery of α-Fe_2O_3 and γ-Fe_2O_3. Reproduced with permission from ref. 314. Copyright 2024, Elsevier.

and cancers. Hence, the U.S. Environmental Protection Agency has set a limit of 10 mg L^{-1} of N–NO_3^- and 1 mg L^{-1} of N–NO_2^- in drinking water.[306] Conventional denitrification approaches reduce nitrates present in water to gaseous nitrogen, avoiding side products like nitrous oxide or ammonia.[307–310] However, recent progress in this aspect highlights the benefits of the reduction of nitrates to ammonia as an important precursor to different value-added products, *e.g.*, fertilizer and a prospective hydrogen storage fuel.[311] Here, we will discuss a few state-of-the-art catalytic materials to demonstrate the feasibility of the process.

7.1.1. 0D nanostructured and heterostructured catalysts. Self-activated 0D $Ni(OH)_2$ nanoparticles deposited on Ni substrate can selectively reduce NO_3^- to NH_4^+ in the laboratory as well as can be scaled up to treat wastewater from a chemical factory, Hunan Sinopec Catalyst Co., Ltd (China) (Fig. 21A–D).[312] The pilot-scale wastewater treatment system reported in this work consists of a sedimentation tank, electrocatalytic reactor, and storage tank. A sedimentation tank is used to separate the solids suspended in wastewater. The electrocatalytic reactor is set up with 26 electrodes connected to a DC

power supply and can purify 500 liters of wastewater. The reactor can work in fed-batch and continuous flow modes for NO_3^-–N concentration 241–2527 mg L^{-1}, and the selectivity of NH_4^+–N obtained is as high as 92.5%. The reduced ammonia can be separated from water using air-stripping methods. Photoelectrocatalytic 0D Co can also produce ammonia in simulated wastewater containing nitrates, nitrites, phosphates, sulfates, carbonates, and bicarbonates.[313] However, the FE for ammonia in simulated wastewater is only 12%, whereas the maximum FE reported is 92% in water containing only NO_3^-. Ni single-atoms decorated on oxygen-vacant WO_3 can efficiently produce ammonia in simulated wastewater containing NO_3^- and other organic pollutants like phenol, benzyl alcohol, and formaldehyde (Fig. 21E–H).[41] These organic pollutants act as hole-sacrificial agents and promote NO_3^- reduction. Subnanometric metal oxides on TiO_2 can also function as efficient photocatalysts for ammonia production in simulated wastewater.[154] CuO nanoparticles on Cu foam electrodes can directly produce ammonium-based fertilizer when simulated wastewater containing NO_3^- and Cl$^-$ is fed into the constructed flow cell containing cathodic and anodic reaction chambers, an

5062 | *Chem. Soc. Rev.*, 2025, **54**, 5021–5080

This journal is © The Royal Society of Chemistry 2025

electrified PTFE membrane, and a trap chamber.[53] The performance of the electrochemical flow cell has also been monitored using industrial wastewater from Shandong Keyuan Pharmaceutical Co. Ltd, containing NO_3^-, Cl^-, Na^+, K^+, SO_4^{2-}, and chemical oxygen demand (COD). Production of $(NH_4)_2SO_4$ from industrial wastewater is a proof-of-concept for electrochemical upcycling of NO_3^- to form valuable fertilizers.

7.1.2. 1D nanostructured and heterostructured catalysts.
Ru–Cu nanowire catalysts can reduce the nitrate concentration in water from an industrial level of 2000 ppm to a drinkable level of <50 ppm and efficiently produce ammonia.[208] For separating ammonia, effluent with a high vapour pressure of ammonia is subjected to air stripping, and 99.7% of ammonia is successfully stripped out. For air stripping, in this work, the effluent is sealed in a flask with Argon for 24 hours. This stripped-out ammonia vapour is either trapped in HCl to form NH_4Cl or condensed to form ammonia water. The performance of catalytic materials for NO_3RR to NH_3 has also been demonstrated in simulated wastewater to extend the practical applicability. In another work published by the same group, similar Ru–Cu nanowires with slight modifications have been utilized for electrocatalytic NO_3RR from industrial wastewater containing 2000 ppm NO_3^-.[315] In this work, they have developed a membrane electrode assembly (MEA) and a reactor with a porous solid electrolyte (PSE) and compared their electrocatalytic NO_3RR performance. The PSE reactor, which has a cation shielding effect, is more effective due to enhanced concentration of cations, and can produce purified water and ammonia simultaneously from electrocatalytic NO_3RR. Another work highlights the fabrication of a paired electrolysis platform, where defect-engineered 1D TiO_2 nanotubes with Co doping and oxygen vacancies act as the cathode.[316] The doped and vacant sites can synergistically promote electron transfer for NO_3RR to NH_3 at the cathode, and the anode simultaneously traps the NH_3 and converts it to $(NH_4)_2SO_4$, an ammonia-based fertilizer used in agriculture.

7.1.3. 2D nanostructured and heterostructured catalysts.
The recovery of produced ammonia from wastewater is always challenging. A few works focused on this challenge and developed electrodes based on 2D materials to address this problem. In this attempt, a membrane-less electrochemical technique has been developed that electrochemically converts nitrate synchronized with ammonia recovery.[317] The system typically consists of a 3D-printed porous Cu–Ni metallic glass that can effectively electroreduce the nitrates present in wastewater to ammonia. This work successfully converts 70% of nitrate and recovers the ammonia from the reaction mixture as ammonium chloride. Hematite (α-Fe_2O_3) deposited on a Ni foam electrode and coupled with a water-resistant membrane can reportedly remove 97.6% of nitrates from wastewater, and consequent upcycling of these nitrates can yield ammonia (Fig. 21I–K).[314] 81.6% of this ammonia can be recovered in situ in the form of ammonium sulfates. To check practical applicability, the system is tested on wastewater from a photovoltaics industry containing nitrates and nitrites. After electrocatalysis, 74.8% of total inorganic nitrogen is removed and 77.1% of

ammonium is recovered. The entire process leads to an energy consumption rate of 62.2 kW h per kg of NH_3.

7.2. Urea synthesis

Urea is the most important nitrogen-based fertilizer used in crop production. The current industrial process for urea synthesis uses harsh reaction conditions and leaves a huge carbon footprint. This includes (i) the synthesis of ammonia by the Haber–Bosch process and (ii) the combination of ammonia and CO_2 at a high temperature (150–200 °C) and pressure (150–200 bar).[318] Hence, a ''greener'' and more sustainable way to produce ammonia under ambient conditions is required, which would also aid in realizing carbon/nitrogen neutrality in the environment. Co-reduction of CO_2 and nitrogenous species like NO_3^-, NO_2^-, and N_2 via electrochemical or photoelectrochemical pathways can lead to the sustainable production of urea by C–N coupling, thus maintaining carbon neutrality and the nitrogen cycle.[318,319] However, slow adsorption of substrates, multiple reaction steps, and competitive side reactions impede the catalytic reactions toward urea synthesis.[320] Hence, to improve catalytic processes, the design of catalysts is crucial for the co-reduction process. A diverse range of catalysts, such as single-atoms, bimetallic, dual site, oxygen-vacant, and non-metallic materials, have been used in recent years for the co-reduction of nitrogenous species and CO_2 to form urea.

7.2.1. 0D nanostructured and heterostructured catalysts.
Cu single-atoms with different coordination environments have been widely used for urea production. A comparative study with Cu–N–C coordination structures revealed that Cu–N_4 and Cu–N_{4-x}–C_x are more active sites for NO_3RR and CO_2RR when compared to Cu–N_3–C_1 and Cu–N_2–C_2.[321] The formation of *COOH and *NH intermediates are energetically more favourable on Cu–N_4 sites while the energies of other intermediates like *CO and *NH_2 are similar on all Cu–N–C sites. Cu single-atoms (SAs) can be electrochemically reconstituted to form Cu_4 clusters that act as active sites for C–N coupling and urea synthesis.[58] The Cu_4 clusters can be reversibly transformed to Cu SAs again by switching to open circuit potential and this makes the Cu_1–CeO_2 catalysts structurally and electrochemically stable. Cu SAs can also be used to form bimetallic sites Cu/Ti by coupling with TiO_2.[322] The benefit of using bimetallic sites is that the Cu site can effectively adsorb CO_2 and reduce *CO_2 to *CO; while the Ti sites can adsorb NO_3^- and reduce *NO_3^- to *NH_2 by photoelectrocatalysis. Due to the adjacent positioning of Cu and Ti, the *CO and *NH_2 intermediates can easily undergo C–N coupling to form urea. Bimetallic Cu/Zn sites can operate by relay catalysis mechanism and stabilize the intermediates *CO_2NO_2 (key intermediate for C–N coupling) on Zn sites and *$COOHNH_2$ (formed on protonation) on Cu sites preferentially.[323] Urea formation with an FE of 75% is reported for wastewater-level nitrate concentrations. 0.28 kg of CO_2 emissions per kg of urea is calculated for the Cu/Zn catalyst, which is far less compared to 1.8 kg of CO_2 for conventional methods of urea synthesis. The study also compares the urea formation for bimetallic hybrid catalysts and

This journal is © The Royal Society of Chemistry 2025

Chem. Soc. Rev., 2025, 54, 5021–5080 | 5063

their corresponding single-component catalysts. The reaction energy for C–N bond formation and the consecutive protonation step is higher for single-component catalysts, which leads to lower FE for urea. Electrocatalysts like CuWO$_4$ are also endowed with bimetallic sites that combine the advantages of WO$_3$ and CuO$_x$, and are capable of simultaneous reduction of NO$_3^-$ and CO$_2$.[59] The high-valence W centers in WO$_3$ can stabilize *NO$_2$ intermediates, however, they are unable to reduce CO$_2$ to *CO at low overpotentials. Contrarily, Cu centers are well known for reducing CO$_2$ to *CO, but a continuous arrangement of Cu assists in C–C coupling reactions, forming a series of by-products. For the formation of urea, C–C coupling has to be suppressed, and C–N coupling reactions have to be promoted, which is achieved by CuWO$_4$. The alternating bimetallic reduction sites, Cu and W, can reduce the raw precursors, form reduced and hydrogenated intermediates, initiate C–N coupling, and increase the selectivity of urea produced. Besides the Cu and bimetallic catalysts, other single metallic catalysts based on Fe and Pt can also produce urea. In one such work, the utilization of 0D Fe$_2$O$_3$ nanoparticles has been highlighted for urea synthesis from the co-reduction of NO$_3^-$ and CO$_2$ simultaneously.[324] Here, minuscule γ-Fe$_2$O$_3$ nanoparticles (<2 nm), confined within the pores of a conductive metal–organic framework (MOF), Ni-HITP MOF can electrocatalytically produce urea, and the catalyst shows stability for 150 hours. Instead of having excellent catalytic properties, metal oxide nanoparticles suffer from a few drawbacks like instability, aggregation, and uneven size distribution. Encapsulation within the pores of Ni-HITP MOF offers better stability, uniform size, confinement, and conductivity to the γ-Fe$_2$O$_3$ nanoparticles for electrocatalysis. The Fe(III) centers can simultaneously reduce NO$_3^-$ and CO$_2$ to *NO$_2$ and *COOH, the key intermediates. Further, these catalytically active adjacent Fe(III) centers can induce C–N coupling between *NH$_2$ and *COOH to produce *CONH$_2$, the key intermediate for urea formation. Pt nanostructures can also produce urea electrocatalytically from CO and NH$_3$.[325] In this work, CO has been used instead of CO$_2$. In the first step, Pt triggers the oxidative coupling between CO and NH$_3$ to produce cyanate via proton-coupled electron transfer. In the next step, the produced cyanate reacts with ammonium via the Wöhler reaction to yield urea, the desired product. The reactions take place on the exposed Pt(100) and Pt(111) facets of the Pt/C catalyst. Oxidation of NH$_3$ and CO are energetically feasible on both Pt(111) and Pt(100) surfaces. However, the *NH$_3$ intermediate is more stable on Pt(111) while the *NH$_2$ intermediate is more stable on Pt(100) facet. Among the intermediates obtained from CO oxidation, *CO is stable on Pt(100); however, *CO$_2$ and *COOH are unstable and react with OH$^-$ to form CO$_2$ and H$_2$CO$_3$, respectively. Hence, on the Pt(100) surface, *NH$_2$ and CO undergo C–N coupling to produce *OCNH, which is converted to *OCN (cyanate) under alkaline conditions. In the presence of NH$_4^+$, this cyanate is converted to urea.

7.2.2. 1D nanostructured and heterostructured catalysts.
Instead of single components, hybrid bimetallic catalysts can lower the energy barrier and selectively produce urea in higher amounts. Dual-active Fe sites, namely, amorphous Fe, and

Fe$_3$O$_4$ on carbon nanotubes (CNTs), also act as efficient electrocatalysts for urea production (Fig. 22A–D).[60] The amorphous Fe@C and Fe$_3$O$_4$ active sites participate in the adsorption and activation of NO$_3^-$ and CO$_2$, respectively, and lower the energy barrier for the formation of urea. Zn foil is an efficient electrode for the electrosynthesis of urea, but the fabrication of Zn nanostructures via typical methods is challenging. Coupling Cu with Zn to form a bimetallic core–shell nanowire structure is a viable alternative (Fig. 22E–H).[326] Additionally, electron transfer from Zn to Cu produces electron-deficient Zn, which favours NO$_3$RR. The Cu@Zn bimetallic heterostructure thus favours the formation of intermediates and the C–N coupling required for urea synthesis. Non-metallic catalysts like F-doped carbon nanotubes (CNTs) also report excellent urea production by electroreduction of CO$_2$ and NO$_3^-$.[327] The availability of abundant C–F$_2$ moieties as active sites promotes the formation of *CO and *NH$_2$ intermediates, and the electronic structure of CNTs ensures excellent conductivity and charge transfer, beneficial for electrocatalysis. Another recent work reports 1D Cu phthalocyanine nanotubes, which have many active sites for electroreduction, namely, Cu center, pyridinic-N1, and pyrrolic-N2 and N3.[328] Among them, urea synthesis is driven by the reduction of N$_2$ and CO$_2$ by dual active sites, the pyridinic-N1 site and Cu site to form *NN and *CO, respectively. Here also, the reaction proceeds through the *NCON intermediate, followed by subsequent protonation to form urea. The catalyst surface is modified via oxygen vacancy and facet engineering to boost the catalytic synthesis of urea. For the formation of urea, the C–N coupling reaction between *CO$_2$ and *NO$_2$ intermediates is crucial. The early-stage C–N coupling provides a better selectivity of urea when compared to the later-stage coupling between *CO$_2$ and *NH$_2$.[329] For instance, defect-engineered 1D CeO$_2$ nanorods with abundant oxygen vacancies can entrap and insert *NO intermediate into the vacant sites and subject it to subsequent C–N coupling to form *NO–CO.[330] The oxygen-vacant (V$_O$) CeO$_2$ nanorod catalysts were compared with the V$_O$-deficient CeO$_2$ catalysts to gain conducive insight into the *NO entrapping by the V$_O$ sites. Further, this work indicates that the C–N coupled intermediate formation has a lower energy barrier when compared to the protonation intermediates in the case of pristine CeO$_2$. The oxygen vacancies can thus help in selective C–N coupling and promote the electrocatalytic synthesis of urea. The C–N coupling step promotes the selectivity of the formation of urea, however, the energy barrier of the protonation of *CO$_2$NH$_2$ is high, which is why it is the potential determining step (PDS). The energy barrier of PDS can be reduced by 1D indium oxyhydroxide, i.e., InOOH rods with oxygen vacancies.[57] The oxygen vacancies result in unsaturated In sites, which decrease the energy barrier of PDS, facilitate the protonation of *CO$_2$NH$_2$ to *COOHNH$_2$, and enhance the catalytic performance of InOOH for producing urea. The catalysts discussed above operate on the co-reduction of NO$_3^-$ and CO$_2$ precursors to form urea. Though nitrates are readily available and have more advantages, some catalysts also report urea synthesis by N$_2$ and CO$_2$ co-reduction. Mott–Schottky heterostructures like Bi–BiVO$_4$ have a space–charge region at

5064 | Chem. Soc. Rev., 2025, 54, 5021–5080

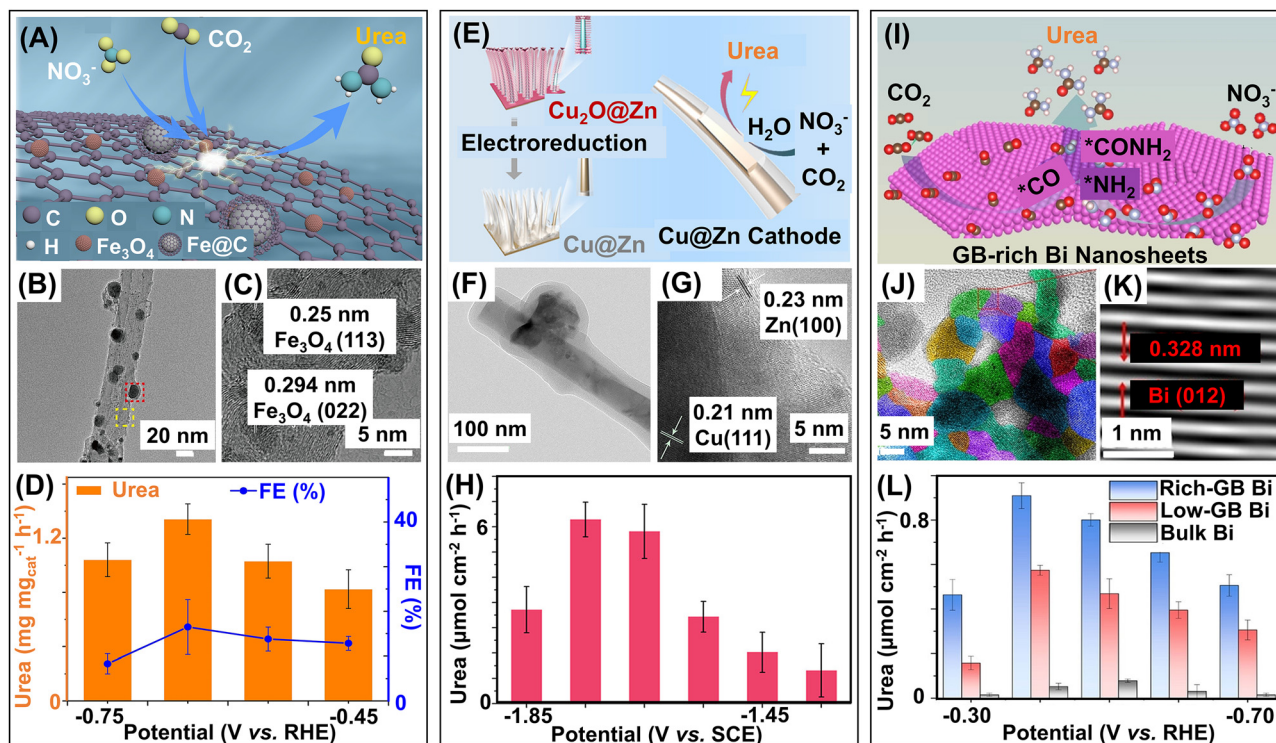This journal is © The Royal Society of Chemistry 2025

Fig. 22 Low-dimensional catalysts for urea synthesis from co-reduction of NO_3^- and CO_2. (A) Schematic representation of urea synthesis by dual active Fe(a)@C and Fe_3O_4 on carbon nanotubes (CNTs). (B) TEM image of Fe(a)@C-Fe_3O_4/CNT. (C) HRTEM image showing the lattice fringes with d-spacings of 0.25 nm and 0.294 nm corresponding to the (113) and (022) planes of Fe_3O_4 nanoparticles, respectively. (D) Urea yields and the corresponding Faradaic efficiencies using Fe(a)@C-Fe_3O_4/CNT at different potentials. Reproduced with permission from ref. 60. Copyright 2023, Wiley-VCH. (E) Schematic representation of the fabrication of core–shell Cu@Zn nanowires and catalytic formation of urea over these nanowires. (F) TEM image of Cu@Zn nanowire. (G) HRTEM image showing the lattice fringes with d-spacings of 0.23 nm and 0.21 nm corresponding to the Zn(100) and Cu(111) planes, respectively. (H) Urea yields at different applied potentials using the Cu@Zn nanowires. Reproduced with permission from ref. 326. Copyright 2022, American Chemical Society. (I) Schematic representation of grain boundary-rich Bi nanosheets reconstructed from Bi_2Se_3 nanosheets, utilized for the synthesis of urea from NO_3^- and CO_2. (J) TEM and (K) HRTEM images of grain boundary-rich Bi nanosheets showing lattice fringes with d-spacing of 0.328 nm corresponding to the (012) plane of Bi. (L) Comparison of urea yields by grain boundary-rich Bi, low grain boundary Bi, and bulk Bi at different applied potentials. Reproduced with permission from ref. 332. Copyright 2024, Wiley-VCH.

the interface due to the transfer of electrons from $BiVO_4$ to metallic Bi, forming local electrophilic and nucleophilic regions.[331] The space–charge region exposes more active sites and promotes adsorption and activation of N_2 and CO_2 at local electrophilic and nucleophilic sites, respectively. Thereafter, the C–N coupling between *N≡N* and CO produces the *NCON* intermediate, which acts as a precursor for the formation of urea.

7.2.3. 2D nanostructured and heterostructured catalysts. 2D catalysts like MXenes, MBenes, and carbon nitrides are well-known catalysts discussed previously in Section 5.2 for electro-catalytic ammonia synthesis. Recent studies indicate that besides reducing N_2 or NO_3^-, the heterostructures based on these 2D materials can co-reduce CO_2 and function as efficient electrocatalysts for urea synthesis. One of the recent works along this line reports a double transition metal-based Mo_2VC_2 MXene, which can co-reduce N_2 and CO_2 and, followed by C–N coupling, can produce urea.[333] The selective formation of key intermediates for the C–N coupling is crucial for urea production. The Mo_2VC_2 MXene can selectively convert *CO_2 to *CO, which is one of the key intermediates. This *CO can further react with the intermediates formed from N_2, *i.e.*, *N_2 and

H-added intermediates like *NHN, *NHNH, *NH_2N, *NH_2NH, and *NH_2NH_2, *via* C–N coupling to produce urea. The work also highlights that double-transition metal-based MXenes can effectively function as better electrocatalysts for urea synthesis when compared with single-transition metal-based MXenes. Hence, single-transition metal-based MXenes like Mo_2C can also be functionalized with planar metal clusters like Cu *via* strong metal–support interactions for enhanced performance of urea electrosynthesis.[334] The active sites on the Cu_n/Mo_2C catalyst enhance the electrocatalytic "one-step" N–C–N coupling process by inserting *CO intermediate into the NH_2*–NH_2* intermediate, promoted by the electrostatic interactions between the N atoms. This "one-step" coupling process offers an energy-efficient and favourable thermodynamic route to urea synthesis compared to the conventional two-step coupling processes. Bimetallic sites like Ru–Pd can also promote the photoelectrosynthesis of urea when encapsulated on 2D–2D heterostructures like WO_3/MXene.[335] The photo-cathode composed of this 0D–2D–2D heterostructure can simultaneously reduce CO_2 and N_2 and is substantiated by water oxidation at the photoanode. However, the fabrication

This journal is © The Royal Society of Chemistry 2025

Chem. Soc. Rev., 2025, **54**, 5021–5080 | **5065**

and engineering of this multi-component catalyst are complex and costly, and the design of simpler and cheaper photo- or electrocatalysts is more favourable for a better understanding of the catalytic mechanism over active sites. Another work reports the utilization of 2D MBenes to electrosynthesize urea from N_2 and CO_2 under ambient conditions.[336] The MBenes with three different metal centers have been used here, namely, Ti_2B_2, Mo_2B_2, and Cr_2B_2. Electrocatalytic urea synthesis takes place at the basal planes of the MBenes. These MBenes can also suppress competitive N_2 reduction to NH_3. Among the three MBenes, the surfaces of Mo_2B_2 and Cr_2B_2 are resistant to oxidation and degradation and offer more reactive surface area, activity, and selectivity for electrocatalysis. Porous carbon nitrides are also another class of widely explored 2D electrocatalysts. These carbon nitrides can also electrosynthesize urea upon structure modification like doping and embedding metallic sites. In this approach, a new N_4B_4 porous carbon nitride with B doping has been synthesized.[337] Upon further substitution doping, M_2B_2 structures have been formed. Fourteen metal (M) atoms have been used and, among them, M = Mn, Cr, and Os were found to be the most active for urea synthesis. The –C–N–C linkages in the carbon nitrides increase the surface area of the pores, which provides more area for electrocatalytic reactive sites. Metal doping increases the conductivity of the catalysts. The boron–boron, metal–boron, and metal–metal bidentate sites enhance the electrocatalytic performance. However, the B–Mn site provides the maximum activation effect on N_2, proving B_2Mn_2 to be the best-performing carbon nitride catalyst in this work. Doping of Fe atoms on InOOH nanosheets has also shown an effective increase in the rate of urea production as compared to bare InOOH nanosheets.[338] The studies indicate that Fe doping increases the number of active sites and optimizes the electronic structure for the adsorption, activation, and hydrogenation of the *$CONH_2$ key intermediate, thereby enhancing the C–N coupling reaction for urea formation. As discussed previously, the catalyst surface plays a crucial role in the adsorption of substrates, the generation of active species, and, finally, releasing the catalytic products for any catalytic reaction. From this viewpoint, 2D catalysts with more active sites can be engineered from exfoliation of existing 2D materials, aiming toward better catalytic performance. Consequently, the reconstruction of Bi_2Se_3 nanosheets into 2D bismuth (Bi) nanosheets results in a high density of grain boundaries caused by the presence of defects (Fig. 22I–L).[332] The urea yield for the reconstructed Bi nanosheets is eight times that of the Bi_2Se_3 nanosheets. This enhancement in catalytic activity is because the grain boundaries lower the energy barriers for the formation of the key intermediates *CO and *NH_2, and also for the C–N coupling reaction. Hence, it can be said that tuning the structures of low-dimensional materials is always crucial from the aspect of catalysis for obtaining maximum catalytic activity.

7.3. Coupled oxidation reactions

An overall reaction consists of an oxidation half-reaction and a reduction half-reaction. Generally, the reduction reactions of N_2 and NO_x^- are accompanied by water-splitting, leading to oxygen evolution reaction (OER), and the formation of active hydrogen.[339–341] The active hydrogen produced from water splitting helps in the protonation process and promotes the formation of ammonia. However, the active hydrogen (H*) produced should be consumed immediately by the nitrogen intermediates, which is difficult as the interaction between two H* forms H_2, giving rise to competitive HER. The active H* can be successfully utilized by catalysts, such as $Co(OH)_2$ and CoP, where the water dissociation process is facilitated on the Co catalysts' surface.[342,343] However, the OER reaction is sluggish and has a high thermodynamic potential of 1.23 V vs. RHE. As an outcome, this hampers the N_2RR and NO_xRR and slows down the entire redox process. Hence, efforts have been made to replace the OER with lower-potential oxidation reactions, like the oxidation of urea, hydrazine, methanol, ethanol, benzyl alcohol, glycerol, and PET, which can yield some value-added products. This section will explore different low-dimensional catalysts, focusing on this approach.

7.3.1. 0D nanostructured and heterostructured catalysts.
Quantum dots (QDs) with semiconducting properties have tuneable band gaps and thus act as excellent catalysts for multielectron and multiproton processes.[344,345] Upon light irradiation, QDs produce sufficient electrons and protons to perform the $8e^-$ NO_3^- reduction to NH_3 as well as any coupled oxidation simultaneously. One such photocatalytic system, glutathione (GSH)-capped 0D CdSe QDs, can convert NO_3^- to NH_4^+ in the presence of an LED light of wavelength 440 nm.[346] Under this light irradiation, H• and GS• radicals are generated from glutathione. The H• radicals participate in the formation of the N–H bond of NH_4^+. The GS• radicals provide the holes for value-added oxidative transformation of secondary aryl alcohols to the corresponding ketones. Bifunctional catalysts also play an immense role in coupling oxidation and reduction reactions in an electrochemical cell. One such example of 0D bifunctional catalysts is $CuCo_2O_4$ spinel oxide-based nanoparticles.[347] $CuCo_2O_4$ nanoparticles, embedded on porous carbon fiber support, can electrocatalytically reduce nitrate and oxidize methanol at the cathode and anode of the cell, respectively. The carbon nanofiber acts as the support material, enhances charge transfer, converts NO_3^- to NO_2^-, and suppresses the competitive HER. The $CuCO_2O_4$ nanoparticles reduce the adsorbed *NO_2 to NH_3. By leveraging the bifunctional nature of the spinel oxide catalyst and improving the thermodynamic favourability of NO_3RR, the water splitting at the anode has been substituted with the methanol oxidation reaction (MOR). Another advantage of coupling the MOR with NO_3RR is that it produces two value-added products instead of one: ammonia from NO_3RR and formate from MOR. Photoelectrochemical synthesis of ammonia is a green and sustainable technology, however, it suffers from a few bottlenecks like lower solar energy-to-ammonia conversion, and entails an extra bias for nitrate reduction coupled with water oxidation. To achieve bias-free photoelectrochemical ammonia production, researchers have recently designed 0D noble metal-based

5066 | Chem. Soc. Rev., 2025, 54, 5021–5080

This journal is © The Royal Society of Chemistry 2025

electrocatalysts that substitute water oxidation with the glycerol oxidation reaction (GOR). This cocatalysis technique has been used previously by CO_2 reduction catalysts to make the catalytic processes more energy efficient.[348–350] Along similar lines, a lead halide, triple cation-based perovskite photoelectrode with a smaller band gap and superior charge transfer properties has been fabricated, followed by the deposition of 0D electrocatalysts.[56] Nitrate is then reduced to ammonia at the cathode formed by the Ru nanoparticle-deposited titanate nanosheets. This NO_3RR is coupled with the GOR at the anode composed of Pt nanoparticle-deposited titanate nanosheets. These titanate nanosheets are more stable and corrosion-proof than conventional carbon material-based supports. This coupled photoelectrocatalytic system can lead to bias-free generation of ammonia utilizing solar energy sources, and this work considerably paves a lower-energy pathway for ammonia production, which is crucial in current catalytic ammonia synthesis research. Apart from green ammonia, this system

also produces value-added products like glyceric acid and lactic acid from glycerol oxidation.

7.3.2. 1D nanostructured and heterostructured catalysts.

1D tungsten phosphide (WP) nanowires can operate as bifunctional catalysts by acting as reducing catalysts at the cathode and oxidizing catalysts at the anode. Exploiting this redox property of WP nanowires, NO_3RR has been coupled with oxygen evolution reaction (OER), hydrazine oxidation reaction (HzOR), and urea oxidation reaction (UOR) and a comparative study of the operating cell potentials of these reactions has been presented in this work (Fig. 23A–D).[55] The overall potential of NO_3RR-OER requires 1.54 V and NO_3RR-UOR requires 1.38 V, whereas NO_3RR-HzOR occurs at a much lower potential of 0.24 V vs. RHE. Thus, coupling NO_3RR with hydrazine oxidation leads to more energy-efficient ammonia production. The product corresponding to NO_3RR is NH_3, while the products for OER, UOR, and HzOR are O_2, (CO_2, N_2), and N_2, respectively. This system provides an alternative green route
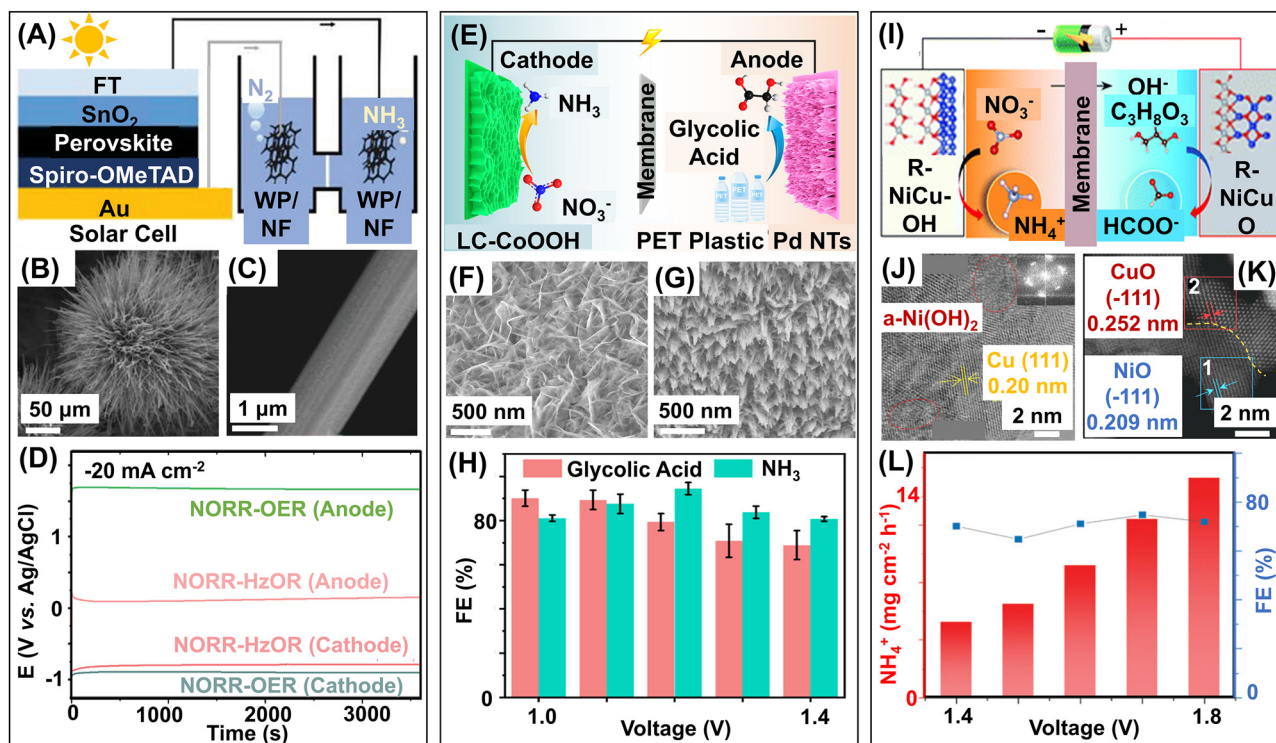

Fig. 23 Low-dimensional catalysts for ammonia synthesis via nitrate reduction coupled with oxidation reactions. (A) Schematic representation showing nitrate reduction (NO_3RR) coupled hydrazine oxidation (HzOR) by tungsten phosphide (WP) nanowires deposited on Ni foam (WP/NF) electrodes coupled with perovskite solar cell. (B) Low and (C) high magnification SEM images of WP nanowires. (D) Potential profiles comparing the cathodic and anodic nitrate reduction-coupled hydrazine oxidation reaction (NORR-HzOR) and nitrate reduction-coupled oxygen evolution reaction (NORR-OER). Reproduced with permission from ref. 55. Copyright 2023, Wiley-VCH. (E) Schematic representation of co-electrolysis of NO_3^- and PET plastic at the low-crystalline CoOOH-based cathode and Pd nanothorn-based anodes to produce NH_3 and glycolic acid simultaneously. (F) SEM image of the low-crystalline CoOOH grown on cobalt foam. (G) SEM image of Pd nanothorns grown on Ni foam. (H) Faradaic efficiencies of NH_3 and glycolic acid produced at different potentials. Reproduced with permission from ref. 54. Copyright 2023, American Chemical Society. (I) Schematic representation of paired electrochemical refining, where NiCu-based electrodes convert nitrate and glycerol to value-added ammonia and formate, respectively. (J) HRTEM image of reconstructed NiCu−OH cathode showcasing amorphous $Ni(OH)_2$ marked by red circles and lattice fringes with d-spacing of 0.20 nm corresponding to (111) planes of crystalline Cu, inset showing the corresponding FFT pattern. (K) STEM image of the reconstructed NiCuO anode showing lattice fringes with d-spacings of 0.209 nm (blue square) corresponding to the (200) of cubic NiO phase and 0.252 nm (red square), corresponding to the (111) plane of the monoclinic CuO phase. (L) NH_3 yields and the corresponding Faradaic efficiencies at the reconstructed NiCu−OH cathode at different voltages. Reproduced with permission from ref. 352. Copyright 2022, Royal Society of Chemistry.

This journal is © The Royal Society of Chemistry 2025

Chem. Soc. Rev., 2025, **54**, 5021–5080 | **5067**

for ammonia synthesis at a much lower energy than other systems using sluggish water oxidation as the half-reaction. HzOR to N_2 requires 4 electrons while the NO_3RR to NH_3 is an 8-electron process. Hence, the kinetics of NO_3RR is more sluggish. To couple these two reactions to produce a galvanic cell, the design of appropriate catalysts is required that can operate at low overpotentials and generate a maximum output voltage. In an attempt to design such a cell, 1D bimetallic RuCo nanorods act as efficient precatalysts for both cathodic and anodic reactions.[351] Nitrate and hydrazine wastewater are fed into the cathodic and anodic chambers of the cell. At the anode, the RuCo nanorods oxidize hydrazine to N_2 at a very low overpotential of -0.031 V $vs.$ RHE. Simultaneously, the same RuCo nanorods have been used to reduce NO_3^- to value-added NH_3 at 0.161 V $vs.$ RHE at the cathode. However, post-reaction characterizations reveal the formation of heterostructures of $Ru|Cu(OH)_2$ 2D nanosheets over RuCo precatalysts, and it has been noted that these reconstructed nanosheets in $situ$ are the active sites for HzOR and NO_3RR. Due to the overuse of plastic by mankind and its toxicity, plastic waste is one of the most common forms of pollutant noted in water, landfills, and the environment. From this viewpoint, in a recent work, NO_3RR has been coupled with the oxidation of ethylene glycol in polyethylene terephthalate (PET) for waste upcycling (Fig. 23E–H).[54] Low crystalline CoOOH catalysts reduce nitrates to produce ammonia at the cathode. Due to low crystallinity, the catalysts have both crystalline and amorphous regions. The amorphous area of the catalysts is endowed with a disordered atomic structure and dangled chemical bonds, which provide more active sites for the adsorption of NO_3^-. The crystallinity enhances the conductivity of the catalyst and promotes electron transfer for NO_3RR. For PET conversion, the anode is formed by 1D Pd nanothorns. The nanothorns have a high curvature tip, which enhances the local electric field and, thus, ensures the availability of a concentration of OH^- near the active site. The OH^- converts the ethylene glycol in PET to carbonyl compounds. Pd nanothorns anode can not only result in the degradation of plastics but also form value-added products like glycolic acid and formate. These coupled redox reactions can lead to the formation of multiple value-added products at the same time in an energy-efficient fashion.

7.3.3. **2D nanostructured and heterostructured catalysts.** Arrays of 2D nanosheets of cobalt phosphide on carbon fiber cloth can electrochemically reduce NO_3^- to produce NH_3 under ambient conditions with a Faradaic efficiency of $\sim 100\%$ in an alkaline medium.[353] Mechanistic investigations indicate that the P centers of the catalyst optimize the active phase and the energy barriers for NO_3RR, and the Co centers adsorb NO_3^- and promote electron transfer for the catalytic process. Here, the oxidation reaction, OER at the anode, is replaced with benzyl alcohol oxidation. This approach lowers the potential of the oxidation reaction from $E^0 = 1.23$ V $vs.$ RHE for OER to $E^0 = 0.48$ V $vs.$ RHE, indicating the benzyl alcohol oxidation to be thermodynamically more favourable than OER. Apart from lowering the overpotential, coupling of the benzyl alcohol oxidation can also yield value-added products like

benzaldehyde and benzoic acid, besides ammonia. The potential of the coupled oxidation reaction can also be lowered by replacing OER with sulfide oxidation reaction (SOR), requiring a lower potential of 0.65 V $vs.$ RHE to attain 100 mA cm^{-2}.[354] For obtaining nitrite reduction reaction (NO_2RR) coupled with SOR, 2D CoNiOOH nanosheets can work as bifunctional catalysts, which can simultaneously generate two value-added products, ammonia and elemental sulfur, from NO_2RR and SOR, respectively. The Ni dopant facilitates the adsorption of NO_2^- and S^{2-}, lowers energy barriers, and enhances NO_2RR and SOR simultaneously. The synchronous production of two value-added products at the cathode and anode offers a greener energy-saving approach for chemical production. Another example of the NO_3RR-coupled glycerol oxidation reaction (GOR) catalyst includes non-noble bimetallic 2D NiCu–OH nanosheets fabricated by co-electrodeposition of amorphous $Ni(OH)_2$ and crystalline $Cu_2(OH)_2(NO_3)$.[352] These 2D nanosheets act as the precatalysts for NO_3RR and GOR at the cathode and anode, respectively (Fig. 23I–L). NiCu–OH can be reconstructed to Cu nanoparticles and amorphous $Ni(OH)_2$ at the cathode under the operating reaction conditions for NO_3RR. The metallic Cu produced in $situ$ at the cathode catalytically reduces NO_3^- to produce green NH_3. Concurrently, at the anode, under the reaction conditions of GOR, NiCu–OH is reconstructed to form Cu-vacant $CuO/NiOOH$ composites. These bimetallic composites catalytically oxidize glycerol to value-added formate. These reconstructed 2D nanosheets have also been used to build a proof-of-concept paired electrochemical refinery that can perform NO_3RR and GOR at low cell voltage and simultaneously generate ammonium and formate. This work provides a proof-of-concept and paves an alternative way for constructing large-scale electrolyzers for ammonia synthesis.

8. Conclusions and perspectives

Over the past decade, the development of novel low-dimensional materials in electrocatalysis and photocatalysis has not only advanced the efficient synthesis of various value-added products but has also deepened our understanding of the complex mechanisms behind catalytic reactions, simplifying the design of more effective catalysts. The electronic properties of these materials can be easily tuned and their interfaces modulated for better adsorption and availability of catalytic sites, thereby making them suitable for photocatalysis and electrocatalysis. The combined effects of the materials and unique interfacial properties present in the heterostructures make them state-of-the-art catalysts in this field. Doping, defects, facet engineering, and formation of heterojunctions boost the catalytic properties of the low-dimensional materials. These catalytic materials can lead to selective production of green ammonia in a sustainable fashion by the reduction of N-containing species like N_2, NO_x, or NO_x^-. The enzymes present in the nitrogen cycle act as the inspiration for fabricating active low-dimensional materials as catalysts. In this review, we have

outlined the recent 0D, 1D, and 2D low-dimensional materials used for the photo- and/or electrocatalytic production of ammonia. These low-dimensional materials present an array of physical and chemical characteristics for boosting the catalytic reactions. For instance, the alignment of the band positions of the photocatalysts and the redox potentials of the desired reactions is crucial for performing the photocatalytic reactions. Low-dimensional materials offer the opportunity to design heterostructures such that the band positions can be engineered to align with the redox potentials of N_2RR and NO_xRR. The important features of low-dimensional materials like light absorption properties, charge carrier properties, and lower recombination of charges further make them ideal photocatalysts. Most state-of-the-art photocatalysts developed in the lab use simulated light sources. Direct harvest of solar light for the effective generation of ammonia still poses a challenge. Though few reports of solar light-harvesting photocatalysts have been reported, their efficiency is unsatisfactory. Hence, increasing the solar-to-fuel efficiency of the photocatalysts for the production of ammonia remains a major concern. Quantum materials with plasmonic structures have better light absorption properties and can be used to design efficient photocatalysts. The band structures of quantum materials are optimized to provide the electrons required for the catalytic reactions and, thus they act as electron reservoirs. The quantum states can provide better conductivity, transportation of charges, improved lifetime, and enhanced surface properties, which make them prospective materials for energy-converting catalytic reactions. Quantum materials can transfer charge and electron spin, which might boost the catalytic activity of reduction reactions of N-containing species to ammonia. Generally, the production of ammonia originates from the reduction of dinitrogen or nitrates, which requires 6 and 8 electrons, respectively, and, in principle, the reactions require high overpotentials to surpass the high energy barrier. In electrocatalysis, the low-dimensional materials are supposed to provide lower overpotential compared with ideal thermodynamic potentials. However, the overpotentials reported for most electrocatalysts developed for ammonia production are still much higher than the thermodynamic potential, which requires further initiatives for designing heterostructures from experimental and theoretical aspects. Determination of the active sites of the catalysts through theoretical calculations is also pertinent for assessing and comparing the performance of various catalytic materials. To effectively utilize electrocatalytically synthesized ammonia in fertilizers, it is crucial to select appropriate electrolytes. Electrolytes should be non-toxic for plants and also should not affect their growth. NaCl, KOH, and Na_2SO_4 are mostly used as electrolytes for this purpose. For large-scale practical applications, designing flow cells appears to be a promising strategy, and some progress has been made in this area. However, significant optimizations are still required to enhance efficiency, increase yield, and improve the stability of catalysts before they can be used for the mass production of ammonia. The stability of catalysts is often hindered due to side reactions and can be modulated by driving the flow of charge carriers to

the active sites for the reaction. The input of two energy sources, photo and electrical energy for generating ammonia by photocathodes has also been explored. However, state-of-the-art photoelectrocatalysts developed at the lab-scale report a low efficiency of ammonia production. Coupling with an electric grid or battery to increase the current density might lead to a higher yield of ammonia.

Over the past years, the constant progress in ammonia synthesis has necessitated the establishment of a rigorous protocol for the measurement and quantification of NH_3. Though diverse and well-established quantification techniques exist in the literature, contamination from different nitrogen-containing molecules like NO_x or a non-negligible amount of ammonia from solvents or electrolytes, nitrogen or hydrogen leaching, and non-catalytic ammonia production can lead to errors in the quantification of ammonia. Additionally, ammonia can be in the form of ammonium ion (NH_4^+) or un-ionized ammonia (NH_3) in liquid reaction media, depending on the pH and the temperature. At higher temperatures and pH (>11), ammonia predominantly remains in the gaseous state.[355] Hence, in alkaline solutions, gaseous ammonia is present in the head space and the liquid phase as dissolved gas. This further complicates the quantitative analysis and preserving the samples for measurements. Reviews and protocols describing the correct method for ammonia measurement and quantification are present in the literature, following which correct protocols for ammonia quantification can be established in the lab.[5,15,24,356,357] Among the existing techniques, the spectroscopic methods for ammonia quantification are the most common, less expensive and widely used. However, these methods depend on the pH of the reaction medium and the concentration of ammonia to be measured. For instance, Nessler's reagent method works in both alkaline and acidic solutions, over a concentration range of 0–8 mg L^{-1}.[357] However, the high alkalinity of Nessler's reagent, the toxicity due to the presence of mercury, and the short lifetime somewhat limit the use of this method. The indophenol blue method, another spectroscopic technique, works in alkaline media and detects low-concentration ammonia ranging from 0–0.6 mg NH_3–N L^{-1}.[15] Nevertheless, the sample preparation for this method is lengthy and the presence of organic nitrogen-containing molecules can perturb the quantification. The salicylate spectroscopic method despite being a stable method suffers from major drawbacks like lower sensitivity and higher cost. Ion chromatography is also widely used for the quantification of ammonia and it offers many advantages over the spectroscopic methods, including efficiency, reproducibility, and high sensitivity toward NH_4^+ detection, and covers a wide detection range of 0.02–40 mg NH_3–N L^{-1}.[136] However, this process is comparatively expensive, requires complex instrumentation, proper selection of columns and eluents, and is sometimes incompatible with acidic or basic solutions, and organic solvents. Ammonia can also be detected by fluorescence upon reaction with o-phthaldialdehyde and sulfite, but the detection limit is only up to 1 nmol L^{-1}.[358] Ammonium ion-selective electrode (ISE) is another efficient technique for the

This journal is © The Royal Society of Chemistry 2025

Chem. Soc. Rev., 2025, **54**, 5021–5080 | **5069**

measurement of ammonia with concentrations ranging 0.03–1400 mg NH_3–N L^{-1}, however, the accuracy of this method is poor for concentrations less than 0.5 mg NH_3–N L^{-1}.[136] Extensive background control experiments are always necessary to check and confirm the presence of any non-synthesized ammonia contaminants. In this regard, nuclear magnetic resonance (NMR) techniques with isotope labeling experiments play a crucial role. Catalytic experiments with ^{15}N-labeled N-sources as reactants analyzed by ^1H and ^{15}N NMR methods can provide conclusive proof of the catalytic production of ammonia. The use of ^{15}N-isotope-labeled reactant generates $^{15}NH_4^+$, which can be confirmed from ^1H NMR spectra showing the chemical shifts of triplet coupling of ^{14}N and doublet coupling for ^{15}N.[5] In the case of non-aqueous systems, the presence of organic solvents sometimes interferes with the detection of the NH_3 signal, which can be resolved using solvent signal suppression methods. The accurate concentration of ammonia can be measured by calibration curves with standard solutions containing ammonia. Isotope-labeling experiments can also be performed with liquid chromatography–mass spectrometry (LC–MS) techniques. An LC-MS coupled Berthelot assay can detect $^{14}NH_3$ and $^{15}NH_3$ by analyzing ^{14}N-indophenol (m/z: 198) and ^{15}N-indophenol (m/z: 199) formed by Berthelot reactions.[359] Although many quantification techniques are available, based on the reaction conditions, reactants, solvents, and the concentration of ammonia produced, the appropriate method has to be chosen for the accurate quantification of ammonia.

Despite the vast ongoing research on ammonia production, certain obstacles persist, necessitating additional progress. Currently, researchers are focusing on addressing these challenges and a few advancements have been achieved, and further upgradation in these aspects is required in the future. Despite being energy-intensive and leaving a significant carbon footprint, the Haber–Bosch (H–B) approach remains the industrial technology for ammonia synthesis. Recent efforts are now directed toward modification of the H–B plants with CO_2 capture facilities to reduce the carbon footprint. Different electrolyzers have been developed in recent years to increase the energy efficiency of the ammonia synthesis process. For instance, the Topsoe green ammonia demonstration uses a high-temperature solid oxide electrolyzer cell to power the ammonia synthesis process.[360] This electrolyzer can split water to generate green hydrogen and separate nitrogen from the air, thus reducing energy input intake and increasing overall efficiency. The small-scale green ammonia demonstrator by the ThyssenKrupp industries applies the chlor-alkaline water electrolyzer cell for ammonia synthesis.[361] Polymer electrolyte membrane (PEM)-based electrolyzers are often used for industrial-scale ammonia synthesis. The green ammonia plant planned by Yara proposes to use a PEM electrolyzer produced by ITM Power.[362] The wind power-to-ammonia demonstrator at Harwell, Oxford, United Kingdom, in association with Siemens, uses a PEM water electrolyzer to produce H_2 and N_2 from air separation over a Johnson Matthey Fe-based catalyst.[363] In an attempt to develop decentralized and energy-efficient

technologies for ammonia generation, Europe has also proposed over 20 projects by 2030 for green ammonia generation.[364] Green ammonia-generating plants are now being proposed to be constructed or currently are constructed in different parts of the world, such as the Australian Renewable Energy Agency (ARENA) in western Australia, Kapsom in north-eastern India, and Fertiberia in Spain.[365–367] The Yuri Renewable Hydrogen to Ammonia Project, led by Yara Pilbara Fertilisers Pty. Ltd (Yara), a fertilizer company, and ENGIE, a leader in low-carbon energy and services, with the support of ARENA, ENGINE, and Mitsui & Co. Ltd (Mitsui), was started in 2022, and is expected to be complete in 2028. This project proposes to industrially scale up the production of green ammonia using off-grid intermittent renewable H_2 obtained via electrolysis. This project also aims to build a 10 MW electrolyzer powered by 18 MW solar PV and supported by an 8 MW battery energy storage system.[365] In the same year (2022), Fertiberia, a Spanish fertilizer producer with support from the Green H2F project also constructed a green ammonia plant in Spain with Iberdrola and Spain's National Hydrogen Center. This plant project has a 20 PEM MW electrolyzer powered by a 100 MW PV with a capacity of 3000 t_{H_2} $year^{-1}$. An additional 800 MW capacity is also under development and will be complete by 2027.[368] Although the polymer electrolyte membrane (PEM) electrolyzers are quite promising H_2 production is somewhat limited by the low temperature. High-temperature electrolyzers including solid oxide or alkaline electrolyzers have also been considered but the higher cost limits their use for large-scale applications.[23] Different literature studies indicate that for the complete industrial production of decarbonized, sustainable production of green ammonia further developments are required to construct highly efficient electrolyzers ($>80\%$).[369] For entirely decarbonizing the Haber–Bosch approach to ammonia production, the upcoming goal is to generate ammonia from water, air, and renewable energy sources. In this regard, several photo- and/or electrocatalysts have been designed; still, they suffer from a few limitations like the cost and production of electrical energy and the low yield of ammonia produced in the range of mmol h^{-1} g^{-1}. The yield of ammonia in the millimolar range is quite inferior compared to industrial standards. Hence, the photo- and electrocatalytic approaches developed so far are not sufficient for the lab to industrial-level scale-up of the technology. Further investigations in this regard are necessary and would require cumulative expertise from the fields of materials science, catalysis, reactor engineering, and the use of artificial intelligence and robotization.[24]

Ammonia is highly water soluble due to the hydrogen bond between ammonia and water; hence, it is difficult to separate from aqueous medium. Most photocatalytic and electrocatalytic reactions are performed in an aqueous media, and the extraction of ammonia from aqueous phase remains an obstacle in most cases. Air and steam stripping are sometimes used to separate ammonia from aqueous medium, but these processes are energy-intensive.[208] For air stripping of ammonia, maintenance of high airflow, temperature, and pressure of the

packed bed are required to separate ammonia from water and convert it to the gaseous phase, eventually consuming a significant amount of energy.[370] In the case of steam stripping, steam generation requires high temperatures consuming energy, while coupling heat recovery systems to improve the energy efficiency of this process can be complex and expensive.[371] Another effective way of ammonia separation is upscaling the produced ammonia to salts like ammonium sulfate or ammonium chloride. This process helps in easy ammonia retrieval and directly converts ammonia to fertilizers.[53,208,316] The development of membrane-based electrolyzers can also promote the separation of ammonia from the reaction medium. Recently, several lab-scale electrolyzers have been constructed for the electro/photoelectrocatalytic synthesis of ammonia. The electrolyzers have certain benefits over conventional catalytic setups. For instance, in conventional electrocatalysis electricity is sometimes harnessed from fossil fuels and produces greenhouse gases. Instead, the electrolyzers are powered by renewable energy sources like solar power or wind to produce electricity for the electrocatalytic reactions, thus making ammonia synthesis green and reducing the carbon footprint. Additionally, the electrolyzer concurrently couples electrosynthesis and gaseous product separation, which minimizes the undesired redox reaction between NH_3 and the oxidized products. Thus, the electrolyzers can produce highly pure ammonia with high yield rates and minimal loss. The electrolyzers can also participate in redox reactions and extract the oxidized and reduced products simultaneously. For instance, NH_3 and Cl_2 can be electrosynthesized simultaneously and separated by incorporating gas-extraction electrodes into a flow-type membrane-free electrolyzer, coupled with ammonia and chlorine trap channels and a waste stream channel.[372] Electrolyzers can be either membrane-based or membrane-free. The membrane-based electrolyzers can be proton exchange membranes (PEM), anion exchange membranes (AEM), or membrane–electrode assemblies (MEA). Membranes play a crucial role in determining the performance and scalability of ammonia-producing electrolyzers. In non-solid electrochemical/photoelectrochemical one-chamber cells, oxidation and reduction reactions occur in the single chamber and the ammonia produced upon reduction of N_2 or NO_x is susceptible to oxidation. To avoid this possibility, an electrolyzer consisting of a double-chamber cell or H-cell, separated by a proton exchange membrane (PEM) or an anion exchange membrane (AEM) is preferred. During the electrochemical reaction, the electrons generated at the anode-chamber can pass through the membrane to the cathode-chamber and participate in the N_2RR or NO_xRR to produce ammonia. However, the ammonia produced as NH_4^+ in aqueous solutions cannot cross the membrane, thus avoiding oxidation and product loss. Hence, the choice of membranes that can limit NH_4^+ crossover is extremely crucial. The most commonly used cation exchange membranes, Nafion 212 and Nafion 112 allow the transport of NH_4^+; therefore they prove inefficient for ammonia generation electrolyzers.[367,373] Among anion exchange membranes, AEM PiperION-A80 exhibits negligible NH_4^+ crossover in both acidic and neutral electrolytes and can be used for the electrosynthesis of ammonia in neutral or acidic reaction media. However, in basic electrolytes, AEM PiperION-A80 proves inefficient as it is permeable to NH_3 under basic conditions.[373] Additionally, membranes allow the freedom of using two different electrolytes in the cathodic and anodic chambers.[374] Anion exchange membranes are highly permeable to nitrates, hence, AEMs have to be avoided for NO_3RR systems. Instead, a proton-exchange membrane electrode assembly (PEMEA) constructed with Nafion 117 and coupled with electrocatalysts like oxide-derived Cu nanoneedle cathodes can efficiently produce ammonia from nitrates.[375] The production of ammonia can be scaled up from the millimolar range obtained from conventional electrocatalytic reactions by copper–tin alloy catalyst to molar range by transferring to a membrane electrode assembly (MEA) electrolyzer using renewable electricity and the cathode and anode separated by anion-exchange quaternary ammonium poly(*N*-methylpiperidine-*co*-*p*-terphenyl) (QAPPT) membrane.[322] To meet the real application and industrial standards of ammonia production *via* the NO_xRR process, electrocatalysis experiments are now performed in electrolyzers using various electrolytes to obtain ampere-level current density.[230,376,377] Achieving long-term stability of ion-exchange membranes is still a challenge in many works, thus limiting long operating time for catalysis and high yield of ammonia. The construction of a 3D physically interlocked interface bipolar membrane can increase water dissociation sites, ionic transfer, and interfacial stability. By combining a Co nanoarray cathode with the bipolar membrane reactor, electrosynthesis of ammonia with increased yield can be achieved at $1000\ mA\ cm^{-2}$ for 100 hours of operation.[378] MEA electrolyzers composed of cathodic CuZn ribbons, a proton exchange membrane (Nafion117), and an anodic IrO_2–Ti mesh, exhibit stable operation at $500\ mA\ cm^{-2}$ for 220 hours for producing ammonia.[379] The electrolytes in the electrolyzers also have a significant impact on ammonia synthesis. The design of a flow electrolyzer with chain-ether-based electrolyte and gas diffusion electrodes can demonstrate 300 hours of continuous operation under ambient conditions.[2] The flow electrolyzers can also help separate synthesized ammonia by constructing a 'two-in-one'' flow cell electrolyzer that integrates the two chambers of NO_3RR electrolysis, and NH_3 capture through a commercial gas diffusion electrode.[380] Apart from synchronized NH_3 production and capture, this electrolyzer rapidly transports NH_3 molecules away from the reaction interfaces, thereby promoting NO_3RR to NH_3. With such rapid development in catalyst and membrane design, electrolyzer device optimization; green, sustainable, carbon-free, low-cost, large-scale industrial methods for ammonia production are expected soon. A multidisciplinary approach is needed to upgrade lab-scale ammonia production into full-scale industrial ammonia fertilizer production. This includes expertise in photocatalysis, electrocatalysis, chemical separation, agricultural science, and technical engineering. These combined skills are essential to developing an efficient alternative to the Haber–Bosch process and addressing the current global demand for

This journal is © The Royal Society of Chemistry 2025

Chem. Soc. Rev., 2025, **54**, 5021–5080 | **5071**

sustainable ammonia production. Exploring and identifying the most efficient methods for ammonia production is a critical challenge this field must address in the coming years. Advancing these technologies will be the key to driving growth in both the agriculture-based economy and the energy sectors that rely on ammonia as a fuel source.

Author contributions

M. P., A. M., and C. C. M. conceived and designed the review. A. M. wrote the initial draft. A. M., C. C. M., and M. P. reviewed, edited, and wrote the manuscript. M. P. supervised the entire review. All the authors contributed to the discussion and manuscript preparation.

Data availability

No primary research results, software, or code have been included, and no new data were generated or analyzed as part of this review.

Conflicts of interest

The authors declare no competing financial interest.

Acknowledgements

References

1 R. F. Service, *Science*, 2018, **361**, 120–123.
2 S. Li, Y. Zhou, X. Fu, J. B. Pedersen, M. Saccoccio, S. Z. Andersen, K. Enemark-Rasmussen, P. J. Kempen, C. D. Damsgaard, A. Xu, R. Sažinas, J. B. V. Mygind, N. H. Deissler, J. Kibsgaard, P. C. K. Vesborg, J. K. Nørskov and I. Chorkendorff, *Nature*, 2024, **629**, 92–97.
3 K. Zhang, A. Cao, L. H. Wandall, J. Vernieres, J. Kibsgaard, J. K. Nørskov and I. Chorkendorff, *Science*, 2024, **383**, 1357–1363.
4 D. R. MacFarlane, P. V. Cherepanov, J. Choi, B. H. R. Suryanto, R. Y. Hodgetts, J. M. Bakker, F. M. F. Vallana and A. N. Simonov, *Joule*, 2020, **4**, 1186–1205.
5 H. Iriawan, S. Z. Andersen, X. Zhang, B. M. Comer, J. Barrio, P. Chen, A. J. Medford, I. E. L. Stephens, I. Chorkendorff and Y. Shao-Horn, *Nat. Rev. Methods Primers*, 2021, **1**, 56.
6 J. Kim and D. C. Rees, *Biochemistry*, 1994, **33**, 389–397.
7 K. A. Brown, D. F. Harris, M. B. Wilker, A. Rasmussen, N. Khadka, H. Hamby, S. Keable, G. Dukovic, J. W. Peters, L. C. Seefeldt and P. W. King, *Science*, 2016, **352**, 448–450.
8 Z. Chen, G. Quek, J.-Y. Zhu, S. J. W. Chan, S. J. Cox-Vázquez, F. Lopez-Garcia and G. C. Bazan, *Angew. Chem., Int. Ed.*, 2023, **62**, e202307101.
9 D. Voiry, H. S. Shin, K. P. Loh and M. Chhowalla, *Nat. Rev. Chem.*, 2018, **2**, 0105.
10 C. Katan, N. Mercier and J. Even, *Chem. Rev.*, 2019, **119**, 3140–3192.
11 T. Edvinsson, *R. Soc. Open Sci.*, 2018, **5**, 180387.
12 Q. Shao, P. Wang, T. Zhu and X. Huang, *Acc. Chem. Res.*, 2019, **52**, 3384–3396.
13 Y. Pang, C. Su, G. Jia, L. Xu and Z. Shao, *Chem. Soc. Rev.*, 2021, **50**, 12744–12787.
14 Y. Ruan, Z.-H. He, Z.-T. Liu, W. Wang, L. Hao, L. Xu, A. W. Robertson and Z. Sun, *J. Mater. Chem. A*, 2023, **11**, 22590–22607.
15 G. Qing, R. Ghazfar, S. T. Jackowski, F. Habibzadeh, M. M. Ashtiani, C.-P. Chen, M. R. Smith III and T. W. Hamann, *Chem. Rev.*, 2020, **120**, 5437–5516.
16 Y. Shi, Z. Zhao, D. Yang, J. Tan, X. Xin, Y. Liu and Z. Jiang, *Chem. Soc. Rev.*, 2023, **52**, 6938–6956.
17 Y. Xiong, Y. Wang, J. Zhou, F. Liu, F. Hao and Z. Fan, *Adv. Mater.*, 2024, **36**, 2304021.
18 A. K. K. Padinjareveetil and M. Pumera, *Adv. Mater. Interfaces*, 2023, **10**, 2201734.
19 B. Wang, S. Chen, Z. Zhang and D. Wang, *SmartMat*, 2022, **3**, 84–110.
20 S. Li, X. Fu, J. K. Nørskov and I. Chorkendorff, *Nat. Energy*, 2024, **9**, 1344–1349.
21 J. John, D. R. MacFarlane and A. N. Simonov, *Nat. Catal.*, 2023, **6**, 1125–1130.
22 B. H. R. Suryanto, H.-L. Du, D. Wang, J. Chen, A. N. Simonov and D. R. MacFarlane, *Nat. Catal.*, 2019, **2**, 290–296.
23 D. Ye and S. C. E. Tsang, *Nat. Synth.*, 2023, **2**, 612–623.
24 L. Collado, A. H. Pizarro, M. Barawi, M. García-Tecedor, M. Liras and V. A. D. L. P. O'Shea, *Chem. Soc. Rev.*, 2024, **53**, 11334–11389.
25 Y. Feng, L. Jiao, X. Zhuang, Y. Wang and J. Yao, *Adv. Mater.*, 2025, **37**, 2410909.
26 W.-Q. Li, M. Xu, J.-S. Chen and T.-N. Ye, *Adv. Mater.*, 2024, **36**, 2408434.
27 R. Nittoor-Veedu, X. Ju and M. Pumera, *Adv. Energy Mater.*, 2024, 2402205.
28 G. Gan, G. Hong and W. Zhang, *Adv. Funct. Mater.*, 2024, 2401472.
29 Y. Zhou, X. Fu, I. Chorkendorff and J. K. Nørskov, *ACS Energy Lett.*, 2025, **10**, 128–132.
30 S. Yin, Z. Guan, Y. Zhu, D. Guo, X. Chen and S. Wang, *ACS Nano*, 2024, **18**, 27833–27852.
31 M. Majumder, H. Saini, I. Dědek, A. Schneemann, N. R. Chodankar, V. Ramarao, M. S. Santosh, A. K. Nanjundan, S. Kment, D. Dubal, M. Otyepka, R. Zbořil and K. Jayaramulu, *ACS Nano*, 2021, **15**, 17275–17298.

5072 | *Chem. Soc. Rev.*, 2025, **54**, 5021–5080

This journal is © The Royal Society of Chemistry 2025

32 T. Hu, X. Cheng, J. Luo, Y. Yan, Q. Zhang and Y. Li, *ACS Catal.*, 2024, **14**, 14539–14563.

33 H. Fang, D. Liu, Y. Luo, Y. Zhou, S. Liang, X. Wang, B. Lin and L. Jiang, *ACS Catal.*, 2022, **12**, 3938–3954.

34 X. Long, F. Huang, Z. Yao, P. Li, T. Zhong, H. Zhao, S. Tian, D. Shu and C. He, *Small*, 2024, **20**, 2400551.

35 Y. Li, Q. Zhang, Z. Mei, S. Li, W. Luo, F. Pan, H. Liu and S. Dou, *Small Methods*, 2021, **5**, 2100460.

36 K. Ithisuphalap, H. Zhang, L. Guo, Q. Yang, H. Yang and G. Wu, *Small Methods*, 2019, **3**, 1800352.

37 N. H. Truong, J.-S. Kim, J. Lim and H. Shin, *Chem. Eng. J.*, 2024, **495**, 153108.

38 S. M. Ghoreishian, K. Shariati, Y. S. Huh and J. Lauterbach, *Chem. Eng. J.*, 2023, **467**, 143533.

39 A. H. Pizarro, J. Fermoso, M. García-Tecedor, M. Barawi, V. A. D. L. P. O'Shea and L. Collado, *J. Mater. Chem. A*, 2024, **12**, 16987–17001.

40 C.-W. Tsao, M.-J. Fang and Y.-J. Hsu, *Coord. Chem. Rev.*, 2021, **438**, 213876.

41 Y. Wang, H. Yin, X. Zhao, Y. Qu, A. Zheng, H. Zhou, W. Fang and J. Li, *Appl. Catal., B*, 2024, **341**, 123266.

42 J. Qin, X. Hu, X. Li, Z. Yin, B. Liu and K.-H. Lam, *Nano Energy*, 2019, **61**, 27–35.

43 H. Yin, Z. Chen, Y. Peng, S. Xiong, Y. Li, H. Yamashita and J. Li, *Angew. Chem., Int. Ed.*, 2022, **61**, e202114242.

44 M. Mohebinia, X. Xing, G. Yang, D. Wang, C. Solares-Bockmon, Z. Ren and J. Bao, *Mater. Today Chem.*, 2022, **24**, 100993.

45 Y. Kong, L. Wu, X. Yang, Y. Li, S. Zheng, B. Yang, Z. Li, Q. Zhang, S. Zhou, L. Lei, G. Wu and Y. Hou, *Adv. Funct. Mater.*, 2022, **32**, 2205409.

46 D. Yin, D. Chen, Y. Zhang, W. Wang, Q. Quan, W. Wang, Y. Meng, Z. Lai, Z. Yang, S. Yip, C.-Y. Wong, X. Bu, X. Wang and J. C. Ho, *Adv. Funct. Mater.*, 2023, **33**, 2303803.

47 W. Tong, B. Huang, P. Wang, L. Li, Q. Shao and X. Huang, *Angew. Chem., Int. Ed.*, 2020, **59**, 2649–2653.

48 A. K. K. Padinjareveetil, J. V. Perales-Rondon and M. Pumera, *Adv. Mater. Technol.*, 2023, **8**, 2202080.

49 Y. J. Jang, A. E. Lindberg, M. A. Lumley and K.-S. Choi, *ACS Energy Lett.*, 2020, **5**, 1834–1839.

50 L. P. Camargo, P. R. C. da Silva, A. Batagin-Neto, V. Klobukoski, M. Vidotti and L. H. Dall'Antonia, *Appl. Mater. Today*, 2022, **28**, 101540.

51 B. Wang, L. Yao, G. Xu, X. Zhang, D. Wang, X. Shu, J. Lv and Y.-C. Wu, *ACS Appl. Mater. Interfaces*, 2020, **12**, 20376–20382.

52 M. A. Mushtaq, A. Kumar, G. Yasin, M. Arif, M. Tabish, S. Ibraheem, X. Cai, W. Ye, X. Fang, A. Saad, J. Zhao, S. Ji and D. Yan, *Appl. Catal., B*, 2022, **317**, 121711.

53 J. Gao, N. Shi, Y. Li, B. Jiang, T. Marhaba and W. Zhang, *Environ. Sci. Technol.*, 2022, **56**, 11602–11613.

54 T. Ren, Z. Duan, H. Wang, H. Yu, K. Deng, Z. Wang, H. Wang, L. Wang and Y. Xu, *ACS Catal.*, 2023, **13**, 10394–10404.

55 C. Lim, H. Roh, E. H. Kim, H. Kim, T. Park, D. Lee and K. Yong, *Small*, 2023, **19**, 2304274.

56 A. Tayyebi, R. Mehrotra, M. A. Mubarok, J. Kim, M. Zafari, M. Tayebi, D. Oh, S.-H. Lee, J. E. Matthews, S.-W. Lee, T. J. Shin, G. Lee, T. F. Jaramillo, S.-Y. Jang and J.-W. Jang, *Nat. Catal.*, 2024, **7**, 510–521.

57 C. Lv, C. Lee, L. Zhong, H. Liu, J. Liu, L. Yang, C. Yan, W. Yu, H. H. Hng, Z. Qi, L. Song, S. Li, K. P. Loh, Q. Yan and G. Yu, *ACS Nano*, 2022, **16**, 8213–8222.

58 X. Wei, Y. Liu, X. Zhu, S. Bo, L. Xiao, C. Chen, T. T. T. Nga, Y. He, M. Qiu, C. Xie, D. Wang, Q. Liu, F. Dong, C.-L. Dong, X.-Z. Fu and S. Wang, *Adv. Mater.*, 2023, **35**, 2300020.

59 Y. Zhao, Y. Ding, W. Li, C. Liu, Y. Li, Z. Zhao, Y. Shan, F. Li, L. Sun and F. Li, *Nat. Commun.*, 2023, **14**, 4491.

60 J. Geng, S. Ji, M. Jin, C. Zhang, M. Xu, G. Wang, C. Liang and H. Zhang, *Angew. Chem., Int. Ed.*, 2023, **62**, e202210958.

61 J. Shao, H. Jing, P. Wei, X. Fu, L. Pang, Y. Song, K. Ye, M. Li, L. Jiang, J. Ma, R. Li, R. Si, Z. Peng, G. Wang and J. Xiao, *Nat. Energy*, 2023, **8**, 1273–1283.

62 Q. Lai, T. Cai, S. C. E. Tsang, X. Chen, R. Ye, Z. Xu, M. D. Argyle, D. Ding, Y. Chen, J. Wang, A. G. Russell, Y. Wu, J. Liu and M. Fan, *Sci. Bull.*, 2022, **67**, 2124–2138.

63 H. Li, F. Pan, C. Qin, T. Wang and K.-J. Chen, *Adv. Energy Mater.*, 2023, **13**, 2301378.

64 M. Appl, *Ammonia*, Ullmann's Encyclopedia of Industrial Chemistry, 2006, DOI: **10.1002/14356007.a02_143.pub2**.

65 R. D. Milton, R. Cai, S. Abdellaoui, D. Leech, A. L. De Lacey, M. Pita and S. D. Minteer, *Angew. Chem., Int. Ed.*, 2017, **56**, 2680–2683.

66 J. Guo and P. Chen, *Acc. Chem. Res.*, 2021, **54**, 2434–2444.

67 O. Westhead, J. Barrio, A. Bagger, J. W. Murray, J. Rossmeisl, M.-M. Titirici, R. Jervis, A. Fantuzzi, A. Ashley and I. E. L. Stephens, *Nat. Rev. Chem.*, 2023, **7**, 184–201.

68 N. R. Dhar, E. V. Seshacharyulu and N. N. Biswas, *Proc. Natl. Inst. Sci.*, 1941, **7**, 115–131.

69 G. N. Schrauzer, N. Strampach, L. N. Hui, M. R. Palmer and J. Salehi, *Proc. Natl. Acad. Sci. U. S. A.*, 1983, **80**, 3873–3876.

70 H. Hirakawa, M. Hashimoto, Y. Shiraishi and T. Hirai, *J. Am. Chem. Soc.*, 2017, **139**, 10929–10936.

71 Q. Han, C. Wu, H. Jiao, R. Xu, Y. Wang, J. Xie, Q. Guo and J. Tang, *Adv. Mater.*, 2021, **33**, 2008180.

72 X. Gao, L. An, D. Qu, W. Jiang, Y. Chai, S. Sun, X. Liu and Z. Sun, *Sci. Bull.*, 2019, **64**, 918–925.

73 X. Chen, X. Zhang, Y.-H. Li, M.-Y. Qi, J.-Y. Li, Z.-R. Tang, Z. Zhou and Y.-J. Xu, *Appl. Catal., B*, 2021, **281**, 119516.

74 P. Li, S. Gao, Q. Liu, P. Ding, Y. Wu, C. Wang, S. Yu, W. Liu, Q. Wang and S. Chen, *Adv. Energy Sustainability Res.*, 2021, **2**, 2000097.

75 S. Zhang, Y. Zhao, R. Shi, C. Zhou, G. I. N. Waterhouse, L.-Z. Wu, C.-H. Tung and T. Zhang, *Adv. Energy Mater.*, 2020, **10**, 1901973.

76 Y. Zhao, L. Zheng, R. Shi, S. Zhang, X. Bian, F. Wu, X. Cao, G. I. N. Waterhouse and T. Zhang, *Adv. Energy Mater.*, 2020, **10**, 2002199.

77 W. Wang, H. Zhou, Y. Liu, S. Zhang, Y. Zhang, G. Wang, H. Zhang and H. Zhao, *Small*, 2020, **16**, 1906880.

This journal is © The Royal Society of Chemistry 2025

Chem. Soc. Rev., 2025, **54**, 5021–5080 | **5073**

78 Y. Lu, Y. Yang, T. Zhang, Z. Ge, H. Chang, P. Xiao, Y. Xie, L. Hua, Q. Li, H. Li, B. Ma, N. Guan, Y. Ma and Y. Chen, *ACS Nano*, 2016, **10**, 10507–10515.

79 G. N. Schrauzer and T. D. Guth, *J. Am. Chem. Soc.*, 1977, **99**, 7189–7193.

80 Y. Guan, H. Wen, K. Cui, Q. Wang, W. Gao, Y. Cai, Z. Cheng, Q. Pei, Z. Li, H. Cao, T. He, J. Guo and P. Chen, *Nat. Chem.*, 2024, **16**, 373–379.

81 C. S. Diercks, Y. Liu, K. E. Cordova and O. M. Yaghi, *Nat. Mater.*, 2018, **17**, 301–307.

82 X. Cui, C. Tang and Q. Zhang, *Adv. Energy Mater.*, 2018, **8**, 1800369.

83 A. R. Singh, B. A. Rohr, J. A. Schwalbe, M. Cargnello, K. Chan, T. F. Jaramillo, I. Chorkendorff and J. K. Nørskov, *ACS Catal.*, 2017, **7**, 706–709.

84 M. Ali, F. Zhou, K. Chen, C. Kotzur, C. Xiao, L. Bourgeois, X. Zhang and D. R. MacFarlane, *Nat. Commun.*, 2016, **7**, 11335.

85 H. E. Kim, J. Kim, E. C. Ra, H. Zhang, Y. J. Jang and J. S. Lee, *Angew. Chem., Int. Ed.*, 2022, **61**, e202204117.

86 M. A. Mushtaq, M. Arif, X. Fang, G. Yasin, W. Ye, M. Basharat, B. Zhou, S. Yang, S. Ji and D. Yan, *J. Mater. Chem. A*, 2021, **9**, 2742–2753.

87 M. S. Yu, S. C. Jesudass, S. Surendran, J. Y. Kim, U. Sim and M.-K. Han, *ACS Appl. Mater. Interfaces*, 2022, **14**, 31889–31899.

88 C. Sun, Z. Shao, Y. Hu, Y. Peng and Q. Xie, *ACS Appl. Mater. Interfaces*, 2023, **15**, 23085–23092.

89 X. Chen, N. Li, Z. Kong, W.-J. Ong and X. Zhao, *Mater. Horiz.*, 2018, **5**, 9–27.

90 B. Rytelewska, A. Chmielnicka, T. Chouki, M. Skunik-Nuckowska, S. Naghdi, D. Eder, A. Michalowska, T. Ratajczyk, E. Pavlica, S. Emin, Y. Fu, I. A. Rutkowska and P. J. Kulesza, *Electrochim. Acta*, 2023, **471**, 143360.

91 M. A. Shipman and M. D. Symes, *Catal. Today*, 2017, **286**, 57–68.

92 H. Wan, A. Bagger and J. Rossmeisl, *Angew. Chem., Int. Ed.*, 2021, **60**, 21966–21972.

93 X. Lu, H. Song, J. Cai and S. Lu, *Electrochem. Commun.*, 2021, **129**, 107094.

94 H. Liu, L. Bai, A. Bergmann, B. R. Cuenya and J. Luo, *Chem*, 2024, **10**, 2963–2986.

95 T. Ouyang, S. Huang, X.-T. Wang and Z.-Q. Liu, *Chem. – Eur. J.*, 2020, **26**, 14024–14035.

96 H. Gleiter, *Nanostruct. Mater.*, 1995, **6**, 3–14.

97 V. V. Pokropivny and V. V. Skorokhod, *Mater. Sci. Eng., C*, 2007, **27**, 990–993.

98 Z.-H. Xue, S.-N. Zhang, Y.-X. Lin, H. Su, G.-Y. Zhai, J.-T. Han, Q.-Y. Yu, X.-H. Li, M. Antonietti and J.-S. Chen, *J. Am. Chem. Soc.*, 2019, **141**, 14976–14980.

99 L. Meng, J. M. D. Lane, L. Baca, J. Tafoya, T. Ao, B. Stoltzfus, M. Knudson, D. Morgan, K. Austin, C. Park, P. Chow, Y. Xiao, R. Li, Y. Qin and H. Fan, *J. Am. Chem. Soc.*, 2020, **142**, 6505–6510.

100 B. Guan, X. Wang, Y. Xiao, Y. Liu and Q. Huo, *Nanoscale*, 2013, **5**, 2469–2475.

101 T. Hyeon, S. S. Lee, J. Park, Y. Chung and H. B. Na, *J. Am. Chem. Soc.*, 2001, **123**, 12798–12801.

102 J. Xu, S. Zhang, H. Liu, S. Liu, Y. Yuan, Y. Meng, M. Wang, C. Shen, Q. Peng, J. Chen, X. Wang, L. Song, K. Li and W. Chen, *Angew. Chem., Int. Ed.*, 2023, **62**, e202308044.

103 G. Liu, M. Zavelani-Rossi, G. Han, H. Zhao and A. Vomiero, *J. Mater. Chem. A*, 2023, **11**, 8950–8960.

104 M. Parente, M. van Helvert, R. F. Hamans, R. Verbroekken, R. Sinha, A. Bieberle-Hütter and A. Baldi, *Nano Lett.*, 2020, **20**, 5759–5764.

105 J. E. Omoriyekomwan, A. Tahmasebi, J. Zhang and J. Yu, *Energy Convers. Manage.*, 2019, **192**, 88–99.

106 H. Du, H. Guo, K. Wang, X. Du, B. A. Beshiwork, S. Sun, Y. Luo, Q. Liu, T. Li and X. Sun, *Angew. Chem., Int. Ed.*, 2023, **62**, e202215782.

107 G. Liu, Z. Tang, X. Gu, N. Li, H. Lv, Y. Huang, Y. Zeng, M. Yuan, Q. Meng, Y. Zhou and C. Wang, *Appl. Catal., B*, 2022, **317**, 121752.

108 Z. Chen, D. Chao, J. Liu, M. Copley, J. Lin, Z. Shen, G.-T. Kim and S. Passerini, *J. Mater. Chem. A*, 2017, **5**, 15669–15675.

109 R. Khare, D. B. Shinde, S. Bansode, M. A. More, M. Majumder, V. K. Pillai and D. J. Late, *Appl. Phys. Lett.*, 2015, **106**, 023111.

110 D. J. Lee, S.-H. Yu, H. S. Lee, A. Jin, J. Lee, J. E. Lee, Y.-E. Sung and T. Hyeon, *J. Mater. Chem. A*, 2017, **5**, 8744–8751.

111 W. Bai, S. Li, J. Ma, W. Cao and J. Zheng, *J. Mater. Chem. A*, 2019, **7**, 9086–9098.

112 G. Xia, S. Wang, X. Zhao and L. Zhou, *J. Mater. Chem. C*, 2013, **1**, 3291–3296.

113 Y. Min, G. D. Moon, B. S. Kim, B. Lim, J.-S. Kim, C. Y. Kang and U. Jeong, *J. Am. Chem. Soc.*, 2012, **134**, 2872–2875.

114 S. Mahasivam, V. Bansal and M. Sastry, *J. Phys. Chem. Lett.*, 2024, **15**, 3923–3928.

115 Z. L. Shaw, S. Kuriakose, S. Cheeseman, M. D. Dickey, J. Genzer, A. J. Christofferson, R. J. Crawford, C. F. McConville, J. Chapman, V. K. Truong, A. Elbourne and S. Walia, *Nat. Commun.*, 2021, **12**, 3897.

116 J. N. Tiwari, R. N. Tiwari and K. S. Kim, *Prog. Mater. Sci.*, 2012, **57**, 724–803.

117 S. Sun, M. Lu, X. Gao, Z. Shi, X. Bai, W. W. Yu and Y. Zhang, *Adv. Sci.*, 2021, **8**, 2102689.

118 P. Innocenzi and L. Stagi, *Acc. Mater. Res.*, 2024, **5**, 413–425.

119 Y. Zhang, F. Gao, H. You, Z. Li, B. Zou and Y. Du, *Coord. Chem. Rev.*, 2022, **450**, 214244.

120 Y. Lu, S. Du and R. Steinberger-Wilckens, *Appl. Catal., B*, 2016, **199**, 292–314.

121 H. Hou, G. Shao, W. Yang and W.-Y. Wong, *Prog. Mater. Sci.*, 2020, **113**, 100671.

122 X. Lu, C. Wang and Y. Wei, *Small*, 2009, **5**, 2349–2370.

123 L. Liang, X. Kang, Y. Sang and H. Liu, *Adv. Sci.*, 2016, **3**, 1500358.

124 Y. Xia, P. Yang, Y. Sun, Y. Wu, B. Mayers, B. Gates, Y. Yin, F. Kim and H. Yan, *Adv. Mater.*, 2003, **15**, 353–389.

5074 | *Chem. Soc. Rev.*, 2025, **54**, 5021–5080

This journal is © The Royal Society of Chemistry 2025

125 M. Byakodi, N. S. Shrikrishna, R. Sharma, S. Bhansali, Y. Mishra, A. Kaushik and S. Gandhi, *Biosens. Bioelectron.: X*, 2022, **12**, 100284.

126 T. A. Shifa, F. Wang, Y. Liu and J. He, *Adv. Mater.*, 2019, **31**, 1804828.

127 W. Huang, L. Hu, Y. Tang, Z. Xie and H. Zhang, *Adv. Funct. Mater.*, 2020, **30**, 2005223.

128 Z. He, J. Zhang, X. Li, S. Guan, M. Dai and S. Wang, *Small*, 2020, **16**, 2005051.

129 P. Sabatier, *La catalyse en chimie organique*, Paris & Liége Ch. Béranger Editeur, 1920.

130 Y. Zhu, W. Peng, Y. Li, G. Zhang, F. Zhang and X. Fan, *Small Methods*, 2019, **3**, 1800438.

131 J. K. Nørskov, T. Bligaard, J. Rossmeisl and C. H. Christensen, *Nat. Chem.*, 2009, **1**, 37–46.

132 Ž. Kovačič, B. Likozar and M. Huš, *ACS Catal.*, 2020, **10**, 14984–15007.

133 W. Hou and S. B. Cronin, *Adv. Funct. Mater.*, 2013, **23**, 1612–1619.

134 B. Bajorowicz, M. P. Kobylański, A. Gołąbiewska, J. Nadolna, A. Zaleska-Medynska and A. Malankowska, *Adv. Colloid Interface Sci.*, 2018, **256**, 352–372.

135 G. Zhang, Y. Li, C. He, X. Ren, P. Zhang and H. Mi, *Adv. Energy Mater.*, 2021, **11**, 2003294.

136 M. Li, H. Huang, J. Low, C. Gao, R. Long and Y. Xiong, *Small Methods*, 2019, **3**, 1800388.

137 J. Li, J. Wang, S. Shen, R. Chen, M. Liu and F. Dong, *Environ. Sci. Technol.*, 2023, **57**, 5445–5452.

138 H. Kominami, A. Furusho, S.-Y. Murakami, H. Inoue, Y. Kera and B. Ohtani, *Catal. Lett.*, 2001, **76**, 31–34.

139 M. Yamauchi, R. Abe, T. Tsukuda, K. Kato and M. Takata, *J. Am. Chem. Soc.*, 2011, **133**, 1150–1152.

140 G. Ren, J. Zhao, Z. Zhao, Z. Li, L. Wang, Z. Zhang, C. Li and X. Meng, *Angew. Chem., Int. Ed.*, 2024, **63**, e202314408.

141 G. Ren, M. Shi, Z. Li, Z. Zhang and X. Meng, *Appl. Catal., B*, 2023, **327**, 122462.

142 J. Bao, H. Maimaiti, J. Sun, L. Feng and X. Zhao, *Int. J. Hydrogen Energy*, 2024, **95**, 1–11.

143 X. Yu, P. Qiu, Y. Wang, B. He, X. Xu, H. Zhu, J. Ding, X. Liu, Z. Li and Y. Wang, *J. Colloid Interface Sci.*, 2023, **640**, 775–782.

144 P. Li, Z. Zhou, Q. Wang, M. Guo, S. Chen, J. Low, R. Long, W. Liu, P. Ding, Y. Wu and Y. Xiong, *J. Am. Chem. Soc.*, 2020, **142**, 12430–12439.

145 C. Liu, D. Hao, J. Ye, S. Ye, F. Zhou, H. Xie, G. Qin, J. Xu, J. Liu, S. Li and C. Sun, *Adv. Energy Mater.*, 2023, **13**, 2204126.

146 Y. Huang, Y. Zhu, S. Chen, X. Xie, Z. Wu and N. Zhang, *Adv. Sci.*, 2021, **8**, 2003626.

147 K. Li, W. Cai, Z. Zhang, H. Xie, Q. Zhong and H. Qu, *Chem. Eng. J.*, 2022, **435**, 135017.

148 Y. Fang, Y. Xue, L. Hui, H. Yu and Y. Li, *Angew. Chem., Int. Ed.*, 2021, **60**, 3170–3174.

149 K. Pournemati, A. Habibi-Yangjeh and A. Khataee, *ACS Appl. Nano Mater.*, 2024, **7**, 2200–2213.

150 D. Cui, S. Wang, X. Yang, L. Xu and F. Li, *Small*, 2024, **20**, 2306229.

151 D. Hao, J. Ren, Y. Wang, H. Arandiyan, M. Garbrecht, X. Bai, H. K. Shon, W. Wei and B.-J. Ni, *Energy Mater. Adv.*, 2021, **2021**, 9761263.

152 R. Fu, Y. Wang, G. Wang, Q. Zhan, L. Zhang and L. Liu, *Green Chem.*, 2023, **25**, 8531–8538.

153 Z. Zhao, R. Tan, Y. Kong, Z. Zhang, S. Qiu, X. Mu and L. Li, *Angew. Chem., Int. Ed.*, 2023, **62**, e202303629.

154 J. Li, R. Chen, J. Wang, Y. Zhou, G. Yang and F. Dong, *Nat. Commun.*, 2022, **13**, 1098.

155 J. Li, R. Chen, J. Wang, K. Wang, Y. Zhou, M. Xing and F. Dong, *Angew. Chem., Int. Ed.*, 2024, **63**, e202317575.

156 P. Li, R. Wu, P. Li, S. Gao, Z. Qin, X. Song, W. Sun, Z. Hua, Q. Wang and S. Chen, *Adv. Sci.*, 2024, **11**, 2408829.

157 V. Jain, S. Tyagi, P. Roy and P. P. Pillai, *J. Am. Chem. Soc.*, 2024, **146**, 32356–32365.

158 C. Feng, F. Raziq, M. Hu, H. Huang, Z.-P. Wu, S. Zuo, J. Luo, Y. Ren, B. Chang, D. Cha, S. Ayirala, A. Al-Yousef, T. D. Dao and H. Zhang, *Adv. Energy Mater.*, 2024, **14**, 2303792.

159 P. Xia, X. Pan, S. Jiang, J. Yu, B. He, P. M. Ismail, W. Bai, J. Yang, L. Yang, H. Zhang, M. Cheng, H. Li, Q. Zhang, C. Xiao and Y. Xie, *Adv. Mater.*, 2022, **34**, 2200563.

160 R. Wu, S. Gao, C. Jones, M. Sun, M. Guo, R. Tai, S. Chen and Q. Wang, *Adv. Funct. Mater.*, 2024, **34**, 2314051.

161 L. Zhang, R. Li, L. Cui, Z. Sun, L. Guo, X. Zhang, Y. Wang, Y. Wang, Z. Yu, T. Lei, X. Jian, X. Gao, C. Fan and J. Liu, *Chem. Eng. J.*, 2023, **461**, 141892.

162 K. Wu, Z. Wang, X. Zhang, C. Sun, Q. Li, H. Zhang, X. Bai, A. Khosla and Z. Zhao, *Langmuir*, 2024, **40**, 13603–13612.

163 Q. Zhang, Q. Li, H. Li, X. Shi, Y. Zhou, Q. Ye, R. Yang, D. Li and D. Jiang, *Inorg. Chem.*, 2023, **62**, 12138–12147.

164 Y. Liu, Y. Xue, L. Hui, H. Yu, Y. Fang, F. He and Y. Li, *Nano Energy*, 2021, **89**, 106333.

165 S. Liu, M. Wang, H. Ji, L. Zhang, J. Ni, N. Li, T. Qian, C. Yan and J. Lu, *Adv. Mater.*, 2023, **35**, 2211730.

166 T. He, Z. Zhao, R. Liu, X. Liu, B. Ni, Y. Wei, Y. Wu, W. Yuan, H. Peng, Z. Jiang and Y. Zhao, *J. Am. Chem. Soc.*, 2023, **145**, 6057–6066.

167 X. Zhang, Y. Liu, S. Feng, X. Gu, M. Zhou, H. Wang and J. Hua, *Appl. Catal., B*, 2024, **366**, 125013.

168 M. Yu, Y. Chen, M. Gao, G. Huang, Q. Chen and J. Bi, *Small*, 2023, **19**, 2206407.

169 X. Wang, G. Fan, S. Guo, R. Gao, Y. Guo, C. Han, Y. Gao, J. Zhang, X. Gu and L. Wu, *Angew. Chem., Int. Ed.*, 2024, **63**, e202404258.

170 J. Tan, H. Ren, Z. Zhao, X. Xin, Y. Shi, D. Yang and Z. Jiang, *Chem. Eng. J.*, 2023, **466**, 143259.

171 Z. Shen, F. Li, L. Guo, X. Zhang, Y. Wang, Y. Wang, X. Jian, X. Gao, Z. Wang, R. Li, C. Fan and J. Liu, *Appl. Catal., B*, 2024, **346**, 123732.

172 Y. Xi, Y. Xiang, T. Bao, Z. Li, C. Zhang, L. Yuan, J. Li, Y. Bi, C. Yu and C. Liu, *Angew. Chem., Int. Ed.*, 2024, **63**, e202409163.

173 C. Clavero, *Nat. Photonics*, 2014, **8**, 95–103.

174 K. T. Ranjit and B. Viswanathan, *J. Photochem. Photobiol., A*, 1997, **108**, 73–78.

This journal is © The Royal Society of Chemistry 2025

Chem. Soc. Rev., 2025, **54**, 5021–5080 | **5075**

175 A. Pandikumar, S. Manonmani and R. Ramaraj, *Catal. Sci. Technol.*, 2012, **2**, 345–353.

176 K. T. Ranjit, R. Krishnamoorthy, T. K. Varadarajan and B. Viswanathan, *J. Photochem. Photobiol., A*, 1995, **86**, 185–189.

177 I. G. Zacharia and W. M. Deen, *Ann. Biomed. Eng.*, 2005, **33**, 214–222.

178 R. Chen, J. Li, J. Wang, W. Yang, S. Shen and F. Dong, *Environ. Sci. Technol.*, 2023, **57**, 12127–12134.

179 P. Zhang, L. Chen, D.-H. Kuo, B. Wu, Z. Su, D. Lu, Q. Wu, J. Li, J. Lin and X. Chen, *J. Mater. Chem. A*, 2024, **12**, 7163–7177.

180 L. Chen, D. Shen, B. Li, Z. Xiao, W. Sun, X. Liu, J. Ma, C. Li and W. Wang, *Ceram. Int.*, 2023, **49**, 23129–23139.

181 J. Zhang, G. Zhang, H. Lan, H. Liu and J. Qu, *Chem. Eng. J.*, 2022, **428**, 130373.

182 G. Ren, M. Shi, S. Liu, Z. Li, Z. Zhang and X. Meng, *Chem. Eng. J.*, 2023, **454**, 140158.

183 X. Lv, W. Wei, F. Li, B. Huang and Y. Dai, *Nano Lett.*, 2019, **19**, 6391–6399.

184 K. Zhao and X. Quan, *ACS Catal.*, 2021, **11**, 2076–2097.

185 S. N. Habisreutinger, L. Schmidt-Mende and J. K. Stolarczyk, *Angew. Chem., Int. Ed.*, 2013, **52**, 7372–7408.

186 H. Hirakawa, M. Hashimoto, Y. Shiraishi and T. Hirai, *ACS Catal.*, 2017, **7**, 3713–3720.

187 X. Huang, R. Du, J. Ren, X. Li, M. Fu, S. Fu, T. Ma, L. Guo, R. A. Soomro, C. Yang and D. Wang, *ACS Catal.*, 2024, **14**, 13542–13549.

188 A. Mallick, J. Kim and M. Pumera, *Small*, 2025, **21**, 2407050.

189 H. Yu, F. Chen, X. Li, H. Huang, Q. Zhang, S. Su, K. Wang, E. Mao, B. Mei, G. Mul, T. Ma and Y. Zhang, *Nat. Commun.*, 2021, **12**, 4594.

190 H. Zheng, X. Li, K. Zhu, P. Liang, M. Wu, Y. Rao, R. Jian, F. Shi, J. Wang, K. Yan and J. Liu, *Nano Energy*, 2022, **93**, 106831.

191 S. Gao, H. Ji, P. Yang, M. Guo, J. Tressel, S. Chen and Q. Wang, *Small*, 2023, **19**, 2206114.

192 K.-C. Ma, H.-Y. Lin, Y.-C. Chen, C.-H. Tsai, K.-H. Zheng and J. M. Wu, *J. Mater. Chem. A*, 2024, **12**, 26866–26876.

193 Y. Fang, Y. Liu, L. Qi, Y. Xue and Y. Li, *Chem. Soc. Rev.*, 2022, **51**, 2681–2709.

194 N. Keller and T. Bein, *Chem. Soc. Rev.*, 2021, **50**, 1813–1845.

195 H. Wang, H. Wang, Z. Wang, L. Tang, G. Zeng, P. Xu, M. Chen, T. Xiong, C. Zhou, X. Li, D. Huang, Y. Zhu, Z. Wang and J. Tang, *Chem. Soc. Rev.*, 2020, **49**, 4135–4165.

196 Z. Zhao, Y. Nian, J. Shi, X. Xin, X. Huang, Y. Shi, J. Tan, Y. Zhang, Y. Han, D. Yang and Z. Jiang, *ACS Catal.*, 2024, **14**, 11626–11634.

197 H. Zhao, D. Zhang, H. Li, W. Qi, X. Wu, Y. Han, W. Cai, Z. Wang, J. Lai and L. Wang, *Adv. Energy Mater.*, 2020, **10**, 2002131.

198 L. Tan, N. Yang, X. Huang, L. Peng, C. Tong, M. Deng, X. Tang, L. Li, Q. Liao and Z. Wei, *Chem. Commun.*, 2019, **55**, 14482–14485.

199 Z. Liu, C. Wang, C. Chen, C. Li and C. Guo, *Electrochem. Commun.*, 2021, **131**, 107121.

200 X. Min and B. Liu, *Small*, 2023, **19**, 2300794.

201 D. Yao, C. Tang, L. Li, B. Xia, A. Vasileff, H. Jin, Y. Zhang and S.-Z. Qiao, *Adv. Energy Mater.*, 2020, **10**, 2001289.

202 D. Kim, S. Surendran, G. Janani, Y. Lim, H. Choi, M.-K. Han, S. Yuvaraj, T.-H. Kim, J. K. Kim and U. Sim, *Mater. Lett.*, 2022, **314**, 131808.

203 W. P. Utomo, H. Wu and Y. H. Ng, *Small*, 2022, **18**, 2200996.

204 L. Liu, T. Xiao, H. Fu, Z. Chen, X. Qu and S. Zheng, *Appl. Catal., B*, 2023, **323**, 122181.

205 X. Wang, X. Wu, W. Ma, X. Zhou, S. Zhang, D. Huang, L. R. Winter, J.-H. Kim and M. Elimelech, *Proc. Natl. Acad. Sci. U. S. A.*, 2023, **120**, e2217703120.

206 Y. Xue, Q. Yu, Q. Ma, Y. Chen, C. Zhang, W. Teng, J. Fan and W.-X. Zhang, *Environ. Sci. Technol.*, 2022, **56**, 14797–14807.

207 Y. Zhang, Y. Wang, L. Han, S. Wang, T. Cui, Y. Yan, M. Xu, H. Duan, Y. Kuang and X. Sun, *Angew. Chem., Int. Ed.*, 2023, **62**, e202213711.

208 F.-Y. Chen, Z.-Y. Wu, S. Gupta, D. J. Rivera, S. V. Lambeets, S. Pecaut, J. Y. T. Kim, P. Zhu, Y. Z. Finfrock, D. M. Meira, G. King, G. Gao, W. Xu, D. A. Cullen, H. Zhou, Y. Han, D. E. Perea, C. L. Muhich and H. Wang, *Nat. Nanotechnol.*, 2022, **17**, 759–767.

209 H. Liu, X. Lang, C. Zhu, J. Timoshenko, M. Rüscher, L. Bai, N. Guijarro, H. Yin, Y. Peng, J. Li, Z. Liu, W. Wang, B. R. Cuenya and J. Luo, *Angew. Chem., Int. Ed.*, 2022, **61**, e202202556.

210 S. Liu, S. Yin, S. Jiao, H. Zhang, Z. Wang, Y. Xu, X. Li, L. Wang and H. Wang, *Mater. Today Energy*, 2021, **21**, 100828.

211 Y. Wang, Y. Xiong, M. Sun, J. Zhou, F. Hao, Q. Zhang, C. Ye, X. Wang, Z. Xu, Q. Wa, F. Liu, X. Meng, J. Wang, P. Lu, Y. Ma, J. Yin, Y. Zhu, S. Chu, B. Huang, L. Gu and Z. Fan, *Angew. Chem., Int. Ed.*, 2024, **63**, e202402841.

212 L. Ouyang, X. He, S. Sun, Y. Luo, D. Zheng, J. Chen, Y. Li, Y. Lin, Q. Liu, A. M. Asiri and X. Sun, *J. Mater. Chem. A*, 2022, **10**, 23494–23498.

213 J. Liang, P. Liu, Q. Li, T. Li, L. Yue, Y. Luo, Q. Liu, N. Li, B. Tang, A. A. Alshehri, I. Shakir, P. O. Agboola, C. Sun and X. Sun, *Angew. Chem., Int. Ed.*, 2022, **61**, e202202087.

214 Q. Liu, L. Xie, J. Liang, Y. Ren, Y. Wang, L. Zhang, L. Yue, T. Li, Y. Luo, N. Li, B. Tang, Y. Liu, S. Gao, A. A. Alshehri, I. Shakir, P. O. Agboola, Q. Kong, Q. Wang, D. Ma and X. Sun, *Small*, 2022, **18**, 2106961.

215 D. Liu, L. Qiao, Y. Chen, P. Zhou, J. Feng, C. C. Leong, K. W. Ng, S. Peng, S. Wang, W. F. Ip and H. Pan, *Appl. Catal., B*, 2023, **324**, 122293.

216 R. Zhang, S. Zhang, Y. Guo, C. Li, J. Liu, Z. Huang, Y. Zhao, Y. Li and C. Zhi, *Energy Environ. Sci.*, 2022, **15**, 3024–3032.

217 N. J. Harmon, C. L. Rooney, Z. Tao, B. Shang, N. Raychaudhuri, C. Choi, H. Li and H. Wang, *ACS Catal.*, 2022, **12**, 9135–9142.

218 D. Dhanabal, S. S. Markandaraj and S. Shanmugam, *ACS Catal.*, 2023, **13**, 9136–9149.

5076 | *Chem. Soc. Rev.*, 2025, **54**, 5021–5080

This journal is © The Royal Society of Chemistry 2025

219 L. Huang, L. Cheng, T. Ma, J.-J. Zhang, H. Wu, J. Su, Y. Song, H. Zhu, Q. Liu, M. Zhu, Z. Zeng, Q. He, M.-K. Tse, D.-T. Yang, B. I. Yakobson, B. Z. Tang, Y. Ren and R. Ye, *Adv. Mater.*, 2023, **35**, 2211856.

220 L. Cheng, T. Ma, B. Zhang, L. Huang, W. Guo, F. Hu, H. Zhu, Z. Wang, T. Zheng, D.-T. Yang, C.-K. Siu, Q. Liu, Y. Ren, C. Xia, B. Z. Tang and R. Ye, *ACS Catal.*, 2022, **12**, 11639–11650.

221 X.-F. Cheng, J.-H. He, H.-Q. Ji, H.-Y. Zhang, Q. Cao, W.-J. Sun, C.-L. Yan and J.-M. Lu, *Adv. Mater.*, 2022, **34**, 2205767.

222 L. Hui, Y. Xue, H. Yu, Y. Liu, Y. Fang, C. Xing, B. Huang and Y. Li, *J. Am. Chem. Soc.*, 2019, **141**, 10677–10683.

223 X. Feng, J. Liu, L. Chen, Y. Kong, Z. Zhang, Z. Zhang, D. Wang, W. Liu, S. Li, L. Tong and J. Zhang, *J. Am. Chem. Soc.*, 2023, **145**, 10259–10267.

224 Y. Wu, J. Lv, F. Xie, R. An, J. Zhang, H. Huang, Z. Shen, L. Jiang, M. Xu, Q. Yao and Y. Cao, *J. Colloid Interface Sci.*, 2024, **656**, 155–167.

225 X. Zheng, Y. Xue, C. Zhang and Y. Li, *CCS Chem.*, 2023, **5**, 1653–1662.

226 B. Chang, L. Li, D. Shi, H. Jiang, Z. Ai, S. Wang, Y. Shao, J. Shen, Y. Wu, Y. Li and X. Hao, *Appl. Catal., B*, 2021, **283**, 119622.

227 W. Lin, H. Chen, G. Lin, S. Yao, Z. Zhang, J. Qi, M. Jing, W. Song, J. Li, X. Liu, J. Fu and S. Dai, *Angew. Chem., Int. Ed.*, 2022, **61**, e202207807.

228 Y. Li, C. Cheng, S. Han, Y. Huang, X. Du, B. Zhang and Y. Yu, *ACS Energy Lett.*, 2022, **7**, 1187–1194.

229 D. Wang, Z.-W. Chen, K. Gu, C. Chen, Y. Liu, X. Wei, C. V. Singh and S. Wang, *J. Am. Chem. Soc.*, 2023, **145**, 6899–6904.

230 J.-Y. Fang, Q.-Z. Zheng, Y.-Y. Lou, K.-M. Zhao, S.-N. Hu, G. Li, O. Akdim, X.-Y. Huang and S.-G. Sun, *Nat. Commun.*, 2022, **13**, 7899.

231 Y. Wang, H. Li, W. Zhou, X. Zhang, B. Zhang and Y. Yu, *Angew. Chem., Int. Ed.*, 2022, **61**, e202202604.

232 T. Hu, M. Wang, C. Guo and C. M. Li, *J. Mater. Chem. A*, 2022, **10**, 8923–8931.

233 J. Cai, J. Huang, A. Cao, Y. Wei, H. Wang, X. Li, Z. Jiang, G. I. N. Waterhouse, S. Lu and S.-Q. Zang, *Appl. Catal., B*, 2023, **328**, 122473.

234 X. Luo, Y. Wu, H. Hu, T. Wei, B. Wu, J. Ding, Q. Liu, J. Luo and X. Liu, *Small*, 2024, **20**, 2403399.

235 G. Zhang, X. Li, K. Chen, Y. Guo, D. Ma and K. Chu, *Angew. Chem., Int. Ed.*, 2023, **62**, e202300054.

236 J. Liang, S. Ma, J. Li, Y. Wang, J. Wu, Q. Zhang, Z. Liu, Z. Yang, K. Qu and W. Cai, *J. Mater. Chem. A*, 2020, **8**, 10426–10432.

237 M. Yu, H. Huang, J. Hu, S. Wang, J. Li and D. Wang, *J. Mater. Chem. A*, 2022, **10**, 23990–23997.

238 G. Lin, Q. Ju, X. Guo, W. Zhao, S. Adimi, J. Ye, Q. Bi, J. Wang, M. Yang and F. Huang, *Adv. Mater.*, 2021, **33**, 2007509.

239 R. Luo, B.-J. Li, Z.-P. Wang, M.-G. Chen, G.-L. Zhuang, Q. Li, J.-P. Tong, W.-T. Wang, Y.-H. Fan and F. Shao, *JACS Au*, 2024, **4**, 3823–3832.

240 Y. Lv, S.-W. Ke, Y. Gu, B. Tian, L. Tang, P. Ran, Y. Zhao, J. Ma, J.-L. Zuo and M. Ding, *Angew. Chem., Int. Ed.*, 2023, **62**, e202305246.

241 J. Ma, Y. Zhang, B. Wang, Z. Jiang, Q. Zhang and S. Zhuo, *ACS Nano*, 2023, **17**, 6687–6697.

242 A. K. K. Padinjareveetil, J. V. Perales-Rondon, D. Zaoralová, M. Otyepka, O. Alduhaish and M. Pumera, *ACS Appl. Mater. Interfaces*, 2023, **15**, 47294–47306.

243 J. V. Perales-Rondon, D. Rojas, W. Gao and M. Pumera, *ACS Sustainable Chem. Eng.*, 2023, **11**, 6923–6931.

244 W. Gao, J. V. Perales-Rondon, J. Michalička and M. Pumera, *Appl. Catal., B*, 2023, **330**, 122632.

245 W. Gao, J. Michalička and M. Pumera, *J. Mater. Chem. A*, 2024, **12**, 32458–32470.

246 Z. Huang, M. Rafiq, A. R. Woldu, Q.-X. Tong, D. Astruc and L. Hu, *Coord. Chem. Rev.*, 2023, **478**, 214981.

247 C. Tang and S.-Z. Qiao, *Chem. Soc. Rev.*, 2019, **48**, 3166–3180.

248 F. F. Tao, L. Nguyen and S. Zhang, *Metal nanoparticles for catalysis: advances and applications*, The Royal Society of Chemistry, 2014.

249 B. H. Ko, B. Hasa, H. Shin, Y. Zhao and F. Jiao, *J. Am. Chem. Soc.*, 2022, **144**, 1258–1266.

250 J. Long, S. Chen, Y. Zhang, C. Guo, X. Fu, D. Deng and J. Xiao, *Angew. Chem., Int. Ed.*, 2020, **59**, 9711–9718.

251 J. Lim, C.-Y. Liu, J. Park, Y.-H. Liu, T. P. Senftle, S. W. Lee and M. C. Hatzell, *ACS Catal.*, 2021, **11**, 7568–7577.

252 T. Hu, C. Wang, M. Wang, C. M. Li and C. Guo, *ACS Catal.*, 2021, **11**, 14417–14427.

253 J. Wang, Y. Wang, C. Cai, Y. Liu, D. Wu, M. Wang, M. Li, X. Wei, M. Shao and M. Gu, *Nano Lett.*, 2023, **23**, 1897–1903.

254 W. Peng, M. Luo, X. Xu, K. Jiang, M. Peng, D. Chen, T.-S. Chan and Y. Tan, *Adv. Energy Mater.*, 2020, **10**, 2001364.

255 Y. Xu, K. Ren, T. Ren, M. Wang, Z. Wang, X. Li, L. Wang and H. Wang, *Appl. Catal., B*, 2022, **306**, 121094.

256 Y. Han, X. Zhang, W. Cai, H. Zhao, Y. Zhang, Y. Sun, Z. Hu, S. Li, J. Lai and L. Wang, *J. Colloid Interface Sci.*, 2021, **600**, 620–628.

257 L. Lv, Y. Shen, J. Liu, X. Meng, X. Gao, M. Zhou, Y. Zhang, D. Gong, Y. Zheng and Z. Zhou, *J. Phys. Chem. Lett.*, 2021, **12**, 11143–11150.

258 G. A. Cerrón-Calle, A. S. Fajardo, C. M. Sánchez-Sánchez and S. Garcia-Segura, *Appl. Catal., B*, 2022, **302**, 120844.

259 N. Zhou, Z. Wang, N. Zhang, D. Bao, H. Zhong and X. Zhang, *ACS Catal.*, 2023, **13**, 7529–7537.

260 M. Yang, T. Wei, J. He, Q. Liu, L. Feng, H. Li, J. Luo and X. Liu, *Nano Res.*, 2024, **17**, 1209–1216.

261 X. Qu, L. Shen, Y. Mao, J. Lin, Y. Li, G. Li, Y. Zhang, Y. Jiang and S. Sun, *ACS Appl. Mater. Interfaces*, 2019, **11**, 31869–31877.

262 Z.-Y. Wu, M. Karamad, X. Yong, Q. Huang, D. A. Cullen, P. Zhu, C. Xia, Q. Xiao, M. Shakouri, F.-Y. Chen, J. Y. T. Kim, Y. Xia, K. Heck, Y. Hu, M. S. Wong, Q. Li, I. Gates, S. Siahrostami and H. Wang, *Nat. Commun.*, 2021, **12**, 2870.

This journal is © The Royal Society of Chemistry 2025

Chem. Soc. Rev., 2025, **54**, 5021–5080 | **5077**

263 W.-D. Zhang, H. Dong, L. Zhou, H. Xu, H.-R. Wang, X. Yan, Y. Jiang, J. Zhang and Z.-G. Gu, *Appl. Catal., B*, 2022, **317**, 121750.

264 J. Yang, H. Qi, A. Li, X. Liu, X. Yang, S. Zhang, Q. Zhao, Q. Jiang, Y. Su, L. Zhang, J.-F. Li, Z.-Q. Tian, W. Liu, A. Wang and T. Zhang, *J. Am. Chem. Soc.*, 2022, **144**, 12062–12071.

265 J. Cheng, W. Sun, G. Dai, X. Yang, R. Xia, Y. Xu, X. Yang and W. Tu, *Fuel*, 2023, **332**, 126106.

266 T. Xiang, Y. Liang, Y. Zeng, J. Deng, J. Yuan, W. Xiong, B. Song, C. Zhou and Y. Yang, *Small*, 2023, **19**, 2303732.

267 P. Guo, D. Luan, H. Li, L. Li, S. Yang and J. Xiao, *J. Am. Chem. Soc.*, 2024, **146**, 13974–13982.

268 J. Deng, Y. Su, D. Liu, P. Yang, B. Liu and C. Liu, *Chem. Rev.*, 2019, **119**, 9221–9259.

269 S. Garcia-Segura, M. Lanzarini-Lopes, K. Hristovski and P. Westerhoff, *Appl. Catal., B*, 2018, **236**, 546–568.

270 H. Jiang, G.-F. Chen, O. Savateev, J. Xue, L.-X. Ding, Z. Liang, M. Antonietti and H. Wang, *Angew. Chem., Int. Ed.*, 2023, **62**, e202218717.

271 F. Gou, H. Wang, M. Fu, Y. Jiang, W. Shen, R. He and M. Li, *Appl. Surf. Sci.*, 2023, **612**, 155872.

272 Q. He, S. Qiao, Y. Zhou, R. Vajtai, D. Li, P. M. Ajayan, L. Ci and L. Song, *Adv. Funct. Mater.*, 2022, **32**, 2106684.

273 J. O. Olowoyo and R. J. Kriek, *Small*, 2022, **18**, 2203125.

274 Z. Deng, C. Ma, Z. Li, Y. Luo, L. Zhang, S. Sun, Q. Liu, J. Du, Q. Lu, B. Zheng and X. Sun, *ACS Appl. Mater. Interfaces*, 2022, **14**, 46595–46602.

275 J. Yuan, H. Yin, X. Jin, D. Zhao, Y. Liu, A. Du, X. Liu and A. P. O'Mullane, *Appl. Catal., B*, 2023, **325**, 122353.

276 A. Ambrosi, C. K. Chua, N. M. Latiff, A. H. Loo, C. H. A. Wong, A. Y. S. Eng, A. Bonanni and M. Pumera, *Chem. Soc. Rev.*, 2016, **45**, 2458–2493.

277 C. Huang, Y. Li, N. Wang, Y. Xue, Z. Zuo, H. Liu and Y. Li, *Chem. Rev.*, 2018, **118**, 7744–7803.

278 H. Yu, Y. Xue, L. Hui, C. Zhang, Y. Fang, Y. Liu, X. Chen, D. Zhang, B. Huang and Y. Li, *Natl. Sci. Rev.*, 2021, **8**, nwaa213.

279 H. Zou, W. Rong, S. Wei, Y. Ji and L. Duan, *Proc. Natl. Acad. Sci. U. S. A.*, 2020, **117**, 29462–29468.

280 X. Yu, P. Han, Z. Wei, L. Huang, Z. Gu, S. Peng, J. Ma and G. Zheng, *Joule*, 2018, **2**, 1610–1622.

281 S. Wang, C. Song, Y. Cai, Y. Li, P. Jiang, H. Li, B. Yu and T. Ma, *Adv. Energy Mater.*, 2023, **13**, 2301136.

282 L. Verger, V. Natu, M. Carey and M. W. Barsoum, *Trends Chem.*, 2019, **1**, 656–669.

283 Y. Li, J. Ma, T. D. Waite, M. R. Hoffmann and Z. Wang, *Environ. Sci. Technol.*, 2021, **55**, 10695–10703.

284 Y. Xiao and C. Shen, *Small*, 2021, **17**, 2100776.

285 L. Zhang, J. Liang, Y. Wang, T. Mou, Y. Lin, L. Yue, T. Li, Q. Liu, Y. Luo, N. Li, B. Tang, Y. Liu, S. Gao, A. A. Alshehri, X. Guo, D. M. Ma and X. Sun, *Angew. Chem., Int. Ed.*, 2021, **60**, 25263–25268.

286 S. Zhang, M. Li, J. Li, Q. Song and X. Liu, *Proc. Natl. Acad. Sci. U. S. A.*, 2022, **119**, e2115504119.

287 D. Pan, M. Austeria P, S. Lee, H.-S. Bae, F. He, G. H. Gu and W. Choi, *Nat. Commun.*, 2024, **15**, 7243.

288 Y. Ying, M. P. Browne and M. Pumera, *Sustainable Energy Fuels*, 2020, **4**, 3732–3738.

289 K. P. A. Kumar, K. Ghosh, O. Alduhaish and M. Pumera, *Electrochem. Commun.*, 2021, **122**, 106890.

290 E. Redondo and M. Pumera, *Appl. Mater. Today*, 2021, **25**, 101253.

291 C. Didier, A. Kundu and S. Rajaraman, *Microsyst. Nanoeng.*, 2020, **6**, 15.

292 C. Iffelsberger, S. Ng and M. Pumera, *Appl. Mater. Today*, 2020, **20**, 100654.

293 V. Urbanová, J. Plutnar and M. Pumera, *Appl. Mater. Today*, 2021, **24**, 101131.

294 G. Bharath, C. Liu, F. Banat, A. Kumar, A. Hai, A. K. Nadda, V. K. Gupta, M. A. Haija and J. Balamurugan, *Chem. Eng. J.*, 2023, **465**, 143040.

295 V. R. Silveira, R. Bericat-Vadell and J. Sá, *J. Phys. Chem. C*, 2023, **127**, 5425–5431.

296 N. Gao, H. Yang, D. Dong, D. Dou, Y. Liu, W. Zhou, F. Gao, C. Nan, Z. Liang and D. Yang, *J. Colloid Interface Sci.*, 2022, **611**, 294–305.

297 C. H. Kim, J. Kim, F. Hollmann and C. B. Park, *Appl. Catal., B*, 2023, **336**, 122925.

298 F. Xu, F. Wu, K. Zhu, Z. Fang, D. Jia, Y. Wang, G. Jia, J. Low, W. Ye, Z. Sun, P. Gao and Y. Xiong, *Appl. Catal., B*, 2021, **284**, 119689.

299 S. Zhou, K. Sun, C. Y. Toe, J. Yin, J. Huang, Y. Zeng, D. Zhang, W. Chen, O. F. Mohammed, X. Hao and R. Amal, *Adv. Mater.*, 2022, **34**, 2201670.

300 L. Paramanik, S. Sultana and K. M. Parida, *J. Colloid Interface Sci.*, 2022, **625**, 83–99.

301 X. Li, W. Fan, Y. Bai, Y. Liu, F. Wang, H. Bai and W. Shi, *Chem. Eng. J.*, 2022, **433**, 133225.

302 D. Liu, J. Wang, S. Bian, Q. Liu, Y. Gao, X. Wang, P. K. Chu and X.-F. Yu, *Adv. Funct. Mater.*, 2020, **30**, 2002731.

303 Y. Bai, S. Gao, W. Xie, Z. Fang, H. Bai and W. Fan, *Int. J. Hydrogen Energy*, 2023, **48**, 10882–10890.

304 P. Li, Y. Liu, M. A. Mushtaq and D. Yan, *Inorg. Chem. Front.*, 2023, **10**, 4650–4667.

305 P. H. van Langevelde, I. Katsounaros and M. T. M. Koper, *Joule*, 2021, **5**, 290–294.

306 U. S. Environmental Protection Agency, Drinking Water Standards and Health Advisories, EPA 822-F-18-001, 2018, **https://www.epa.gov/system/files/documents/2022-2001/dwtable2018.pdf**.

307 L. Su, D. Han, G. Zhu, H. Xu, W. Luo, L. Wang, W. Jiang, A. Dong and J. Yang, *Nano Lett.*, 2019, **19**, 5423–5430.

308 M. Duca and M. T. M. Koper, *Energy Environ. Sci.*, 2012, **5**, 9726–9742.

309 S. Lee, S. Kim, C. Park, W. Kim, S. Ryu and W. Choi, *Energy Environ. Sci.*, 2021, **14**, 4437–4450.

310 C. Park, H. Kwak, G.-H. Moon and W. Kim, *J. Mater. Chem. A*, 2021, **9**, 19179–19205.

311 J. M. McEnaney, S. J. Blair, A. C. Nielander, J. A. Schwalbe, D. M. Koshy, M. Cargnello and T. F. Jaramillo, *ACS Sustainable Chem. Eng.*, 2020, **8**, 2672–2681.

5078 | *Chem. Soc. Rev.*, 2025, **54**, 5021–5080

This journal is © The Royal Society of Chemistry 2025

312 W. Zheng, L. Zhu, Z. Yan, Z. Lin, Z. Lei, Y. Zhang, H. Xu, Z. Dang, C. Wei and C. Feng, *Environ. Sci. Technol.*, 2021, **55**, 13231–13243.

313 N. C. Kani, J. A. Gauthier, A. Prajapati, J. Edgington, I. Bordawekar, W. Shields, M. Shields, L. C. Seitz, A. R. Singh and M. R. Singh, *Energy Environ. Sci.*, 2021, **14**, 6349–6359.

314 X. Wu, Z. Song, Z. Liu, X. Tang, F. Yao, F. Zhao, X. Min and C.-J. Tang, *Appl. Catal., B*, 2024, **359**, 124467.

315 F.-Y. Chen, A. Elgazzar, S. Pecaut, C. Qiu, Y. Feng, S. Ashokkumar, Z. Yu, C. Sellers, S. Hao, P. Zhu and H. Wang, *Nat. Catal.*, 2024, **7**, 1032–1043.

316 Q. Zhang, Y. Li, M. Geng, J. Zhu, H. Sun and B. Jiang, *Appl. Catal., B*, 2023, **330**, 122658.

317 G. Zhang, B. Li, Y. Shi, Q. Zhou, W.-J. Fu, G. Zhou, J. Ma, S. Yin, W. Yuan, S. Miao, Q. Ji, J. Qu and H. Liu, *Nat. Sustainable*, 2024, **7**, 1251–1263.

318 M. Jiang, M. Zhu, M. Wang, Y. He, X. Luo, C. Wu, L. Zhang and Z. Jin, *ACS Nano*, 2023, **17**, 3209–3224.

319 A. Khan, A. Abbas and R. Dickson, *Green Chem.*, 2024, **26**, 1551–1565.

320 Y. Wan, M. Zheng, W. Yan, J. Zhang and R. Lv, *Adv. Energy Mater.*, 2024, **14**, 2303588.

321 J. Leverett, T. Tran-Phu, J. A. Yuwono, P. Kumar, C. Kim, Q. Zhai, C. Han, J. Qu, J. Cairney, A. N. Simonov, R. K. Hocking, L. Dai, R. Daiyan and R. Amal, *Adv. Energy Mater.*, 2022, **12**, 2201500.

322 J. Zheng, S. Xu, J. Sun, J. Zhang, L. Sun, X. Pan, L. Li and G. Zhao, *Appl. Catal., B*, 2023, **338**, 123056.

323 Y. Luo, K. Xie, P. Ou, C. Lavallais, T. Peng, Z. Chen, Z. Zhang, N. Wang, X.-Y. Li, I. Grigioni, B. Liu, D. Sinton, J. B. Dunn and E. H. Sargent, *Nat. Catal.*, 2023, **6**, 939–948.

324 D.-S. Huang, X.-F. Qiu, J.-R. Huang, M. Mao, L. Liu, Y. Han, Z.-H. Zhao, P.-Q. Liao and X.-M. Chen, *Nat. Synth.*, 2024, **3**, 1404–1413.

325 H. Xiong, P. Yu, K. Chen, S. Lu, Q. Hu, T. Cheng, B. Xu and Q. Lu, *Nat. Catal.*, 2024, **7**, 785–795.

326 N. Meng, X. Ma, C. Wang, Y. Wang, R. Yang, J. Shao, Y. Huang, Y. Xu, B. Zhang and Y. Yu, *ACS Nano*, 2022, **16**, 9095–9104.

327 X. Liu, P. V. Kumar, Q. Chen, L. Zhao, F. Ye, X. Ma, D. Liu, X. Chen, L. Dai and C. Hu, *Appl. Catal., B*, 2022, **316**, 121618.

328 J. Mukherjee, S. Paul, A. Adalder, S. Kapse, R. Thapa, S. Mandal, B. Ghorai, S. Sarkar and U. K. Ghorai, *Adv. Funct. Mater.*, 2022, **32**, 2200882.

329 C. Lv, L. Zhong, H. Liu, Z. Fang, C. Yan, M. Chen, Y. Kong, C. Lee, D. Liu, S. Li, J. Liu, L. Song, G. Chen, Q. Yan and G. Yu, *Nat. Sustainable*, 2021, **4**, 868–876.

330 X. Wei, X. Wen, Y. Liu, C. Chen, C. Xie, D. Wang, M. Qiu, N. He, P. Zhou, W. Chen, J. Cheng, H. Lin, J. Jia, X.-Z. Fu and S. Wang, *J. Am. Chem. Soc.*, 2022, **144**, 11530–11535.

331 M. Yuan, J. Chen, Y. Bai, Z. Liu, J. Zhang, T. Zhao, Q. Wang, S. Li, H. He and G. Zhang, *Angew. Chem., Int. Ed.*, 2021, **60**, 10910–10918.

332 Y. Wang, S. Xia, R. Cai, J. Zhang, C. Yu, J. Cui, Y. Zhang, J. Wu and Y. Wu, *Angew. Chem., Int. Ed.*, 2024, **63**, e202318589.

333 Y. Yang, J. Peng, Z. Shi, P. Zhang, A. Arramel and N. Li, *J. Mater. Chem. A*, 2023, **11**, 6428–6439.

334 Y. Zhang, L. Lu, T. Zhao, J. Zhao, Q. Cai and Z. Chen, *J. Mater. Chem. A*, 2024, **12**, 16704–16715.

335 B. Govindan, K. Annamalai, A. Kumar, S. Palanisamy, M. Abu Haija and F. Banat, *ACS Sustainable Chem. Eng.*, 2024, **12**, 8174–8187.

336 X. Zhu, X. Zhou, Y. Jing and Y. Li, *Nat. Commun.*, 2021, **12**, 4080.

337 X. Cao, D. Zhang, Y. Gao, O. V. Prezhdo and L. Xu, *J. Am. Chem. Soc.*, 2024, **146**, 1042–1052.

338 H. Cai, Z. Wang, G. Meng, T. Wei, Y. Liu, J. Luo, Q. Liu, G. Hu and X. Liu, *Inorg. Chem.*, 2024, **63**, 20935–20939.

339 P. Li, Z. Jin, Z. Fang and G. Yu, *Energy Environ. Sci.*, 2021, **14**, 3522–3531.

340 Z. Fang, Z. Jin, S. Tang, P. Li, P. Wu and G. Yu, *ACS Nano*, 2022, **16**, 1072–1081.

341 J.-Y. Zhu, Q. Xue, Y.-Y. Xue, Y. Ding, F.-M. Li, P. Jin, P. Chen and Y. Chen, *ACS Appl. Mater. Interfaces*, 2020, **12**, 14064–14070.

342 X. Deng, Y. Yang, L. Wang, X.-Z. Fu and J.-L. Luo, *Adv. Sci.*, 2021, **8**, 2004523.

343 K. Fan, W. Xie, J. Li, Y. Sun, P. Xu, Y. Tang, Z. Li and M. Shao, *Nat. Commun.*, 2022, **13**, 7958.

344 X.-B. Li, C.-H. Tung and L.-Z. Wu, *Angew. Chem., Int. Ed.*, 2019, **58**, 10804–10811.

345 E. A. Weiss, *ACS Energy Lett.*, 2017, **2**, 1005–1013.

346 S.-L. Meng, J.-H. Li, C. Ye, Y.-L. Yin, X.-L. Zhang, C. Zhang, X.-B. Li, C.-H. Tung and L.-Z. Wu, *Adv. Mater.*, 2024, **36**, 2311982.

347 Z. Niu, S. Fan, X. Li, P. Wang, Z. Liu, J. Wang, C. Bai and D. Zhang, *Chem. Eng. J.*, 2022, **450**, 138343.

348 S. Verma, S. Lu and P. J. A. Kenis, *Nat. Energy*, 2019, **4**, 466–474.

349 Á. Balog, E. Kecsenovity, G. F. Samu, J. He, D. Fekete and C. Janáky, *Nat. Catal.*, 2024, **7**, 522–535.

350 J. Kim, J.-A. Lin, J. Kim, I. Roh, S. Lee and P. Yang, *Nat. Catal.*, 2024, **7**, 977–986.

351 W. Zhu, X. Zhang, F. Yao, R. Huang, Y. Chen, C. Chen, J. Fei, Y. Chen, Z. Wang and H. Liang, *Angew. Chem., Int. Ed.*, 2023, **62**, e202300390.

352 S. Li, P. Ma, C. Gao, L. Liu, X. Wang, M. Shakouri, R. Chernikov, K. Wang, D. Liu, R. Ma and J. Wang, *Energy Environ. Sci.*, 2022, **15**, 3004–3014.

353 S. Ye, Z. Chen, G. Zhang, W. Chen, C. Peng, X. Yang, L. Zheng, Y. Li, X. Ren, H. Cao, D. Xue, J. Qiu, Q. Zhang and J. Liu, *Energy Environ. Sci.*, 2022, **15**, 760–770.

354 M. Yang, T. Wei, C. Zeng, J. Zhang, Y. Liu, J. Luo, G. Hu and X. Liu, *Chem. Eng. J.*, 2024, **498**, 155799.

355 R. Zaffaroni, D. Ripepi, J. Middelkoop and F. M. Mulder, *ACS Energy Lett.*, 2020, **5**, 3773–3777.

356 C. Zhang, J. Li, R. Chen, S. Shen, J. Wang, Y. Sun and F. Dong, *ACS Catal.*, 2024, **14**, 15721–15742.

This journal is © The Royal Society of Chemistry 2025

Chem. Soc. Rev., 2025, **54**, 5021–5080 | **5079**

357 Y. Zhao, R. Shi, X. Bian, C. Zhou, Y. Zhao, S. Zhang, F. Wu, G. I. N. Waterhouse, L.-Z. Wu, C.-H. Tung and T. Zhang, *Adv. Sci.*, 2019, **6**, 1802109.

358 N. Amornthammarong, J.-Z. Zhang and P. B. Ortner, *Anal. Methods*, 2011, **3**, 1501–1506.

359 S. Z. Andersen, V. Čolić, S. Yang, J. A. Schwalbe, A. C. Nielander, J. M. McEnaney, K. Enemark-Rasmussen, J. G. Baker, A. R. Singh, B. A. Rohr, M. J. Statt, S. J. Blair, S. Mezzavilla, J. Kibsgaard, P. C. K. Vesborg, M. Cargnello, S. F. Bent, T. F. Jaramillo, I. E. L. Stephens, J. K. Nørskov and I. Chorkendorff, *Nature*, 2019, **570**, 504–508.

360 J. B. Hansen and P. Han, *Green Ammonia by Haldor Topsoe*, Department of Energy, 2021, **https://www.energy.gov/sites/default/files/2021-2008/2024-green-ammonia-haldor-topsoe.pdf**.

361 *Small-Scale Green Ammonia Plants Open up New Storage Possibilities for Wind and Solar Power*, ThyssenKrupp Industrial Solutions, 2022, **https://insights.thyssenkrupp-industrial-solutions.com/story/small-scale-green-ammonia-plants-open-up-new-storage-possibilities-for-wind-and-solar-power/**.

362 *Yara Selects Linde Engineering to Build Electrolysis Plant at Porsgrunn*, Ammonia Energy Association, 2022, **https://www.ammoniaenergy.org/articles/yara-selects-linde-engineering-to-build-electrolysis-plant-at-porsgrunn/**.

363 S. Wu, N. Salmon, M. M.-J. Li, R. Bañares-Alcántara and S. C. E. Tsang, *ACS Energy Lett.*, 2022, **7**, 1021–1033.

364 B. Bonnet-Cantalloube, M. Espitalier-Noël, P. F. de Carvalho, J. Fonseca and G. Pawelec, *Clean ammonia in the future energy system, Hydrogen Europe*, 2023, **https://hydrogeneurope.eu/wp-content/uploads/2023/2003/2023.2003_H2022Europe_Clean_Ammonia_Report_DIGITAL_FINAL.pdf**.

365 ENGIE-YARA, Renewable Hydrogen and Ammonia Deployment in Pilbara, YURI Phase 0: Feasibility study public report, 2020, **https://arena.gov.au/assets/2020/2011/engie-yara-renewable-hydrogen-and-ammonia-deployment-in-pilbara.pdf**.

366 Kapsom, *The World's First Green Ammonia Plant Was Made By Kapsom, Green ammonia produced from renewable,to a renewable energy drive*, 2022, **https://www.kapsom.com/the-worlds-first-green-ammonia-plant-was-made-by-kapsom/**.

367 W. Bi, E. Gyenge and D. P. Wilkinson, *Chem. Eng. J.*, 2023, **478**, 147359.

368 *H2F project, Green hydrogen, green ammonia and green fertiliser plant*, **https://www.fertiberia.com/en/greenammonia/h2f-project/**.

369 P. Mayer, A. Ramirez, G. Pezzella, B. Winter, S. M. Sarathy, J. Gascon and A. Bardow, *iScience*, 2023, **26**, 107389.

370 M.-H. Yuan, Y.-H. Chen, J.-Y. Tsai and C.-Y. Chang, *Process Saf. Environ. Prot.*, 2016, **102**, 777–785.

371 L. Zeng, C. Mangan and X. Li, *Water Sci. Technol.*, 2006, **54**, 137–145.

372 J. Gao, Q. Ma, Z. Wang, B. E. Rittmann and W. Zhang, *Nat. Commun.*, 2024, **15**, 8455.

373 L. M. Wilder, K. Wyatt, C. A. Skangos, W. E. Klein, M. R. Parimuha, J. L. Katsirubas, J. L. Young and E. M. Miller, *ACS Appl. Energy Mater.*, 2024, **7**, 536–545.

374 K. Kim, C.-Y. Yoo, J.-N. Kim, H. C. Yoon and J.-I. Han, *J. Electrochem. Soc.*, 2016, **163**, F1523.

375 S. Li, D. Han, G. Jiang, Z. Han, H. Lu, J. Gao, X. Wang, Y. Wang, C. Geng, Z. Weng and Q.-H. Yang, *ACS Appl. Energy Mater.*, 2023, **6**, 5067–5073.

376 W. Liao, J. Wang, G. Ni, K. Liu, C. Liu, S. Chen, Q. Wang, Y. Chen, T. Luo, X. Wang, Y. Wang, W. Li, T.-S. Chan, C. Ma, H. Li, Y. Liang, W. Liu, J. Fu, B. Xi and M. Liu, *Nat. Commun.*, 2024, **15**, 1264.

377 S.-N. Zhang, P. Gao, Q.-Y. Liu, Z. Zhang, B.-L. Leng, J.-S. Chen and X.-H. Li, *Nat. Commun.*, 2024, **15**, 10877.

378 Z. Xu, L. Wan, Y. Liao, M. Pang, Q. Xu, P. Wang and B. Wang, *Nat. Commun.*, 2023, **14**, 1619.

379 J. Lan, Z. Wang, C.-W. Kao, Y.-R. Lu, F. Xie and Y. Tan, *Nat. Commun.*, 2024, **15**, 10173.

380 L. Mi, Q. Huo, J. Cao, X. Chen, H. Yang, Q. Hu and C. He, *Adv. Energy Mater.*, 2022, **12**, 2202247.